isvr Institute of Sound and Vibration Research

# Theoretical Study of a Velometer Sensor Piezoelectric Patch Actuator pair for Direct Velocity Feedback Control Systems

**M. Gavagni, P. Garadonio and S.J. Elliott**

ISVR Technical Report No 303

July 2004

University of Southampton

# SCIENTIFIC PUBLICATIONS BY THE ISVR

***Technical Reports*** are published to promote timely dissemination of research results by ISVR personnel. This medium permits more detailed presentation than is usually acceptable for scientific journals. Responsibility for both the content and any opinions expressed rests entirely with the author(s).

***Technical Memoranda*** are produced to enable the early or preliminary release of information by ISVR personnel where such release is deemed to the appropriate. Information contained in these memoranda may be incomplete, or form part of a continuing programme; this should be borne in mind when using or quoting from these documents.

***Contract Reports*** are produced to record the results of scientific work carried out for sponsors, under contract. The ISVR treats these reports as confidential to sponsors and does not make them available for general circulation. Individual sponsors may, however, authorize subsequent release of the material.

# Theoretical study of a velometer sensor – piezoelectric patch actuator pair for direct velocity feedback control systems

**by M. Gavagni, P. Gardonio and S.J. Elliott**

ISVR Technical Report N° 303

July 2004

UNIVERSITY OF SOUTHAMPTON

INSTITUTE OF SOUND AND VIBRATION RESEARCH

SIGNAL PROCESSING AND CONTROL GROUP

# Theoretical study of a velometer sensor – piezoelectric patch actuator pair for direct velocity feedback control systems

by

**M. Gavagni, P. Gardonio and S.J. Elliott**

ISVR Technical Report N° 303

July 2004

Authorized for issue by
Professor S.J. Elliott
Group Chairman

## ABSTRACT

*This report discusses the design of a new velocity sensor to be used in combination with a piezoelectric patch actuator to form a closely located sensor–actuator pair for the implementation of direct velocity feedback control loops. The velocity sensor consists of a principal spring–mass seismic sensor with embedded a direct velocity feedback control loop acting on the lumped mass itself. This simple control system could be bonded onto a panel in order to generate active damping, which would reduce the vibration of the panel dominated by well separated low frequency resonances. In particular, arrays of these control units could be scattered over the surface of a panel in order to control its vibrations over a wide frequency band. When direct velocity feedback is implemented, then stability is guaranteed if the sensor and actuator are collocated and dual. Although a piezoelectric patch does not generate a force, the velocity sensor considered in this report has been designed to directly provide a signal proportional to the velocity at the centre of the piezoelectric patch actuator. Also, its response has been arranged in such a way as to provide a low pass filtering effect, so that the unwanted higher frequencies excitation effects produced by the piezoelectric patch actuator are attenuated. In this way, provided the size and material of the piezoelectric patch are properly chosen, the velocity sensor and piezoelectric patch actuator frequency response function results to be close to that of a collocated pair so that relatively high control gains could be implemented. The response of the velocity sensor with the internal feedback control loop has been studied theoretically with a lumped parameter model which takes into account both the dynamics effect of spring–mass sensor as well as the dynamics effects of the accelerometer sensor used for the internal feedback control loop. Also, the stability of the velocity sensor and piezoelectric patch actuator control system when mounted on a plate has been studied using a mobility model. In particular, a parametric study has also been included in the report in order to assess the stability of the velocity sensor and piezoelectric patch actuator as the size and mass of the piezoelectric patch actuator are varied.*

## TABLE OF CONTENTS

# 1. INTRODUCTION

This report is concerned with the design and development of a micro-worked velocity sensor or MEMS (Micro Electro Mechanical System) "velometer". Such a sensor is planned to be used in a grid of decentralised feedback control systems which are embedded in smart panels for the implementation of active structural acoustic control (ASAC) [1,2]. Each feedback control system is made of a closely located piezoelectric patch actuator and micro--worked velocity sensor. The aim is to obtain a grid of control units that produce active damping so that the response of the panel at low frequency resonances is attenuated. There are many ways for implementing active damping control [3]: for example using direct velocity feedback (DVFB). This approach is perhaps the simplest and, in some cases, the most effective one. For DVFB, the structure-borne or the air-borne disturbances on a structure (in this study a rectangular plate) are detected by a velocity sensor, then electronically multiplied by a fixed negative gain and finally feed feedback to an actuator (in this study a piezoelectric patch bonded on the panel). If the sensor and the actuator are collocated and dual [3,4], then the sensor-actuator response function is real and positive so that the feedback control loop is unconditionally stable [3-5] and thus large control gains could be implemented which produce high levels of damping that reduces the response of the structure at low frequency resonances [1,2]. In contrast, if the sensor and the actuator are not collocated and dual then the sensor-actuator response function can have real part negative in which case a velocity feedback loop is only conditionally stable and so a limited range of control gains could be implemented which produces relatively small damping effects [3,4]. Unconditional and conditional stability depends on the reciprocal collocation and duality of the sensor and actuator pair [4]. For example, a linear velocity sensor and an equally oriented ideal skyhook force actuator positioned at the same point of a structure are collocated and dual and thus could be used to implement an unconditionally stable direct velocity feedback control loop. Alternatively, an accelerometer sensor placed at the centre of a piezoelectric patch strain actuator provides a conditionally stable velocity feedback control system since the sensing and the actuation are neither collocated (different positions for actuation and detection which occurs respectively along the borders of the actuator patch and at the centre of the patch) nor dual (moment excitation versus linear detection of the sensor).

The aim of this study is to design a velocity sensor that gives a better collocation effect than the ordinary accelerometers sensors when used in a velocity feedback control unit with a piezoelectric patch actuator. Also the sensor is intended to produce a signal output, in the controlled frequency band, directly proportional to velocity so that there is no need to have an integrator circuit. Finally, the velocity sensor is designed in such a way as its response gradually rolls off beyond the frequency range of control so that higher frequencies sensor–actuator dynamics effects, that could destabilize the system, are not amplified by the feedback loop [3]. This is an important issue which is closely linked to the actuation mechanisms of the piezoelectric patch. Therefore a parametric study is also presented in order to assess the size and mass effects of a piezoelectric patch actuator and to analyse the intrinsic characteristics of the vibration sensor (natural frequency and damping effects).

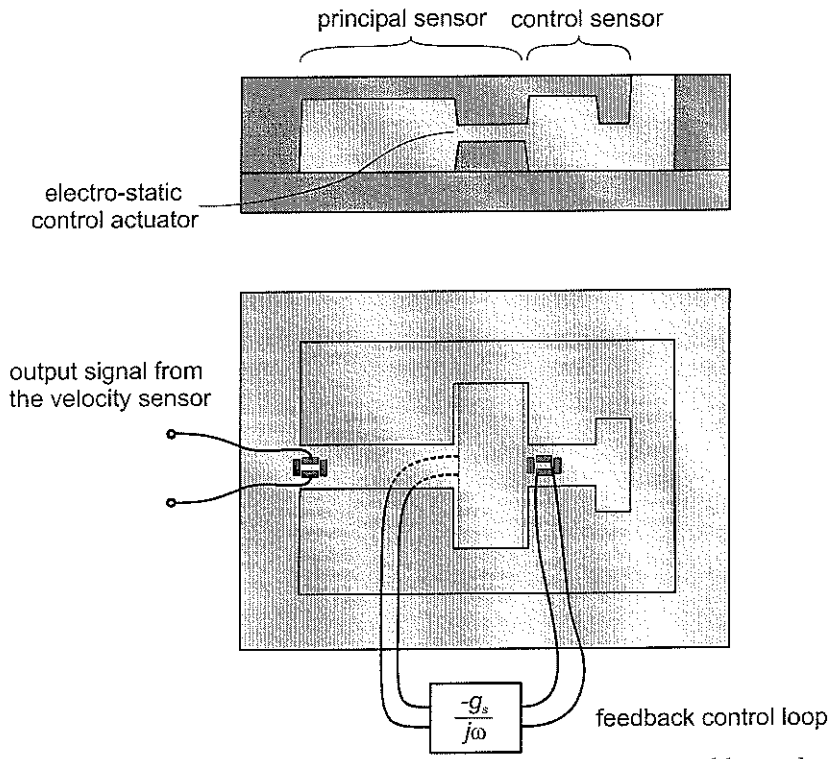


**Figure 1:** *velometer sensor made by a principal cantilever beam spring and lumped mass seismic sensor with an a fixed gain velocity feedback control loop acting on the lumped mass which is made with a control cantilever beam spring and lumped mass seismic sensor and electrostatic control actuator.*

As shown in Figure 1 above, the velocity sensor developed in this study consists a principal cantilever-beam spring and lumped mass seismic sensor with a direct velocity feedback control loop acting on the lumped mass which is made by a control cantilever-beam spring and lumped mass seismic sensor and an electrostatic control actuator. In the remaining part

of the report the whole system will be referred as the "velocity sensor" while the two internal seismic sensors will be referred as the "principal sensor" and the "control sensor" respectively. The micro fabricated device is made of a small quadrilateral frame (size about 5000×5000 μm) with, at the interior, a small cantilever beam (size about 250×20×1000 μm) having a lumped mass at the tip (size about 340×20×100 μm). A set of four equal piezoresistors sensitive to strain are bonded near the clamped side of the small cantilever beam: two of them are aligned with the axis of the beam while the other two are orthogonal to the axis of the beam. The four piezoresistors are electrically connected to form a Wheatstone bridge in such a way as to provide a signal output directly proportional to the variation of resistance of the two axially aligned piezoresistors. In this way the output signal is directly proportional to the deflection of the cantilever beam, i.e. the relative displacement between the seismic mass and the base frame. If the fundamental resonance frequency of this cantilever-beam spring and lumped mass system is well above the frequency range of interest for the measurement, then the detected output signal is directly proportional to the acceleration of the base frame [6]. At frequencies above the fundamental resonance frequency, the sensor output gradually rolls off so that the extra phase shift introduced by the resonance of the cantilever-beam spring and lumped mass system would produce relatively small effects in a direct velocity feedback control system. Also, any other higher frequencies dynamics effects of the sensor–actuator pair that could generate instabilities in a direct velocity feedback loop are reduced. However in the vicinity of the fundamental resonance frequency, both the above mentioned phase shift and the dynamics effects of the sensor–actuator pair are amplified. This problem could be attenuated by introducing additional damping effects in the micro fabricated cantilever-beam spring and lumped mass system. However, increasing the passive damping on the suspended mass does not solely reduce the amplitude of the resonance but also diminishes the constant roll off effect beyond the resonance frequency and stretches the $180^{\circ}$ phase shift over a wide frequency band around the resonance frequency [6]. This is due to the fact that passive damping is generated by the relative velocity of the seismic-mass and base so that for large damping coefficients the seismic mass is constrained to move together with the base. This problem could be avoided by embedding on the cantilever-beam spring and lumped-mass system a local direct velocity feedback loop which generates a control force on the seismic-mass directly proportional to its velocity so that absolute damping rather than relative damping is

generated [7]. In this case it is possible to reduce the amplitude of the output signal at the fundamental resonance frequency of the principal sensor without degrading the output signal higher frequencies roll off. Therefore, as shown in Figure 1, a second cantilever-beam spring (size about 250×20×750 μm), with the four piezoresistor transducers at the base, and lumped mass (size about 270×20×100 μm) system has been added on the lumped mass of the principal sensor in such a way as to detect the acceleration, and thus velocity, by time-integration, of the seismic mass. Also, two metallic armatures have been added on the lumped mass and the base frame of the sensor in such a way as to get an electro-dynamic control actuator. In this way absolute damping force could be generated on the seismic mass of the principal sensor by driving this actuator with a negative signal proportional to the measured velocity of the seismic mass.

The theoretical work presented in this report shows that if the active damping feedback control force generated by the control system embedded in the velocity sensor is properly tuned, then the output signal for the velocity sensor will not be anymore proportional to the acceleration of the base frame but it will be proportional to the opposite sign of the velocity of the base frame. This is an important outcome since the sensor will provide directly the negative velocity signal that is necessary to drive the closely located piezoelectric patch actuator in such a way as to implement a velocity feedback control loop and thus active damping on the structure. Thus, with this type of velocity sensor the measured signal could be directly feedback to the piezoelectric patch actuator without any need for time-integration.

The report is subdivided in four sections. In section two a mobility model is derived in order to obtain the theoretical response of a rectangular plate, subjected to a primary force when an ideal velocity sensor is coupled to either a collocated skyhook force or a closely located piezoelectric patch actuator in order to implement DVFB control. Section three describes the fundamental concepts of an inertial accelerometer made with a spring-mass system. The frequency response function between such an inertial accelerometer sensor with an R-C time integrator circuit and a closely located piezoelectric patch actuator is then considered in order to assess the stability of a direct velocity feedback loop. Also a parametric study is presented in order to highlight the effects generated on the sensor–actuator frequency response function by the size and the weight of the actuator and by the natural frequency and the damping coefficient of the sensor. Section four introduces the

concept of the velocity sensor made with a spring-mass system with embedded a direct velocity feedback control loop. The frequency response function between such a velocity sensor and a closely located piezoelectric patch actuator is then studied considering the cases where the velocity feedback loop embedded in the principal spring-mass system uses either an ideal velocity sensor or a second spring-mass accelerometer sensor with an R-C time integrator circuit mounted on the mass of the principal sensor. The stability of a direct velocity feedback control loop using this velocity sensor and the closely located piezoelectric patch actuator is then assessed.

## 2. SMART PANELS WITH ACTIVE DAMPING CONTROL UNITS

The aim of this section is to introduce the general concept of active damping in structures using collocated or closely located sensor actuator pairs which implement direct velocity feedback. This type of control systems could be used in many applications although the study presented in this report is focussed on smart panels with multiple an independent active damping control units.

### 2.1 Active damping using Direct Velocity Feedback (DVFB)

First of all the fundamental concept of active damping is introduced by analysing the illustrative problem of the isolation of an inertial mass from the vibrations of the base structure to which is mounted via an elastic mount. As shown in Figure 1, a conventional passive connecting system consists of a compliant mount positioned between the base system and the equipment to be isolated which can provide a good level of isolation in the high frequencies range, above the resonance caused by the mass $m$ of the equipment and the stiffness $k$ of the mount.

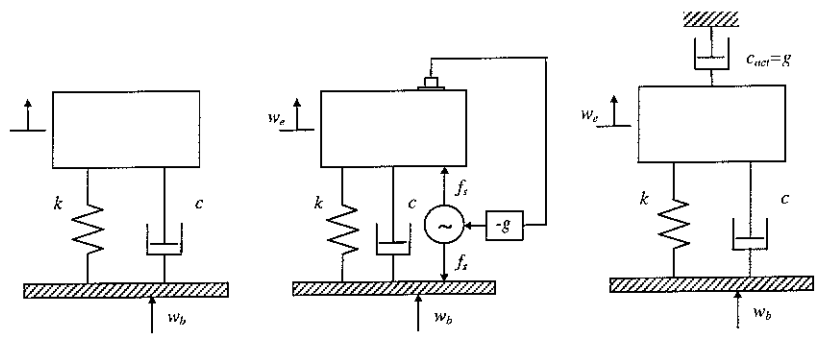


**Figure 1:** *Scheme of a characteristic isolation system: a) with passive damper; b) with both passive and active dampers; c) with a passive damper and an equivalent skyhook passive damper to the active damper.*

However, in order to obtain this good high-frequency isolation, the damping present in the mount must be small, in which case, as shown in Figure 2a, the lightly damped resonance of the mass-spring system produces large vibration transmission. This behaviour emphasizes the

main problem of a passive isolation: an inherent trade-off between high frequency isolation and amplification of the vibration at the basic mounted resonance frequency.

Active control could be employed to solve this intrinsic problem of passive isolation of vibration via a compliant mounting system. In particular, feedback control could be used so that broadband disturbances would be controlled. The simplest way for enhancing the damping at the mounted frequency is by implementing the so called direct velocity feedback (DVFB) where, as shown in Figure 1b, the measured velocity of the seismic mass is directly fed back to an actuator via a fixed control gain [3,5,7]. As shown in Figure 1c, this active technique is equivalent to providing a passive damper between the equipment and the inertial ground, which has been termed "skyhook active damping".

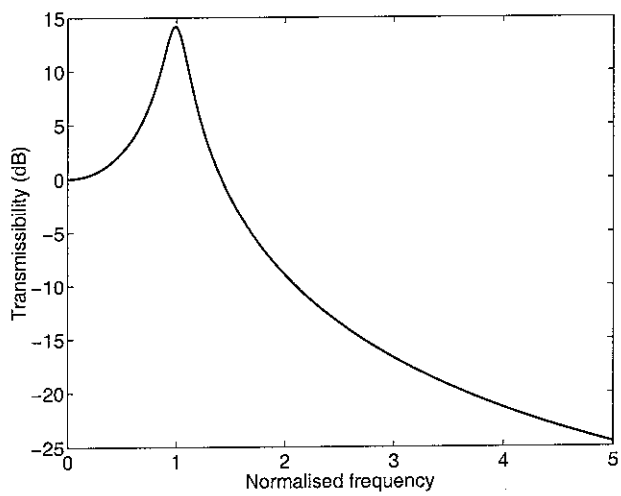


**Figure 2a:** *transmissibility of the system shown in Figure 1a which has a passive damping ratio of $\zeta_{pass}$=0.1 and no active damping.*

According to the scheme shown in figure 1a, the ratio between the amplitudes of the harmonic vibration of the mass, $W_e$, and the base, $W_b$, has been derived in reference [7] to be given by:

$$T(\Omega)=\frac{W_e(\Omega)}{W_b(\Omega)}=\frac{1+2j\zeta_{pass}\Omega}{1-\Omega^2+2j(\zeta_{pass}+\zeta_{act})\Omega}, \tag{2.1}$$

where $m$ is the mass of the equipment, $k$ and $c$ are respectively the stiffness and the damping of the mount, $\Omega = \frac{\omega}{\sqrt{km}}$ is the normalized frequency, $\zeta_{pass} = \frac{c}{2\sqrt{km}}$ is the passive damping and $\zeta_{act} = \frac{g}{2\sqrt{km}}$ is the active damping with $g$ the feedback gain.

Figure 2b shows the transmissibility $T$ as a function of the normalized frequency for the passive isolation system with a lightly damped mount ($\zeta_{pass}$=0.1) or heavily damped mount ($\zeta_{pass}$=0.7) and considering a lightly damped mount ($\zeta_{pass}$=0.1) whose damping is enhanced by the feedback control system ($\zeta_{act}$=0.6). Although passive damping tends to reduce the amplification of the vibration transmission at low frequency, it also tends to degrade the higher frequencies. However, as shown by the faint line, the active damping gives reduction of the resonance peak of the structure without degrading the response roll off beyond the resonance frequency.

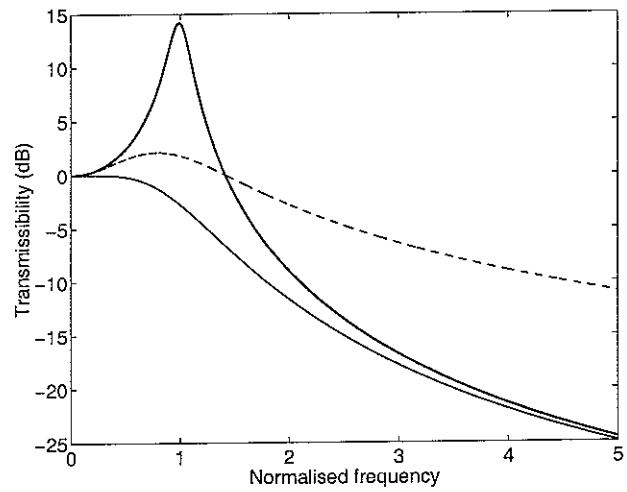


**Figure 2b:** *Transmissibility of the system shown in Figure 1 when the mounting system is lightly damped by a passive damper with $\zeta_{pass}$=0.1 (solid line), or heavily damped by a passive damper with $\zeta_{pass}$=0.7 (dashed line) or heavily damped by a passive damper with $\zeta_{pass}$=0.1 and an active damper $\zeta_{act}$=0.6 (faint line).*

In the next part of this report this type of feedback control loop is studied with reference to the problem of active structural acoustic control in panels using a closely located velocity sensor and piezoelectric patch actuator.

## 2.2 Smart panel with a Direct Velocity Feedback control unit

The concepts introduced in the previous section form the basis for the study of direct velocity feedback control (DVFB) in a smart panel as schematically shown in Figure 4 below. Two types of DVFB control systems are considered which use either a collocated velocity sensor and point force actuator or a closely located velocity sensor and a piezoelectric patch actuator. The dimensions and physical properties of the panel are summarised in Table 1 below.

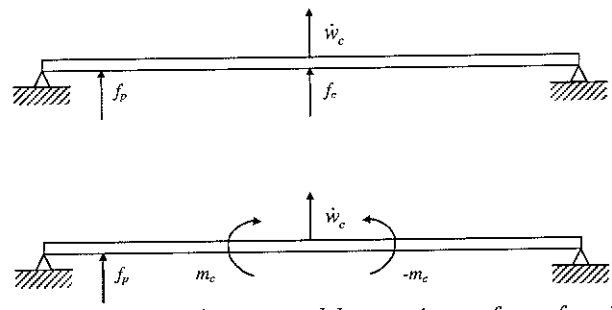


**Figure 4:** *Scheme of a simple supported plate excited by a primary force $f_p$. with either a collocated ideal velocity sensor and force actuator feedback control system (top scheme) or a closely located ideal velocity sensor and a massless piezoelectric patch strain actuator (bottom scheme) feedback control systems.*

**Table 1:** *Geometry and physical constants for the panel.*

| Parameter | Value |
|---|---|
| Dimensions | $l_x \times l_y$=414×314 mm |
| Thickness | $h_s$=1 mm |
| Position of the primary excitation | $x_p$, $y_p$=0.15$l_x$, 0.44$l_y$ mm |
| Mass density | $\rho_s$=2700 kg/m$^3$ |
| Young's modulus | $E_s$=7×10$^{10}$ N/m$^2$ |
| Poisson ratio | $\nu_s$=0.33 |
| Loss factor | $\eta_s$=0.05 |

Throughout this report the mechanical cinematic (linear-angular displacements, velocities, accelerations) or kinetic functions (forces or moments) as well as the electric functions (voltage or current) have been assumed to be time-harmonic and given by the real part of counter clockwise rotating complex vectors, i.e. phasors. The following notation has therefore been used where, for example, a time harmonic displacement or force are given by $w(t) = \mathrm{Re}\{w(\omega)e^{j\omega t}\}$ or $f(t) = \mathrm{Re}\{f(\omega)e^{j\omega t}\}$, where $\omega$ is the circular frequency in [rad/s]. Thus $w(t)$ and $f(t)$ are the time-harmonic displacement and force functions while $w(\omega)$ and $f(\omega)$ are the complex frequency-dependent displacement and force phasors. In order to

simplify the formulation presented in this report, the harmonic time dependence is implicitly assumed in the mathematical expressions which are therefore formulated in terms of the frequency-dependent phasors. Also, the first and second derivative of the time-harmonic functions, for example the linear velocity, $\dot{w}(t) = \mathrm{Re}\left\{j\omega w(\omega)e^{j\omega t}\right\}$, or linear acceleration, $\ddot{w}(t) = \mathrm{Re}\left\{-\omega^2 w(\omega)e^{j\omega t}\right\}$ will be represented by velocity and acceleration frequency-dependent phasors $\dot{w}(\omega) = j\omega w(\omega)$ and $\ddot{w}(\omega) = -\omega^2 w(\omega) = j\omega\dot{w}(\omega)$.

The phasors of the velocities on a generic point of the plate structure $\dot{w}_s(x,y,\omega)$ and at control sensor position $\dot{w}_c(x_c,y_c,\omega)$ can be expressed in terms of the primary and control excitations as follows [8]:

$$\dot{w}_s(x,y,\omega) = Y_{sp}(x,y,\omega)f_p + Y_{sc}(x,y,\omega)u_c(\omega), \tag{2.2}$$

$$\dot{w}_c(\omega) = Y_{cp}(\omega)f_p + Y_{cc}(\omega)u_c(\omega), \tag{2.3}$$

where $f_p$ is the primary excitation and $u_c$ the control signal. The stiffening and the mass effects of the piezoelectric patch actuator are not taken into account in the model. The four mobility terms in equations 2.2 and 2.3 are given by [8]:

$$Y_{sp}(x,y,\omega) = \phi(x,y)\mathbf{a}_{\mathrm{p}}(\omega), \tag{2.4}$$

$$Y_{sc}(x,y,\omega) = \phi(x,y)\mathbf{a}_{\mathrm{c}}(\omega), \tag{2.5}$$

$$Y_{cp}(\omega) = \phi_{\mathrm{c}}(x_c,y_c)\mathbf{a}_{\mathrm{p}}(\omega), \tag{2.6}$$

$$Y_{cc}(\omega) = \phi_{\mathrm{c}}(x_c,y_c)\mathbf{a}_{\mathrm{c}}(\omega), \tag{2.7}$$

where $\phi(x,y)$ and $\phi_{\mathrm{c}}(x_c,y_c)$ are row vectors with the first $N$ natural modes of the plate calculated in a generic point $(x,y)$ and in the control point $(x_c,y_c)$ respectively:

$$\phi(x,y) = [\phi_1(x,y) \quad \phi_2(x,y) \quad \ldots \quad \phi_N(x,y)], \tag{2.8}$$

$$\phi_c(x_c,y_c) = [\phi_1(x_c,y_c) \quad \phi_2(x_c,y_c) \quad \ldots \quad \phi_N(x_c,y_c)], \tag{2.9}$$

and $\mathbf{a}_p(\omega)$, $\mathbf{a}_c(\omega)$ are column vectors for the excitation terms of the first $N$ natural modes of the plate due to either the primary or control excitations:

$$\mathbf{a}_p(\omega) = \begin{bmatrix} a_{p,1}(\omega) \\ a_{p,2}(\omega) \\ \ldots \\ a_{p,N}(\omega) \end{bmatrix}, \qquad \mathbf{a}_c(\omega) = \begin{bmatrix} a_{c,1}(\omega) \\ a_{c,2}(\omega) \\ \ldots \\ a_{c,N}(\omega) \end{bmatrix}. \tag{2.10,11}$$

The terms in the vector relative to the primary excitation are given by

$$a_p(\omega) = j\omega \frac{\phi_{m,n}(x_p,y_p)}{\Lambda[\omega_{m,n}^2(1+j\eta_s)-\omega^2]}, \tag{2.12}$$

while the terms in the control vector, for the force and the moment pair control excitations, are respectively

$$a_{ci}(\omega) = j\omega \frac{\phi_{m,n}(x_c,y_c)}{\Lambda[\omega_{m,n}^2(1+j\eta_s)-\omega^2]}, \tag{2.13}$$

and

$$a_{ci}(\omega) = j\omega c_\alpha \frac{\psi_{m,n}(x_c,y_c)}{\Lambda[\omega_{m,n}^2(1+j\eta_s)-\omega^2]}, \tag{2.14}$$

where: $m$, $n$ are the modal indices, $\omega_{m,n}$ is the natural frequency of the $(m,n)$th mode of the plate, $\phi_{m,n}(x,y)$ is the $(m,n)$th natural mode of the plate at position $(x,y)$, $\psi_{m,n}(x,y)$ is the $(m,n)$th modal contribution of the piezoelectric patch actuator at position $(x,y)$, $\Lambda = \rho_s h_s l_x l_y / 4$ is the modal normalization parameter, $\rho_s$ the density of the material of the

plate, $h_s$, $l_x$ and $l_y$ are respectively the thickness and the dimension of the plate, and $\eta_s$ the hysteresis loss factor. The $(m,n)$th natural frequency and relative mode are respectively:

$$\omega_{m,n} = \sqrt{\frac{E_s I_s}{\rho_s h_s (1-\nu_s^2)}}\left[\left(\frac{m\pi}{l_x}\right)^2 + \left(\frac{n\pi}{l_y}\right)^2\right] = \sqrt{\frac{E_s h_s^2}{12\rho_s (1-\nu_s^2)}}\left[\left(\frac{m\pi}{l_x}\right)^2 + \left(\frac{n\pi}{l_y}\right)^2\right], \quad (2.15)$$

$$\phi_{m,n}(x,y) = \sin\left(\frac{m\pi x}{l_x}\right)\sin\left(\frac{n\pi y}{l_y}\right), \quad (2.16)$$

where $E_s$ and $\nu_s$ are respectively the Young's modulus and Poisson's ratio of the material of the plate and $I_s$ is the second moment of area of the plate.

**Table 2:** *Geometry and physical constants for the piezoelectric, PZT, patch.*

| Parameter | Value |
|---|---|
| Dimensions of the PZT patch | $a_x \times a_y$=30×30 mm |
| Centre position of the PZT patch | $x_c$, $y_c$=0.33$l_x$, 0.71$l_y$ mm |
| Thickness of the PZT patches | $h_{pe}$=0.5 mm |
| Density | $\rho_{pe}$=7650 kg/m$^3$ |
| Young's modulus | $E_{pe}$=2×10$^9$ N/m$^2$ |
| Poisson ratio | $\nu_{pe}$=0.29 |
| Strain constant | $d_{31}$=23×10$^{-12}$ m/V |

The $(m,n)$th modal contribution of the piezoelectric patch actuator is given by [2]:

$$\psi_{m,n}(x,y) = \int_0^{a_x} \psi^y_{m,n}(x_c, y_{c1}) - \psi^y_{m,n}(x_c, y_{c2})\, dx + \int_0^{a_y} \psi^x_{m,n}(x_{c1}, y_c) - \psi^x_{m,n}(x_{c2}, y_c)\, dy, \quad (2.17)$$

where $\psi^x_{m,n}(x,y)$ and $\psi^y_{m,n}(x,y)$ are respectively the first derivative in $x$ and $y$ direction of the natural mode and $a_x$, $a_y$ the dimension of the piezoelectric patch, $x_{c1}$, $x_{c2}$ are the $x$-positions of the two $a_y$ edges of the piezoelectric patch and $y_{c1}$, $y_{c2}$ are the $y$-positions of the two $a_x$ edges of the piezoelectric patch. Finally the actuation constant for the piezoelectric patch $c_\alpha$ is given by [10]:

$$c_\alpha = E_s I_s \frac{3E_{pe}\left[\left(\frac{h_s}{2}+h_{pe}\right)^2-\frac{h_s^2}{4}\right](1-\nu_s)}{2E_{pe}\left[\left(\frac{h_s}{2}+h_{pe}\right)^3-\frac{h_s^3}{8}\right](1-\nu_s)+2E_s\frac{h_s^3}{8}(1-\nu_{pe})}\frac{d_{31}}{h_{pe}}, \tag{2.18}$$

where the physical and geometrical properties of the patch are given in Table 2. From the previous definitions, the extensive form of the $Y_{cp}$ and $Y_{cc}$ is given by:

$$Y_{cp} = j\omega\sum_{m=1}^{\infty}\sum_{n=1}^{\infty}\frac{\phi_{m,n}(x_c,y_c)\phi_{m,n}(x_p,y_p)}{\Lambda[\omega_{m,n}^2(1+j\eta_s)-\omega^2]}, \tag{2.19}$$

$$Y_{cc} = j\omega\sum_{m=1}^{\infty}\sum_{n=1}^{\infty}\frac{\phi_{m,n}(x_c,y_c)\phi_{m,n}(x_c,y_c)}{\Lambda[\omega_{m,n}^2(1+j\eta_s)-\omega^2]}, \tag{2.20}$$

$$Y_{cc} = j\omega c_\alpha\sum_{m=1}^{\infty}\sum_{n=1}^{\infty}\frac{\phi_{m,n}(x_c,y_c)\psi_{m,n}(x_c,y_c)}{\Lambda[\omega_{m,n}^2(1+j\eta_s)-\omega^2]}. \tag{2.21}$$

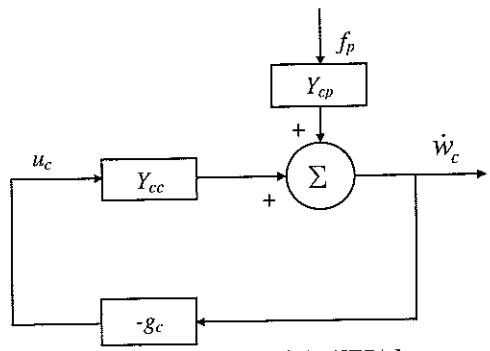


**Figure 5:** *block diagram of the direct velocity feedback (DVFB) loop control implemented on the plate.*

According to the block diagram shown in Figure 5 for the two control loops, when there is no control, that is $u_c(\omega)$=0, the velocity of a generic point of the plate is:

$$\dot{w}_s(x,y,\omega) = Y_{sp}(x,y,\omega)f_p. \tag{2.22}$$

Alternatively, if the sensor-actuator pair implements the DVFB control loop such that:

$$u_c = -g_c \dot{w}_c , \tag{2.23}$$

then, substituting equation (2.22) in (2.3) and solving respect the velocity $\dot{w}_c$ at the error position, the velocity at control point is given by:

$$\dot{w}_c = \frac{Y_{cp}}{1 + g_c Y_{cc}} f_p . \tag{2.24}$$

This formula shows that if $Y_{cc}$ is real and positive then as the control gain $h_c$ is raised as the vibration amplitude at the control position falls down.

It is convenient to represent the overall vibration of the plate in terms of the total kinetic energy which is given by the formula [8]:

$$K(\omega) = \frac{1}{2} \int_A \rho h \left| \dot{w}(x, y) \right|^2 dA . \tag{2.25}$$

Substituting equations (2.7) and (2.23) in (2.24), then the kinetic energy of the plate without the feedback control, i.e. $g_c = 0$:

$$K(\omega) = \frac{1}{4} M f_p^* \mathbf{a}_{\mathrm{p}}^{\mathrm{H}} \mathbf{a}_{\mathrm{p}} f_p , \tag{2.26}$$

and for the plate with the feedback control:

$$K(\omega) = \frac{1}{4} M f_p^* \left[ \mathbf{a}_{\mathrm{p}} + \mathbf{a}_{\mathrm{fc}} \right]^H \left[ \mathbf{a}_{\mathrm{p}} + \mathbf{a}_{\mathrm{fc}} \right] f_p , \tag{2.27}$$

where $M$ is the mass of the plate, * represents the conjugate, $H$ the Hermitian transpose and $\mathbf{a}_{\mathrm{fc}}$ is a column vector with the modal excitation terms due to the control loop and are given by:

$$\mathbf{a}_{fc} = \mathbf{a}_c \frac{-g_c Y_{cp}}{1 + g_c Y_{cc}}. \tag{2.28}$$

Equations (2.26) and (2.27) enables the derivation of the total flexural kinetic energy in the 0--1 kHz frequency range, which is shown in Figures 6 and 7, and the 0-1 kHz ratio between the frequency-averaged total flexural kinetic energy with and without feedback control for a range control gains between 1 and $10^6$, which is shown in Figures 8 and 9.

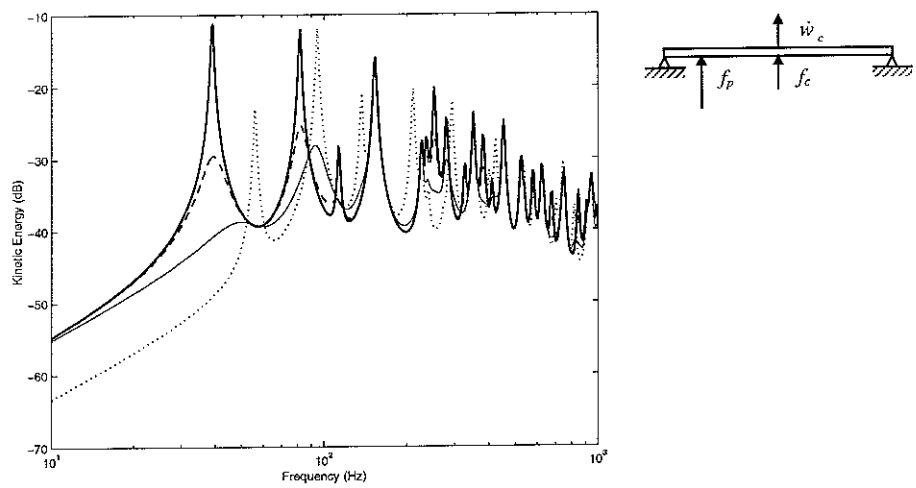


**Figure 6:** *total flexural kinetic energy of the plate when it is excited by a unit primary force and the control gains of the feedback control system using a force actuator are set to be 0 (solid line), 7.7 (dashed line), 33.3 (faint line) and $10^6$ (faint line).*

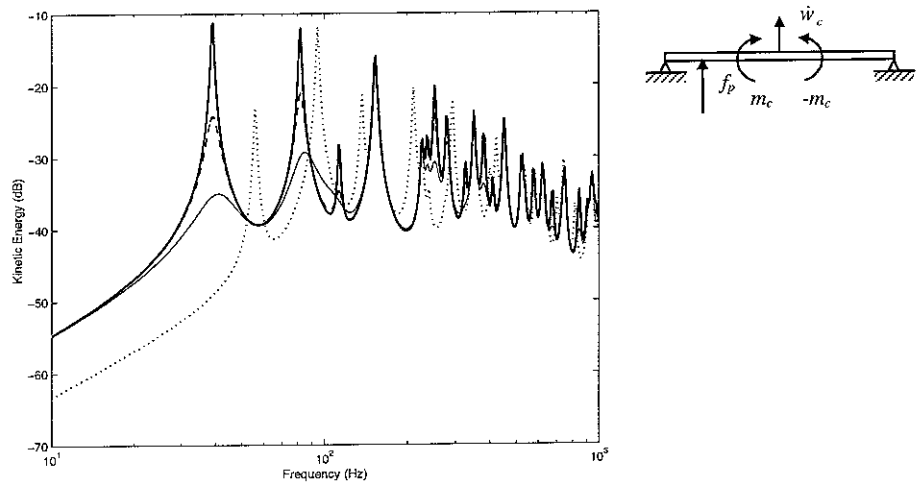


**Figure 7:** *total flexural kinetic energy of the plate when it is excited by a unit primary force and the control gains of the feedback control system using a piezoelectric patch actuator are set to be 0 (solid line), 7.7 (dashed line), 33.3 (faint line) and $10^6$ (faint line).*

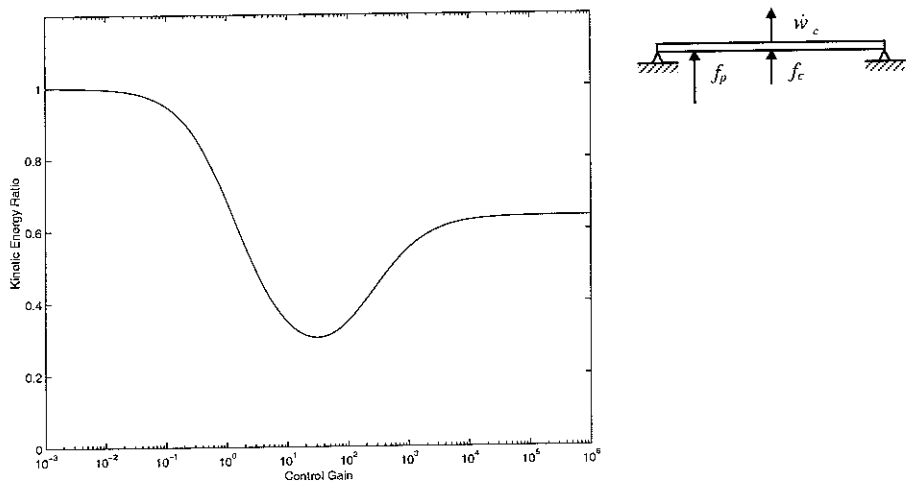


**Figure 8:** *ratio between the 0 to 1 kHz frequency averaged total kinetic energy of the plate with and without feedback control plotted against the gain in the feedback controller using the force actuator.*

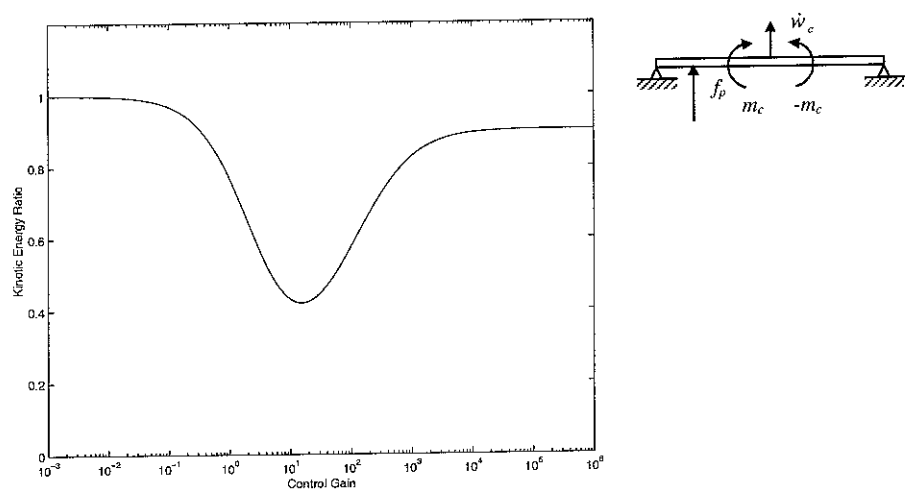


**Figure 9:** *ratio between the 0 to 1 kHz frequency averaged total kinetic energy of the plate with and without feedback control plotted against the gain in the feedback controller using the piezoelectric patch actuator.*

Figures 6 and 7 show the active damping effects and the subsequent rearrangement of the modal responses of the plate when the gain of the DVFB control loop increases [1]. From these figures it is possible to highlight two important behaviours. First, there is an optimal gain that reduces the kinetic energy substantially. Second, with relatively larger gains than the optimal value, the system rearranges its modal response and new resonance peaks come into sight [8]. This characteristic behaviour is exemplified in the Figures 8 and 9 where the minimum value of the ratio of the 0 to 1 kHz frequency averaged kinetic energy of the plate with and without the feedback control corresponds to the optimal gain while for bigger gains than this one the ratio of the kinetic energies increases.

It must be emphasised that the results presented in this section have been derived assuming the two control systems unconditionally stable. In the following section the true stability limits are assessed in details.

## 2.3 Stability of the Direct Velocity Feedback loop

A critical problem in feedback control system design is stability. In the previous sections this feature was omitted in order to focus the attention on the concept of active damping and DVFB. There are two necessary requirements in order to have an unconditionally stable system: the sensor-actuator pair must be dual and collocated [4,5]. Duality means that the actuation and sensing mechanisms occurs with reference to the same type of degree of freedom. Collocation means that the sensor and the actuator operate on the same position. In this case the sensor actuator response function corresponds to a point mobility of the structure, $Y_{cc}$, which intrinsically has real part positive for any frequency. In fact, the power supplied by a collocated and dual velocity sensor and force actuator control unit is given by

$$P = \frac{1}{2}\mathrm{Re}(f_c^* \dot{w}_c) = \frac{1}{2}\mathrm{Re}(f_c^* Y_{cc} f_c) = \frac{1}{2}|f_c|^2 \,\mathrm{Re}(Y_{cc})\,. \tag{2.29}$$

By definition this term is positive and thus the response function $Y_{cc}$ must have real part positive definite. According to the block diagram in Figure 5, the ratio between the velocity $\dot{w}_c$ at the control position and the primary disturbance $f_p$ is given by:

$$\frac{\dot{w}_c}{f_p} = \frac{Y_{cp}}{1 + g_c Y_{cc}}, \tag{2.30}$$

where $Y_{cc}$ is the frequency response function between the sensor and the actuator pair. Since $\mathrm{Re}(Y_{cc})>0$, then equation (2.30) shows that $\dot{w}_c / f_p < 1$ for any control gain and frequency, that is the feedback control loop monotonically decreases the velocity of the structure at the error position for any control gain and frequency. Thus a feedback control system is unconditionally stable when the real part of the sensor–actuator frequency response function

is positive real for all frequencies. Therefore the phase of the sensor–actuator frequency response function must be between ±90° [11-13].

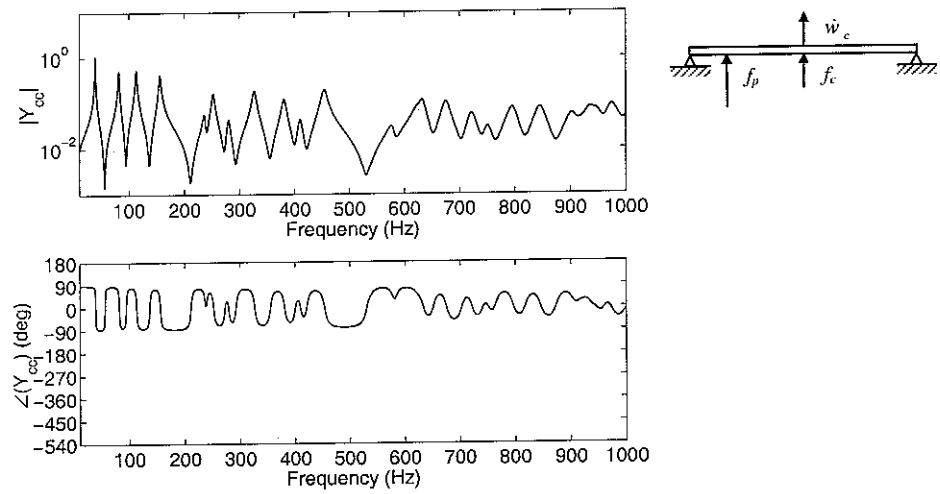


**Figure 10:** *frequency response amplitude (top plot) and phase (bottom plot) between a collocated ideal velocity sensor and force actuator in the 0-1 kHz frequency range.*

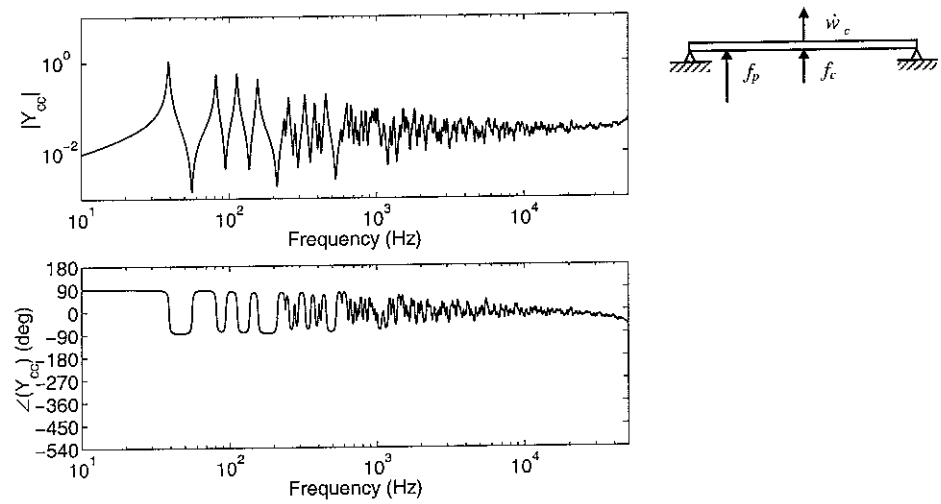


**Figure 11:** *frequency response amplitude (top plot) and phase (bottom plot) between a collocated ideal velocity sensor and force actuator in the 10 Hz-50 kHz frequency range.*

This is a very stringent condition that could be relaxed by adopting the Nyquist criterion for stability which states that provided the plot of the real part versus the imaginary part of the open loop sensor–actuator frequency response function, $Y_{cc}$, also known as the Nyquist plot of $Y_{cc}$, does not encircle the Nyquist point $-1+j0$, then the control system is stable [11-13]. However this criterion must be used with care since it intrinsically implies a limitation on the control gains in the cases where the sensor–actuator frequency response function enter on the

left hand side of the Nyquist plot. These limitations are usually expressed in terms of either phase or amplitude gain margins as described in references [11-13].

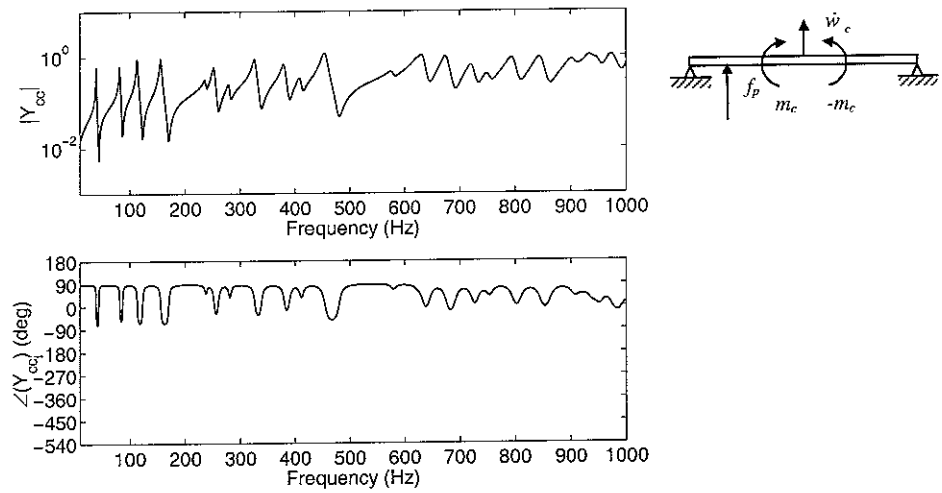


**Figure 12:** *frequency response amplitude (top plot) and phase (bottom plot) between a collocated ideal velocity sensor and a piezoelectric patch strain actuator without mass in the 0-1 kHz frequency range.*

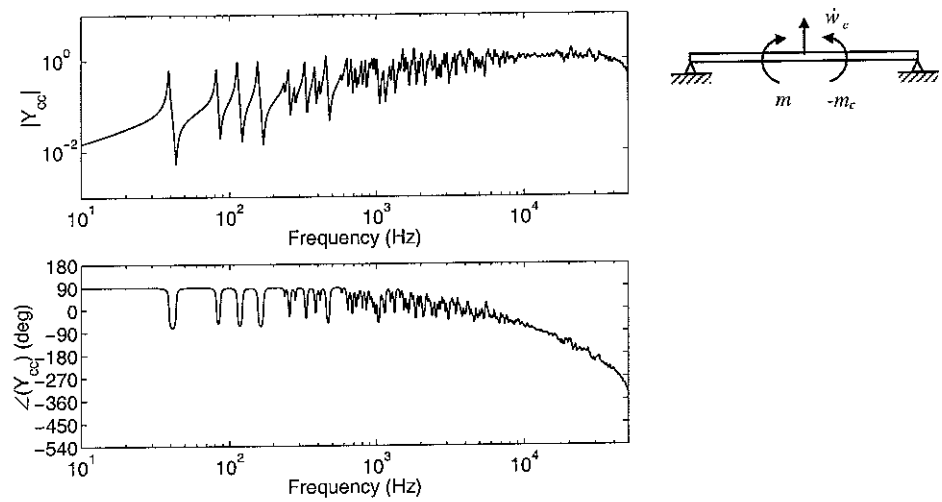


**Figure 13:** *frequency response amplitude (top plot) and phase (bottom plot) between a collocated ideal velocity sensor and a piezoelectric patch strain actuator without mass in the 10 Hz-50 kHz frequency range.*

Figures 10 and 12 and Figures 11 and 13 show the amplitude and phase of the sensor–actuator frequency response functions for the two control systems in Figure 4 in the frequency ranges between 0 and 1 kHz and between 10 and 50 kHz. Figures 10 and 11 confirm that the frequency response function of a collocated and dual velocity sensor and force actuator pair is positive real and thus provides an unconditionally stable control system. In contrast Figure 13 shows that the closely located velocity sensor and piezoelectric patch actuator pair does not

provide an unconditionally stable feedback system since above about 10 kHz the phase of the sensor–actuator frequency response function exceed -90° which implies a negative real part. It is interesting to highlight that, as shown in Figure 11, the force actuator efficiently excites the panel at low frequency while, as shown in Figure 13, the moment excitation of the piezoelectric patch actuator efficiently excites the panel at higher frequencies.

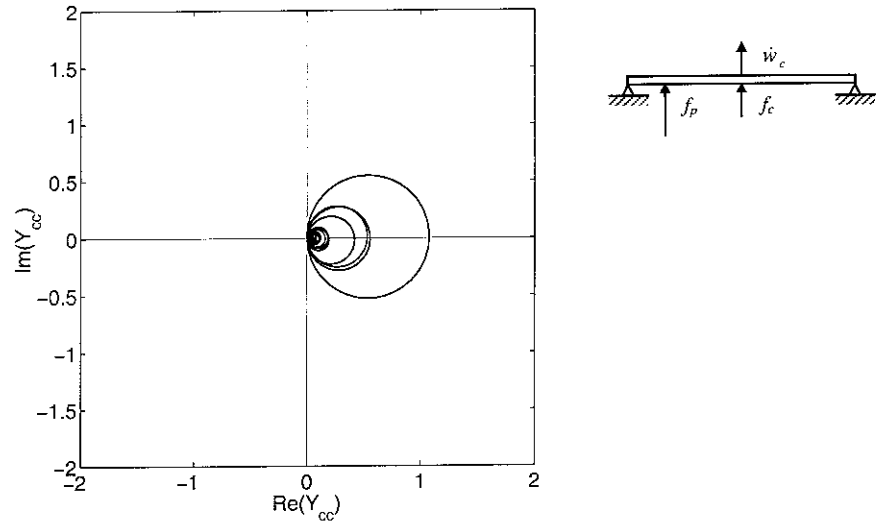


**Figure 14:** *Nyquist plot of the frequency response function between a collocated ideal velocity sensor and force actuator in the 10 Hz-50 kHz frequency range.*

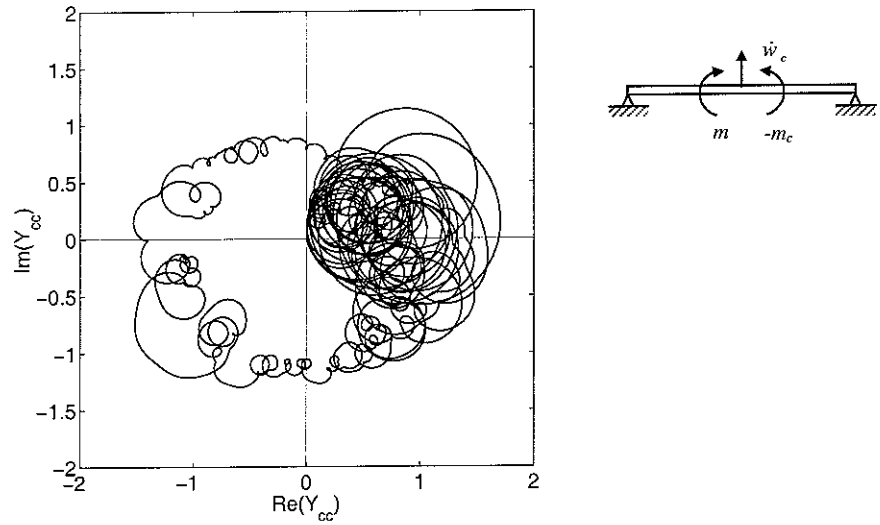


**Figure 15:** *Nyquist plot of the frequency response function between a collocated ideal velocity sensor and a massless piezoelectric patch strain actuator in the 10 Hz-50 kHz frequency range.*

Figures 14 and 15 show the Nyquist plots for the two control systems: the first one is entirely on the right hand side, which confirms the unconditional stability of the velocity sensor and force actuator system, while the second one enters the left hand side at higher frequencies

above 10 kHz. The plot in Figure 15 shows that, because the piezoelectric patch efficiently excites the plate at higher frequencies, then the left hand side of the Nyquist plot is relatively bigger to that on the right hand side which implies there is no gain margin and thus it is not possible to implement even small control gains.

# 3. DVFB USING AN ACCELEROMETER SENSOR AND CONSIDERING THE MASS EFFECT OF THE PIEZOELECTRIC PATCH ACTUATOR

The stability analysis presented in the previous chapter considers a sensor-actuator pair in which the sensor is an ideal transducer that detects the transverse velocity of a panel and the piezoelectric patch actuator is an ideal transducer that exerts line moments along the four edges. In this chapter the dynamics effects of a practical accelerometer sensor and the mass effect of the piezoelectric patch actuator will be taken into account in the stability analysis.

## 3.1 Accelerometer response function

A practical sensor that could be used in the control system studied in this report is the accelerometer [5]. As shown in Figure 16, this type of device is made of a seismic mass $m_a$ connected to a vibrating base via a spring of stiffness $k_a$ and a dashpot with a damping coefficient $c_a$.

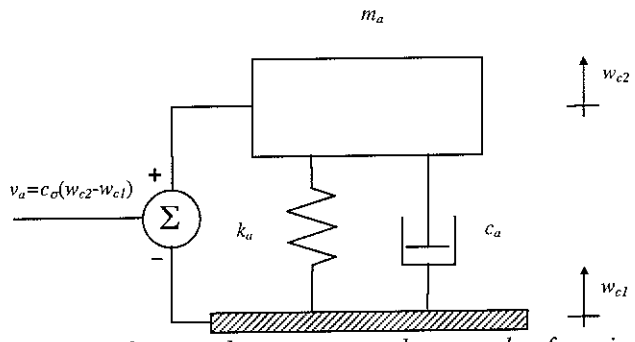


**Figure 16:** *schematic representation of an accelerometer transducer made of a seismic mass $m_a$, which is suspended on the vibrating base via a spring, of stiffness $k_a$, and a damper with damping coefficient $c_a$.*

The spring is normally made of a piezoelectric transducer which generates a voltage signal $v_a$ proportional to the relative displacement between the mass and the base [5]:

$$v_a = c_\sigma \, (w_{c2} - w_{c1}), \tag{3.1}$$

where $c_\sigma$ is the detection constant of the piezoelectric elastic element: The formulation below shows that, for frequencies below the fundamental resonance frequency of the accelerometer system the output signal is directly proportional to the acceleration of the vibrating base. The equation of motion for the system shown in Figure 16 can be derived by applying Newton's second law, so that:

$$m_a \ddot{w}_{c2} = -c_a(\dot{w}_{c2} - \dot{w}_{c1}) - k_a(w_{c2} - w_{c1}), \tag{3.2}$$

where $w_{c1}$ and $w_{c2}$ are the displacements of the base and of the mass respectively. If the relative displacement between the seismic mass and the base is defined as:

$$z = w_{c2} - w_{c1}, \tag{3.3}$$

then the equation of motion can be rewritten in the following form

$$m_a \ddot{z} + c_a \dot{z} + k_a z = -m_a \ddot{w}_{c1}. \tag{3.4}$$

According to the notation introduced in section 2.2, the harmonic motions of the base and seismic mass are defined as:

$$w_{c1}(t) = \mathrm{Re}\left\{w_{c1}(\omega)e^{j\omega t}\right\}, \qquad w_{c2}(t) = \mathrm{Re}\left\{w_{c2}(\omega)e^{j\omega t}\right\} \tag{3.5a,b}$$

and thus

$$z(t) = \mathrm{Re}\left\{z(\omega)e^{j\omega t}\right\}, \tag{3.6}$$

where $w_{c1}(\omega)$, $w_{c2}(\omega)$ are respectively the phasors of the motion of the base and suspended mass, $z(\omega)$ is the phasor of the relative displacement between the mass and the base. Substituting equations (3.5a,b) and (3.6) into equation (3.4) it is found:

$$(-\omega^2 m_a + j\omega c_a + k_a) z e^{j\omega t} = \omega^2 m_a w_{c1} e^{j\omega t}. \tag{3.7}$$

With equation (3.7) it is possible to derive the phasor of the relative displacement $z(\omega)$ with reference to either:

**1) the phasor of the base displacement** $w_{c1}(\omega)$

$$\frac{z(\omega)}{w_{c1}(\omega)} = \frac{\omega^2 m_a}{(k_a - \omega^2 m_a) + j\omega c_a} = \frac{\dfrac{\omega^2}{\omega_a^2}}{\left(1 - \dfrac{\omega^2}{\omega_a^2}\right) + j2\zeta_a \dfrac{\omega}{\omega_a}}, \tag{3.8a}$$

**2) the phasor of the base velocity** $\dot{w}_{c1}(\omega) = j\omega w_{c1}(\omega)$

$$\frac{z(\omega)}{j\omega w_{c1}(\omega)} = \frac{z(\omega)}{\dot{w}_{c1}(\omega)} = \frac{-j\omega m_a}{(k_a - \omega^2 m_a) + j\omega c_a} = \frac{-j\dfrac{\omega}{\omega_a^2}}{\left(1 - \dfrac{\omega^2}{\omega_a^2}\right) + j2\zeta_a \dfrac{\omega}{\omega_a}}, \tag{3.8b}$$

**3) the phasor of the base acceleration** $\ddot{w}_{c1}(\omega) = -\omega^2 w_{c1}(\omega)$

$$\frac{z(\omega)}{-\omega^2 w_{c1}(\omega)} = \frac{z(\omega)}{\ddot{w}_{c1}(\omega)} = \frac{-m_a}{(k_a - \omega^2 m_a) + j\omega c_a} = \frac{-\dfrac{1}{\omega_a^2}}{\left(1 - \dfrac{\omega^2}{\omega_a^2}\right) + j2\zeta_a \dfrac{\omega}{\omega_a}}. \tag{3.8c}$$

where $\omega_a = \sqrt{k_a / m_a}$ and $\zeta_a = c_a / 2\sqrt{k_a m_a}$ are respectively the natural frequency and damping ration of the mass–spring system. These three expressions can be rewritten in terms of the complex frequency response of a single degree of freedom system [5]:

$$H\left(\frac{\omega}{\omega_a}\right) = \frac{1}{\left(1 - \dfrac{\omega^2}{\omega_a^2}\right) + j2\zeta_a \dfrac{\omega}{\omega_a}}, \tag{3.9}$$

so that

$$\frac{z}{w_{c1}} = \frac{\omega^2}{\omega_a^2}\left|H\left(\frac{\omega}{\omega_a}\right)\right| e^{-j\phi}, \tag{3.10a}$$

$$\frac{z}{\dot{w}_{c1}} = -j\frac{\omega}{\omega_a^2}\left|H\left(\frac{\omega}{\omega_a}\right)\right| e^{-j\phi}, \tag{3.10b}$$

$$\frac{z}{\ddot{w}_{c1}} = -\frac{1}{\omega_a^2}\left|H\left(\frac{\omega}{\omega_a}\right)\right| e^{-j\phi}, \tag{3.10c}$$

where

$$\left|H\left(\frac{\omega}{\omega_a}\right)\right| = \frac{1}{\left[\left(1-\frac{\omega^2}{\omega_a^2}\right)^2 + \left(2\zeta_a\frac{\omega}{\omega_a}\right)^2\right]^{\frac{1}{2}}}, \qquad \tan\phi = \frac{2\zeta_a\frac{\omega}{\omega_a}}{1-\left(\frac{\omega}{\omega_a}\right)^2}. \tag{3.11a,b}$$

If $\omega << \omega_a$ then $\left|H\left(\frac{\omega}{\omega_a}\right)\right| \cong 1$ and $\phi \cong 0$ while if $\omega >> \omega_a$ then $\left|H\left(\frac{\omega}{\omega_a}\right)\right| \cong \frac{\omega_a^2}{\omega^2}$ and $\phi \cong 180^o$. Finally at resonance, so that $\omega = \sqrt{1-2\zeta_a^2}\,\omega_a$, $\left|H\left(\frac{\omega}{\omega_a}\right)\right| = \frac{1}{2\zeta_a\sqrt{1-\zeta_a^2}}$ and $\phi \cong 90^o$. Thus, according to equation (3.10a) and as shown in Figure 17a, for frequencies beyond the fundamental resonance frequency $\omega >> \sqrt{1-2\zeta_a^2}\,\omega_a$, $\frac{z}{w_{c1}} \to -1$ so that the accelerometer voltage output is proportional to opposite displacement of the base $v_a \cong -c_\sigma w_{c1}$. Similarly, considering equation (3.10c) and as shown in Figure 17c, for frequencies below the fundamental resonance frequency $\omega << \sqrt{1-2\zeta_a^2}\,\omega_a$, $\frac{z}{\ddot{w}_{c1}} \to -\frac{1}{\omega_a^2}$ so

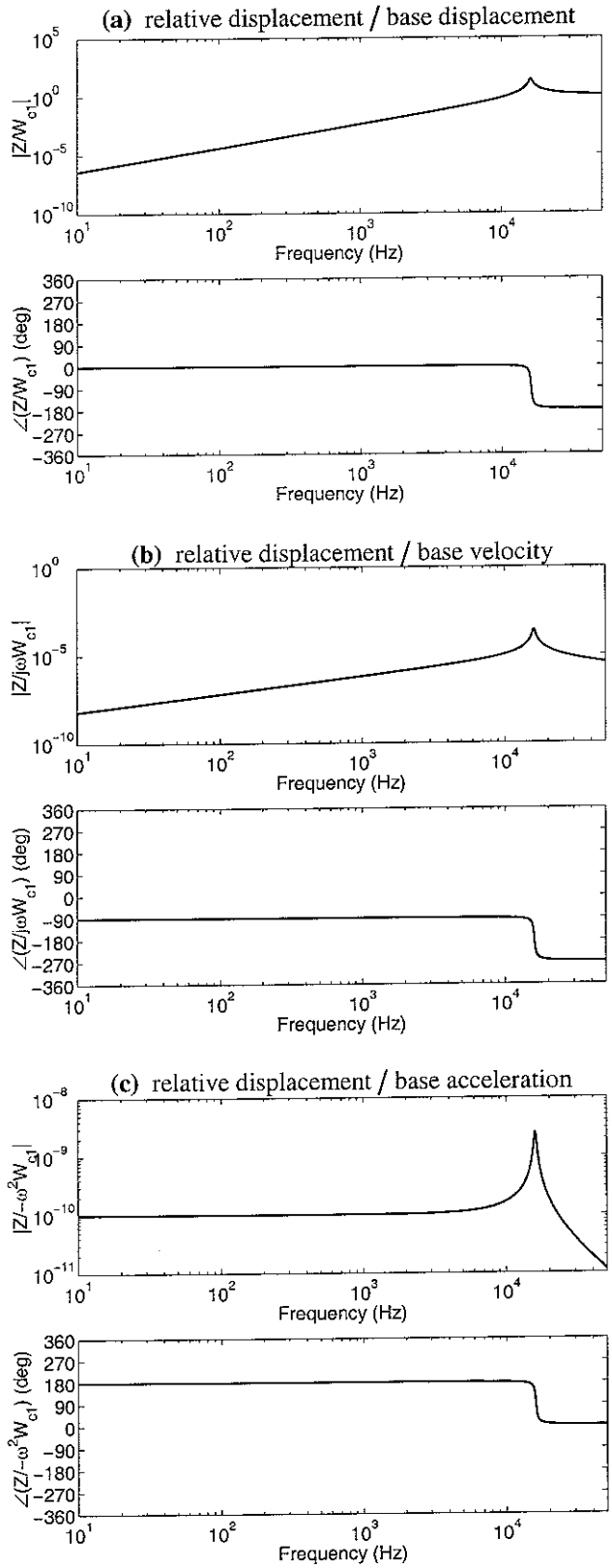


**Figure 17:** *amplitude (top plots) and phase (bottom plots) of the accelerometer relative displacement $z=w_{c2}-w_{c1}$ per unit amplitude of the base a) displacement, b) velocity and c) acceleration.*

that the accelerometer voltage output is in this case proportional to opposite acceleration of the base $v_a \cong -\frac{c_\sigma}{\omega_a^2}\ddot{w}_{c1}$. Finally as one can deduce from equation (3.10b) and as shown in Figure 17b, there is no relationship of proportionality between the relative displacement of the sensor and the velocity of the base apart from the case where $\omega = \omega_a$ and $z/\dot{w}_{c1} = -1/2\zeta_a$.

In summary, as shown in Figure 17c, at frequencies below resonance, the accelerometer sensor provides a voltage output proportional to the opposite of the base acceleration. The output signal is inversely proportional to the natural frequency of the sensor itself. Thus, as the frequency band of measurement is increased as the natural frequency must be higher and thus the sensitivity of the accelerometer is reduced. In principle this type of sensor could be used in a velocity feed back loop if the output signal is integrated in time so as it would be proportional to velocity. In the following sections the feedback system considered in section 2.3 is studied by taking into account the true response of an accelerometer sensor made with a suspended mass on an elastic transducer considering either an ideal time integrator or a practical R-C integrator circuit [12].

## 3.2 Sensor–actuator response function when the dynamics of the accelerometer is taken in to account

In this section the frequency response functions between the accelerometer sensor with an ideal time integrator and either a collocated point control force $f_c$ or the four line of moments, $m_s$, generated by the closely located piezoelectric patch actuator are studied.

Figure 18 illustrates in details the forces and displacements acting on the elements of the accelerometer sensor which is mounted on the plate at the control point. In order to derive the fully coupled equations of motion of the plate and accelerometer systems, the accelerometer has been divided in two elements: the mounting elastic system which is made by a spring, $k_a$, and dashpot, $c_a$, in parallel and the seismic mass $m_a$. Thus the whole system is made of three parts: the plate and the two elements of the accelerometer.

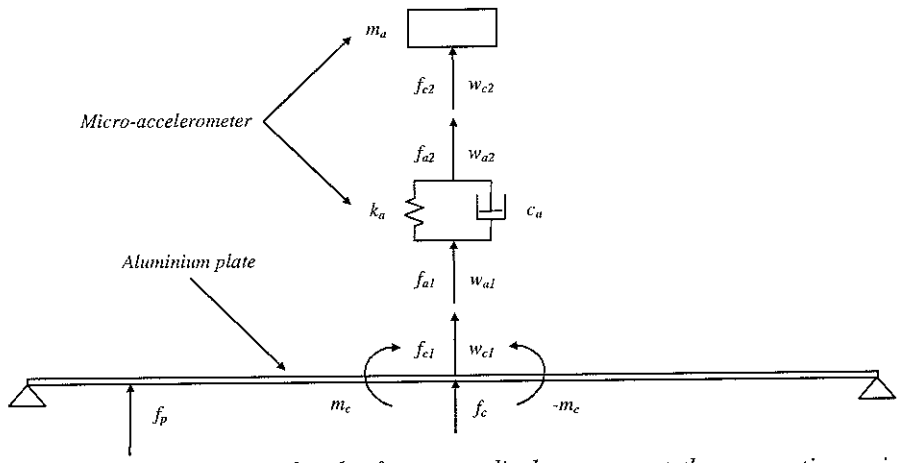


**Figure 18:** *scheme with the notation for the forces an displacements at the connecting points between the elements of the accelerometer which is mounted on an aluminium plate with either a collocated force actuator or closely located piezoelectric patch actuator that generates lines of moments along the four edges.*

The velocity $\dot{w}_{c1}$ of the plate and $\dot{w}_{c2}$ of the accelerometer suspended mass can be derived using the mobility approach as seen in section 2.2, so that:

$$\begin{cases} \dot{w}_{c1} = Y_{11} f_{c1} + Y_{cp} f_p + Y_{cc} u_c \\ \dot{w}_{c2} = Y_{22} f_{c2} \end{cases}, \tag{3.12}$$

where $Y_{11}$ is the point-mobility of the plate at the control position $(x_c,y_c)$ which, according to the formulation presented in section 2.2, is given by:

$$Y_{11} = j\omega \sum_{m=1}^{\infty}\sum_{n=1}^{\infty} \frac{\phi_{m,n}(x_c, y_c)\phi_{m,n}(x_c, y_c)}{\Lambda[\omega_{m,n}^2(1+j\eta_s) - \omega^2]}. \tag{3.13}$$

$Y_{22}$ is the mobility of the seismic mass which can be derived from Newton's second law that gives

$$f_{c2} = m_a \ddot{w}_{c2} = j\omega m_a \dot{w}_{c2}, \tag{3.14}$$

so that:

$$Y_{22} = \frac{\dot{w}_{c2}}{f_{c2}} = j\omega m_a. \tag{3.15}$$

Equations (3.12) could be grouped in matrix form as follow:

$$\dot{\mathbf{w}} = \mathbf{Y}\mathbf{f} + \mathbf{Y}_{\mathrm{p}} f_p + \mathbf{Y}_{\mathrm{c}} u_c , \tag{3.16}$$

where:

$$\dot{\mathbf{w}} = \begin{Bmatrix} \dot{w}_{c1} \\ \dot{w}_{c2} \end{Bmatrix}, \tag{3.17}$$

$$\mathbf{Y} = \begin{bmatrix} Y_{11} & 0 \\ 0 & Y_{22} \end{bmatrix}, \tag{3.18}$$

$$\mathbf{f} = \begin{Bmatrix} f_{c1} \\ f_{c2} \end{Bmatrix}, \tag{3.19}$$

$$\mathbf{Y}_{\mathrm{p}} = \begin{bmatrix} Y_{cp} \\ 0 \end{bmatrix}, \tag{3.20}$$

$$\mathbf{Y}_{\mathrm{c}} = \begin{bmatrix} Y_{cc} \\ 0 \end{bmatrix}. \tag{3.21}$$

The response of the connecting elastic element of the accelerometer is derived in terms of impedances. The constitutive equations for the spring and damping elements in parallel could be written in two forms depending whether the actions of $f_{a1}$ or $f_{a2}$ are considered so that:

$$f_{a1} = k_a (w_{a2} - w_{a1}) = k_a \left( \frac{\dot{w}_{a2}}{j\omega} - \frac{\dot{w}_{a1}}{j\omega} \right), \tag{3.22}$$

$$f_{a2} = k_a (w_{a1} - w_{a2}) = k_a \left( \frac{\dot{w}_{a1}}{j\omega} - \frac{\dot{w}_{a2}}{j\omega} \right), \tag{3.23}$$

where in this case the relation $w(\omega) = \dot{w}(\omega)/j\omega$ was used, and

$$f_{a1} = c_a(\dot{w}_{a2} - \dot{w}_{a1}), \tag{3.24}$$

$$f_{a2} = c_a(\dot{w}_{a1} - \dot{w}_{a2}). \tag{3.25}$$

Remembering that the impedance of a system is given by the ratio between force and velocity, the four expressions given above can be grouped in two impedance equations as follows:

$$\begin{cases} f_{a1} = Z_{11}^a \dot{w}_{a1} + Z_{12}^a \dot{w}_{a2} \\ f_{a2} = Z_{21}^a \dot{w}_{a1} + Z_{22}^a \dot{w}_{a2} \end{cases}, \tag{3.26}$$

where:

$$Z_{11}^a = Z_{22}^a = \frac{k_a}{j\omega} + c_a, \tag{3.27}$$

$$Z_{12}^a = Z_{21}^a = -\frac{k_a}{j\omega} - c_a. \tag{3.28}$$

The two equations in (3.26) can be written in matrix form as follows:

$$\begin{Bmatrix} f_{a1} \\ f_{a2} \end{Bmatrix} = \begin{bmatrix} Z_{11}^a & Z_{12}^a \\ Z_{21}^a & Z_{22}^a \end{bmatrix} \begin{Bmatrix} \dot{w}_{a1} \\ \dot{w}_{a2} \end{Bmatrix}. \tag{3.29}$$

The conditions of compatibility and equilibrium at the connecting points 1 and 2, which are given respectively by:

$$\begin{cases} \dot{w}_{a1} = \dot{w}_{c1} \\ \dot{w}_{a2} = \dot{w}_{c2} \end{cases} \tag{3.30}$$

and

$$\begin{cases} f_{a1} + f_{c1} = 0 \\ f_{a2} + f_{c2} = 0 \end{cases} \Rightarrow \begin{cases} f_{c1} = -f_{a1} \\ f_{c2} = -f_{a2} \end{cases}, \tag{3.31}$$

are now considered so that equation (3.29) becomes:

$$\mathbf{f} = -\mathbf{Z}\dot{\mathbf{w}}, \tag{3.32}$$

where:

$$\mathbf{Z} = \begin{bmatrix} Z_{11}^{a} & Z_{12}^{a} \\ Z_{21}^{a} & Z_{22}^{a} \end{bmatrix}. \tag{3.33}$$

Substituting equation (3.32) in equation (3.16) and solving with respect to the velocity vector $\dot{\mathbf{w}}$ it is found:

$$\dot{\mathbf{w}} = (\mathbf{I} + \mathbf{YZ})^{-1}\{\mathbf{Y}_{\mathrm{p}} f_p + \mathbf{Y}_{\mathrm{c}} u_c\}. \tag{3.34}$$

As discussed in section 3.1, the signal output provided by the elastic piezoelectric element in the accelerometer is proportional to the relative displacement $z = w_{c2} - w_{c1}$ between the seismic mass and the base, i.e. $v_a = c_\sigma (w_{c2} - w_{c1})$. At frequencies below the fundamental resonance frequency of the accelerometer, this signal is proportional to the opposite of the acceleration at the base of the accelerometer, i.e. $v_a \cong -c_\sigma \frac{\ddot{w}_{c1}}{\omega_a^2}$. Thus in order to implement velocity feedback, the signal output from the accelerometer must be integrated with reference to time, i.e. for harmonic signals it should be multiplied by $\frac{1}{j\omega}$. As shown in Figure 19, the accelerometer sensor is therefore provided with an ideal integrator so that the output voltage $\hat{v}_a = \frac{c_\sigma}{j\omega}(w_{c2} - w_{c1})$ is now proportional to the opposite of the base velocity $\hat{v}_a \cong -c_\sigma \frac{\dot{w}_{c1}}{\omega_a^2}$. This signal is then feedback to the control actuator via a fixed positive control gain $g_c$. In this way the control force is a damping force since it is proportional to the opposite of the velocity

of the panel measured at the position where the force itself is applied, i.e. $f_c = g_c \hat{v}_a = g_c \frac{v_a}{j\omega} = g_c \frac{c_\sigma (w_{c2} - w_{c1})}{j\omega} \cong -g_c c_\sigma \frac{\dot{w}_{c1}}{\omega_a^2}$. Similarly the control moments generated along the edges of the piezoelectric strain actuator are proportional to the opposite of the velocity of the panel measured at the centre of the piezoelectric patch: $u_c = g_c \hat{v}_a = g_c \frac{v_a}{j\omega} = g_c \frac{c_\sigma (w_{c2} - w_{c1})}{j\omega} \cong -g_c c_\sigma \frac{\dot{w}_{c1}}{\omega_a^2}$. Thus also the piezoelectric patch actuator should generate a sort of damping excitation.

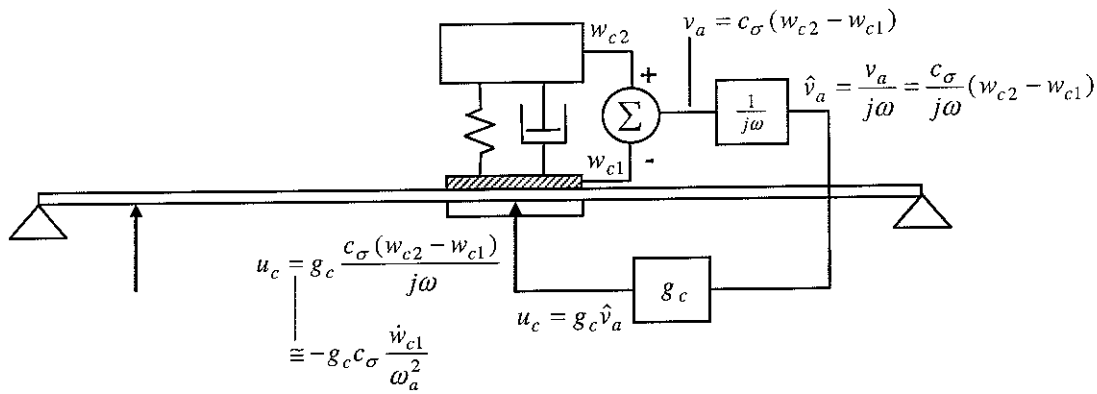


**Figure 19:** *scheme of the accelerometer mounted on an aluminium plate with either a collocated force actuator or closely located moment actuator piezoelectric patch actuator.*

The signal output from the accelerometer sensor and ideal integrator can be expressed in terms of the displacement vector $\mathbf{w} = \{w_{c1} \quad w_{c2}\}^T$ with the following matrix relation

$$\hat{v}_a = \frac{c_\sigma}{j\omega} \mathbf{d}_c \mathbf{w}, \tag{3.35}$$

where

$$\mathbf{d}_c = [-1 \quad 1] \tag{3.36}$$

and the displacement vector $\mathbf{w}$ can be derived by pre-multiplying equation (3.34) by $\frac{1}{j\omega}$ so that, assuming $f_p = 0$, the output signal from the sensor is given by

$$\hat{v}_a = \frac{c_\sigma}{j\omega}\mathbf{d}_c\left\{\frac{1}{j\omega}(\mathbf{I}+\mathbf{YZ})^{-1}\mathbf{Y}_c u_c\right\}. \tag{3.37}$$

In summary, the open loop sensor–actuator frequency response function of the velocity feedback control loops using either a force or piezoelectric patch actuator and the accelerometer, with integrator, sensor is given by

$$G(\omega) = \frac{\hat{v}_a}{u_c} = -\frac{c_\sigma}{\omega^2}\mathbf{d}_c(\mathbf{I}+\mathbf{YZ})^{-1}\mathbf{Y}_c, \tag{3.38}$$

where the mobility term $Y_{cc}$ in the vector $\mathbf{Y}_c$ is given by equation (2.7) with the modal excitation terms in equations (2.13) or (2.14) depending whether the control actuator is the point force or piezoelectric patch that generates lines of moments along the four edges.

As highlighted above, in this case the feedback gain is taken to be positive since the integrated signal from the accelerometer sensor is proportional to the opposite of the velocity at the base of the accelerometer and thus at the error position. Therefore in order to analyse the stability of such a positive feedback loop using the standard criteria for negative feedback loops the opposite of the sensor–actuator response function is considered in the plots below.

Following the analysis presented in section 2.3, the stability of the two control units with the accelerometer sensor and either the control force or control moments generated along the edges of the piezoelectric patch is assessed by plotting either the modulus and phase or the Nyquist plot of the open loop sensor–actuator frequency response function derived with equation (3.37). Figures 20 and 21 show the amplitude and phase of the sensor–actuator frequency response functions for the two control systems in the frequency range between 10 and 50 kHz. Comparing Figure 11 with Figure 20 and Figure 13 with Figure 21 it is clear that below few kHz the coupled response of the inertial accelerometer does not produce significant effects on the sensor–actuator frequency response function. In contrast it is evident that for frequencies near the fundamental resonance of the inertial accelerometer, $\omega \approx \sqrt{1-2\zeta_a^2}\,\omega_a$, the two sensor–actuator frequency response functions are characterised by a wide and high peak and a phase drop of -180° due indeed to the accelerometer resonance. This extra phase shift is very critical since for both control systems, beyond the fundamental resonance

frequency the phase exceeds -90° so that none of the two control systems could be considered unconditionally stable.

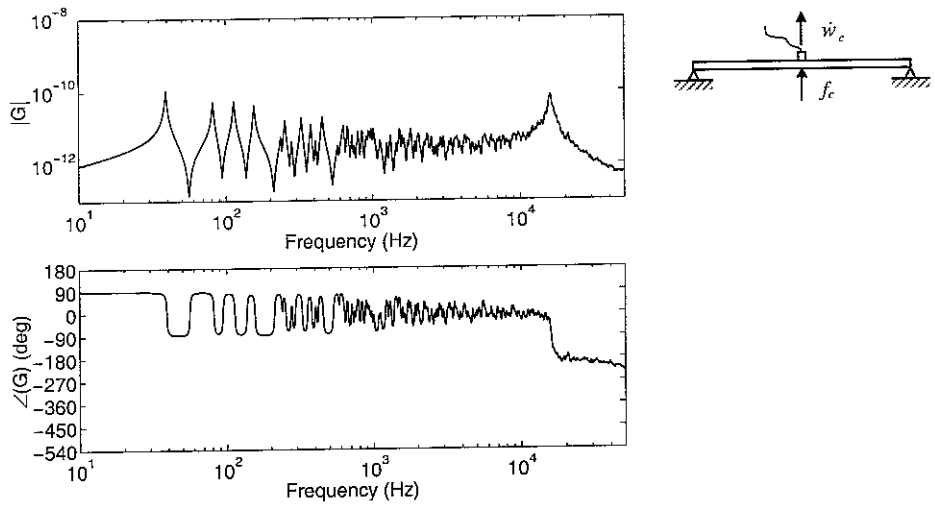


**Figure 20:** *frequency response amplitude (top plot) and phase (bottom plot) between an accelerometer sensor with integrator and a force actuator in the 10 Hz-50 KHz frequency range.*

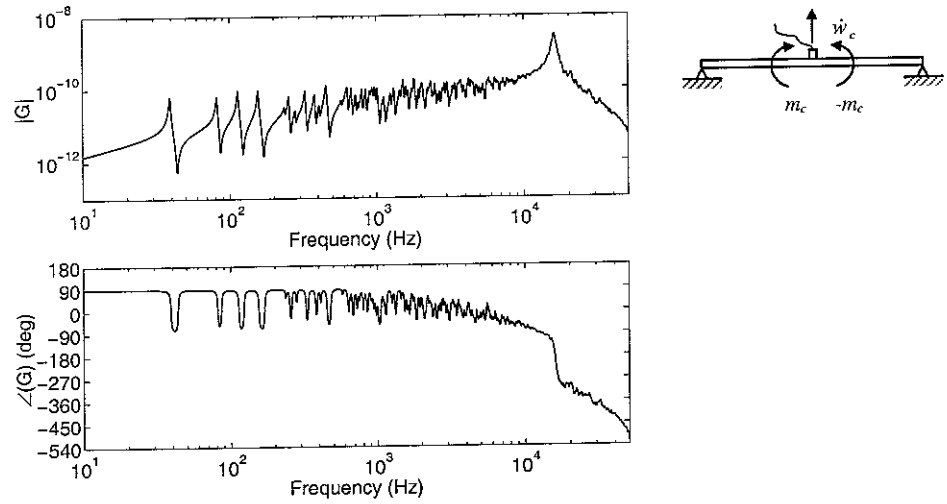


**Figure 21:** *frequency response amplitude (top plot) and phase (bottom plot) between an accelerometer sensor with integrator and a piezoelectric patch strain actuator without mass in the 10 Hz-50 KHz frequency range.*

Indeed, the Nyquist plots for the control units with the force or piezoelectric patch strain actuators, which are given respectively in Figures 22 and 23, show that the part of response function with frequencies around the resonance of the accelerometer occupies the left hand side of the Nyquist plot. Thus because of the extra -180° phase shift generated by the accelerometer resonance the higher frequency part of the two Nyquist plots encircles the real negative axis so that the control loop can not be considered unconditionally stable.

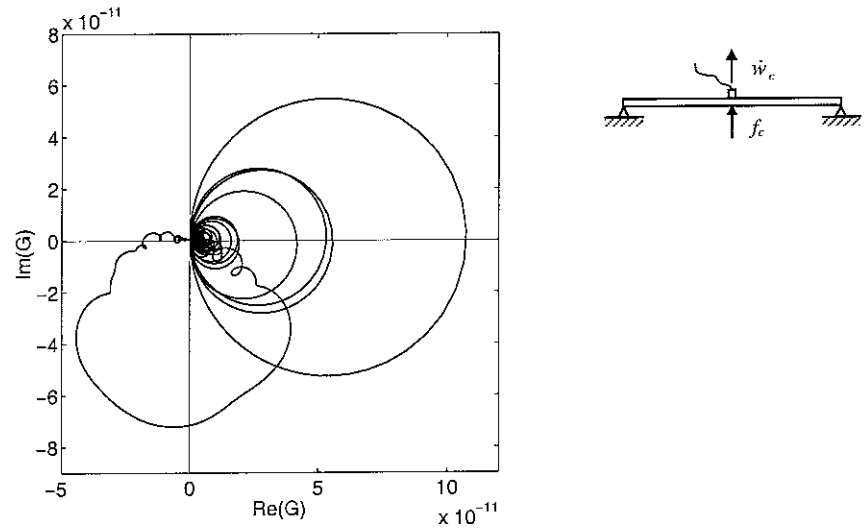


**Figure 22:** *Nyquist plot of the frequency response between an accelerometer sensor with integrator and a force actuator in the 10 Hz-50 KHz frequency range.*

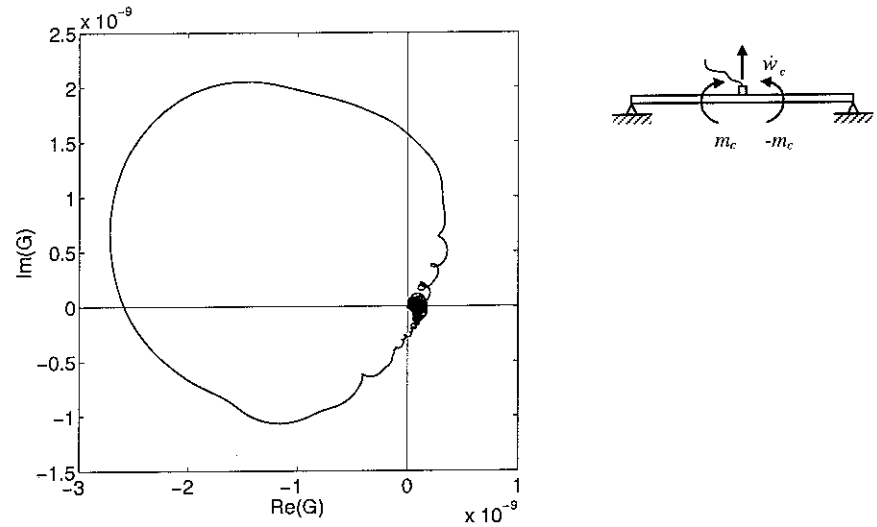


**Figure 23:** *Nyquist plot of the frequency response between an accelerometer sensor with integrator and a piezoelectric patch strain actuator without mass in the 10 Hz-50 KHz frequency range.*

Considering the case with the force actuator, Figure 22 shows that the amplitude of the loop in the left hand side of the Nyquist plot is about the same big as those on the right hand side since, as one can deduce from Figure 20, the amplitude of the frequency response function in proximity of the accelerometer fundamental resonance is about the same as the amplitudes of the response function relative to the low frequency resonances. However this loop is rotated with reference to the low frequency loops by just a bit more than $90^o$ so that it crosses the negative imaginary axis at a point that is just a fraction away from the origin than the points where the loops on the positive hand side cross the real positive axis. Thus the control system is conditionally stable and a limited range of control gains could be implemented so that some

active damping effects could be generated in correspondence to the low frequency resonances. Considering now the case with the piezoelectric patch strain actuator, Figure 23 shows that the amplitude of the loop in the left hand side of the Nyquist plot is much more big of those on the right hand side since, as one can deduce from Figure 21, the amplitude of the frequency response function in proximity of the accelerometer fundamental resonance is much more larger than the amplitudes of the response function relative to the low frequency resonances. As discussed in section 2.3, this is due to the intrinsic feature of piezoelectric strain actuators that more efficiently excite the panel at higher frequencies so that the amplitude of the sensor–actuator response function gradually rises with frequency. Moreover, in this case the big loop is rotated with reference to the low frequency loops by exactly $180^o$ so that it crosses the negative imaginary axis at a point that is much more far away from the origin than the points where the loops on the positive hand side cross the real positive axis. Thus the control system is univocally unstable for any control gain.

## 3.3 Sensor-actuator response function when the dynamics of the accelerometer and the mass effect of the piezoelectric patch actuator are taken in to account

The dynamics effects of the piezoelectric patch strain actuator were not taken into account in the study presented in the previous section. In this section the sensor–actuator response function is derived by taking into account only the mass effect of the piezoelectric patch actuator. This effect is modelled as a lumped mass of 4.1 g located at the control point. Thus the mathematical formulation to derive the vector with the velocities at the base and inertial mass of the accelerometer is the same of that used in section 3.2 with included the effect of a lumped mass, $m_{pzt}$, which is connected at the control point as shown in Figure 24.

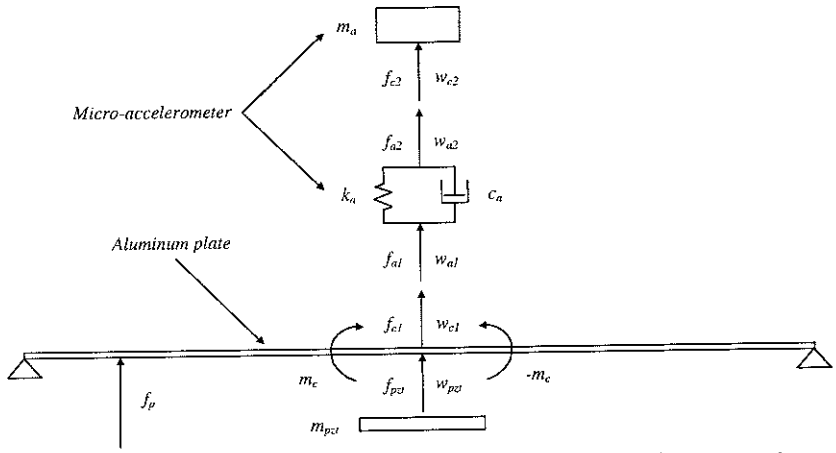


**Figure 24:** *scheme with the notation for the forces an displacements at the connecting points between the elements of the accelerometer which is mounted on an aluminium plate with a piezoelectric patch actuator that is modelled as a lumped mass with moment excitations at the edges.*

According to the notation shown in Figure 24, the compatibility and force equilibrium conditions at the control position are given by:

$$\begin{cases} \dot{w}_{a1} = \dot{w}_{c1} = \dot{w}_{pzt} \\ \dot{w}_{a2} = \dot{w}_{c2} \end{cases}, \tag{3.39}$$

$$\begin{cases} f_{a1} + f_{c1} + f_{pzt} = 0 \\ f_{a2} + f_{c2} = 0 \Rightarrow \end{cases} \Rightarrow \quad \begin{cases} f_{c1} = -f_{a1} - f_{pzt} \\ f_{c2} = -f_{a2} \end{cases}, \tag{3.40}$$

where $f_{pzt}$ is the force due to the inertial effect of the piezoelectric patch strain actuator. The response of the piezoelectric strain actuator lumped mass can be written in terms of an impedance relation as follows:

$$f_{pzt} = Z_{pzt} \dot{w}_{pzt}, \tag{3.41}$$

where, according to equation (3.15),

$$Z_{pzt} = \frac{1}{j\omega m_{pzt}}. \tag{3.42}$$

Thus, from the equilibrium and compatibility conditions in (3.39) and (3.40) and using the impedance matrix equation (3.29) for the spring damper elements in the accelerometer, the following relation can be derived:

$$\begin{Bmatrix} f_{c1} \\ f_{c2} \end{Bmatrix} = -\begin{bmatrix} Z_{11}^a & Z_{12}^a \\ Z_{21}^a & Z_{22}^a \end{bmatrix} \begin{Bmatrix} \dot{w}_{c1} \\ \dot{w}_{c2} \end{Bmatrix} - \begin{bmatrix} Z_{pzt} & 0 \\ 0 & 0 \end{bmatrix} \begin{Bmatrix} \dot{w}_{c1} \\ \dot{w}_{c2} \end{Bmatrix}, \tag{3.43}$$

which can be re-written in compact form as follows

$$\mathbf{f} = -\overline{\mathbf{Z}}\dot{\mathbf{w}}\,, \tag{3.44}$$

where

$$\overline{\mathbf{Z}} = \begin{bmatrix} Z_{11}^a + Z_{pzt} & Z_{12}^a \\ Z_{21}^a & Z_{22}^a \end{bmatrix}. \tag{3.45}$$

Equation (3.44) can therefore be used in the formulation derive in the previous section so that the open loop sensor–actuator frequency response function of the velocity feedback control loops using the accelerometer sensor with integrator and taking into account the mass effect of the piezoelectric patch actuator is given by

$$G(\omega) = \frac{\hat{v}_a}{u_c} = -\frac{c_\sigma}{\omega^2}\mathbf{d}_c\left(\mathbf{I} + \mathbf{Y}\overline{\mathbf{Z}}\right)^{-1}\mathbf{Y}_c\,. \tag{3.46}$$

Figure 25 shows the amplitude and phase of the sensor–actuator frequency response functions between 10 and 50 kHz. Comparing this Figure with Figures 21 it is found that, as one would expect, the mass effect of the piezoelectric patch actuator produces nearly no effect at low frequencies below few kHz. In contrast at higher frequencies it tends to pull down the amplitude of the frequency response function although the peak due to the resonance of the accelerometer is still higher than those due to the low frequency resonances of the plate.

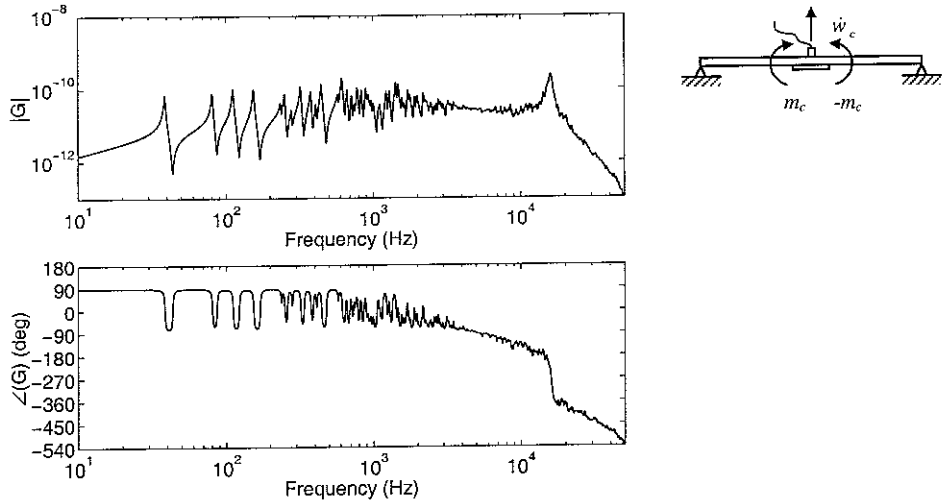


**Figure 25:** *frequency response amplitude (top plot) and phase (bottom plot) between an accelerometer sensor with integrator and a piezoelectric patch strain actuator modelled as a lumped mass $m_p$=4.1 g in the 10 Hz-50 KHz frequency range.*

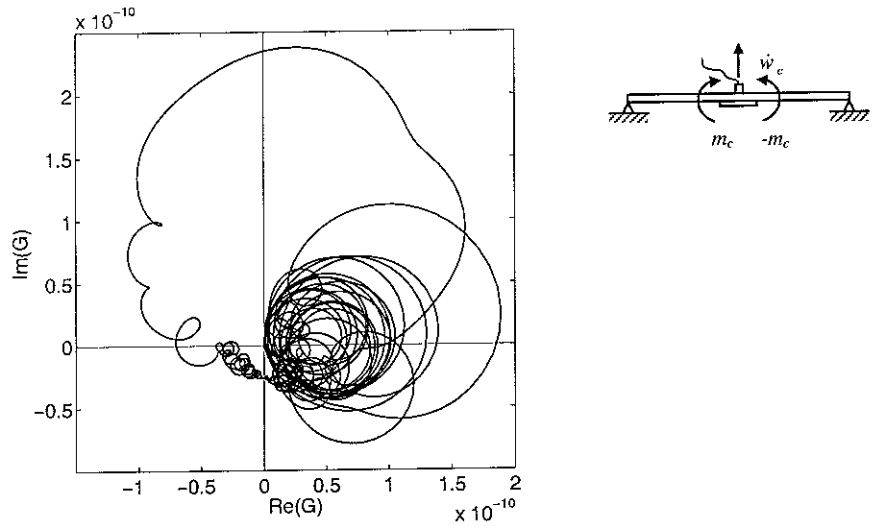


**Figure 26:** *Nyquist plot of the frequency response between an accelerometer sensor with integrator and a piezoelectric patch strain actuator modelled as a lumped mass $m_p$=4.1 g in the 10 Hz-50 KHz frequency range.*

Therefore the Nyquist plot for this sensor–actuator system, which is shown in Figure 26, is still characterised by a bigger loop on the left hand side than the loops on the right hand side. The phase lag introduced by the mass has incremented the rotation of this loop with reference to the low frequency loops to about $270^o$ However, although the piezoelectric actuator mass of 4.1 g tends to pull down the amplitude of the response function as the frequency rises and tends to generate an extra phase lag of $90^o$ yet these effects are not enough to produce respectively the necessary roll off and phase lag that would enable the implementation of a stable feedback control loop with a significant control gain.

### 3.4 Sensor–actuator response function when the dynamics of the accelerometer, the piezoelectric patch mass and the analogue time integration are taken in to account

The results presented in the two previous sections have been derived assuming that the accelerometer sensor shown in Figure 19 is equipped with an ideal integrator with frequency response function $G_{\text{int}}(\omega) = 1/j\omega$ . In practice, the analogue integration of the output signal from the accelerometer sensor $v_a$ is implemented with an R–C integrator circuit as shown in Figure 27 below [12]. The frequency response function for such a integrator circuit is given by

$$\overline{G}_{\text{int}}(\omega) = \frac{1}{1 + j\omega\tau}. \tag{3.47}$$

where

$$\tau = RC. \tag{3.48}$$

and $R$, $C$ are the resistance and capacitance in the integration circuit.

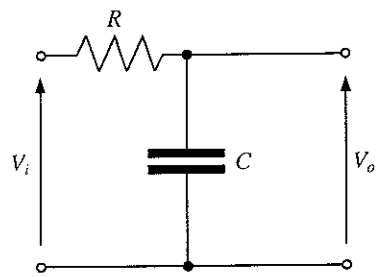


$$C(j\omega) = \frac{V_o(j\omega)}{V_i(j\omega)} = \frac{\frac{1}{j\omega C}}{R + \frac{1}{j\omega C}} = \frac{1}{1 + j\omega\tau}$$

$$\tau = RC$$

**Figure 27:** *R-C integrator circuit.*

As shown in Figure 28, this circuit produces the integration effect, which is characterised by a $\frac{1}{\omega}$ constant amplitude roll off and a $-90^o$ phase lag, at frequencies above the cut-off frequency

$$\omega_c = \frac{1}{\tau} = \frac{1}{RC}. \tag{3.49}$$

which in this case has been assumed to be at 20 Hz.

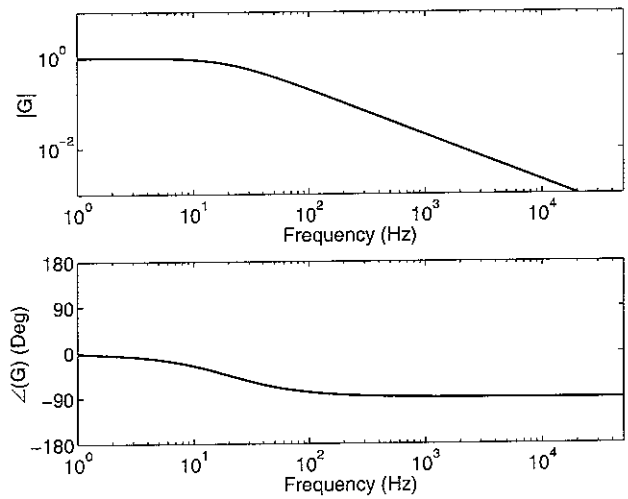


**Figure 28:** *frequency response amplitude (top plot) and phase (bottom plot) of the integrator circuit shown in Figure 27.*

Thus if, as shown in Figure 29, the frequency response function for the integrator circuit, $\overline{G}_{\text{int}}(\omega) = 1/(1+j\omega\tau)$, is included in the control scheme, then the sensor actuator frequency response function results

$$G(\omega) = \frac{\hat{v}_a}{u_c} = -\frac{c_\sigma}{1+j\omega\tau}\frac{1}{j\omega}\mathbf{d}_c(\mathbf{I}+\mathbf{Y}\overline{\mathbf{Z}})^{-1}\mathbf{Y}_c. \tag{3.50}$$

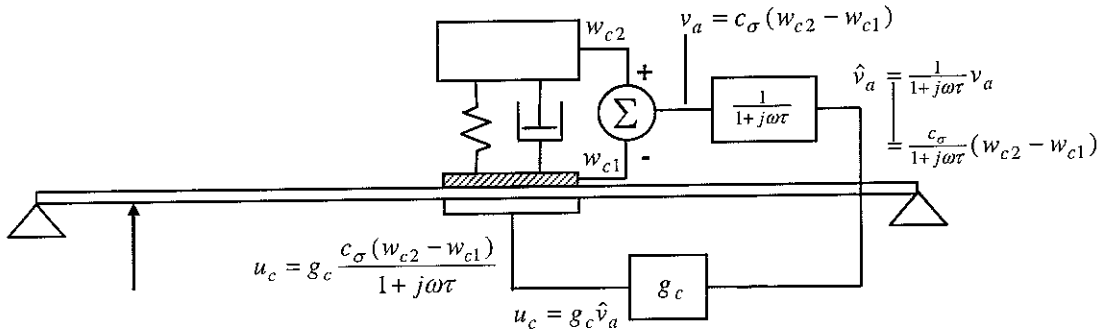


**Figure 29:** *scheme of the accelerometer with integrator circuit mounted on an aluminium plate with either a collocated force actuator or closely located moment actuator piezoelectric patch actuator.*

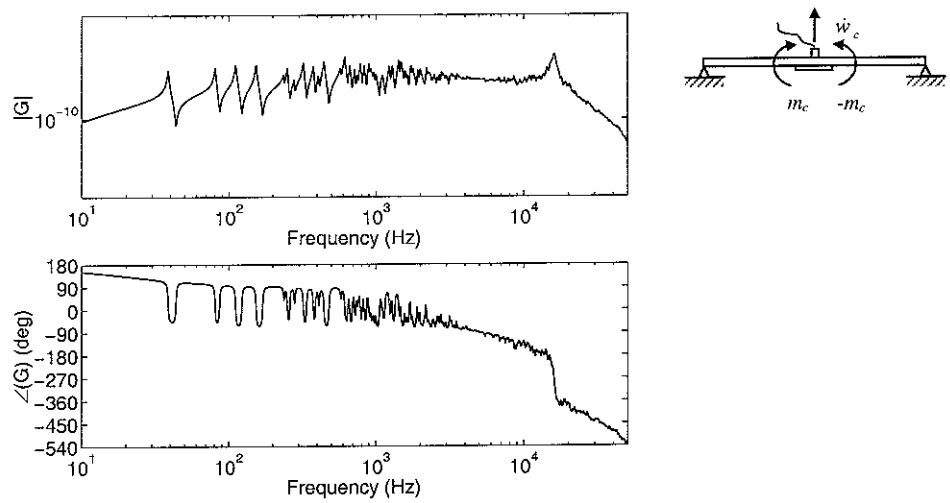


**Figure 30:** *frequency response amplitude (top plot) and phase (bottom plot) between an accelerometer sensor with the integrator circuit shown in Figure 27 and a piezoelectric patch strain actuator modelled as a lumped mass $m_p$=4.1 g in the 10 Hz-50 KHz frequency range.*

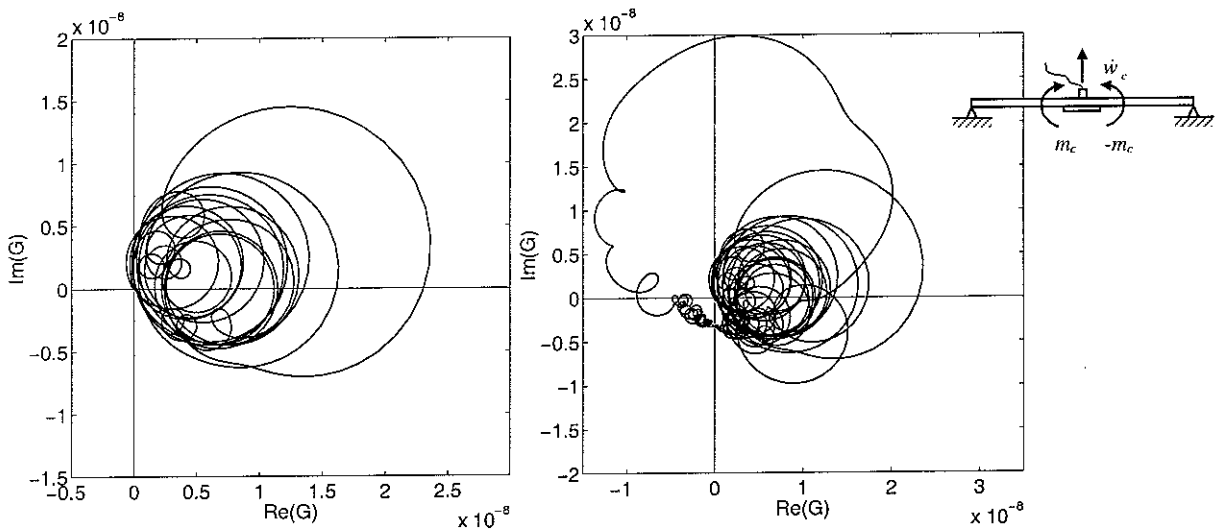


**Figure 31:** *Nyquist plot of the frequency response between an accelerometer sensor with the integrator circuit shown in Figure 27 and a piezoelectric patch strain actuator modelled as a lumped mass $m_p$=4.1 g in the 0 Hz-1 kHz range (left hand side plot) and 10 Hz-50 KHz frequency range (right hand side plot).*

Figure 30 shows the amplitude and phase of the sensor–actuator frequency response functions between 10 and 50 kHz when the integrator circuit in Figure 27 is used. Comparing this Figure with Figure 25 it comes out that, because below the cut off frequency there is no integration, then the sensor–actuator frequency response function below the cut off frequency is characterised by an amplitude slightly larger than that obtained with the ideal integration but more importantly the phase is about $90^o$ in advance so that below the cut of frequency the phase of the sensor–actuator frequency response function is between $+90^o$ and $+180^o$. This implies that, as shown in Figure 31, the Nyquist plot for this sensor–actuator frequency

response function starts on the left hand side top quadrant. In principle this should not cause instability problems although having part of the frequency response function on the left hand side of the Nyquist plot does not guarantee an unconditionally stable and robust feedback control loop.

### 3.5 Actuator mass and size effects

In order to understand and improve the performances of the feedback control unit, it is important to know its behaviour when some characteristic parameters change. Figure 32 shows the mass effect of the piezoelectric patch actuator considering four patches of the same 30×30 mm dimensions but with masses: $m_{p1}$=0, $m_{p2}$=2.5, $m_{p3}$=5, $m_{p4}$=10 g. As highlighted in the previous section, the mass tends to roll off the amplitude response at higher frequencies. Indeed, Figure 32 shows that as the mass of the actuator is increased as the amplitude of the response function tends to go down at higher frequencies. However even with a 10 g piezoelectric actuator the sensor–actuator response function is still characterised by amplitudes at higher frequency which are comparable to the lower frequencies peaks due to the resonances of the plate. Thus, as shown by the Nyquist plots in Figure 33, there are still large loops in left hand side of the plots which indicates that the feedback control loop are either unstable for all control gains (top two plots) or conditionally stable for a relatively small set of control gains (bottom two plots).

A second important parametric analysis takes into account the variation of the size of the piezoelectric patch actuator while its mass is kept constant to 4.1 g. Four cases have been considered with square patches whose dimensions are 5, 10, 30 and 50 mm. Figure 34 shows that the greater is the dimension of the actuator the greater is amplitude rise effect with frequency. Moreover, as the size of the actuator rises as the cut off frequency for which the phase exceeds -90° falls down. Thus, the smaller is the size of the actuator the wider is the frequency band where the phase remains between +90° and -90°. The Nyquist plots shown in Figure 35 indicate that even for the smallest patch there is always a relatively large loop on the left hand side of the plot.

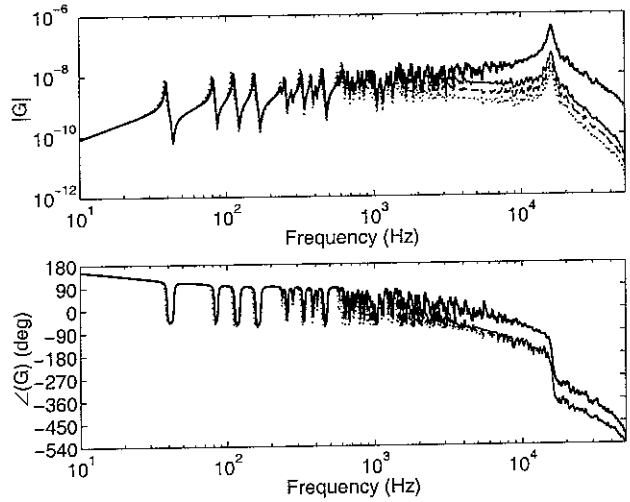


**Figure 32:** *frequency response amplitude (top plot) and phase (bottom plot) between a micro-accelerometer and a piezoelectric patch strain actuator of different masses but same dimensions in the 10 Hz-50 KHz frequency range. The thick solid line represents a piezoelectric patch strain actuator of mass 0 g, the thin solid line is referred to a mass of 2.5 g, the dashed line is referred to a mass of 5 g and the dotted line is referred to a mass of 10 g.*

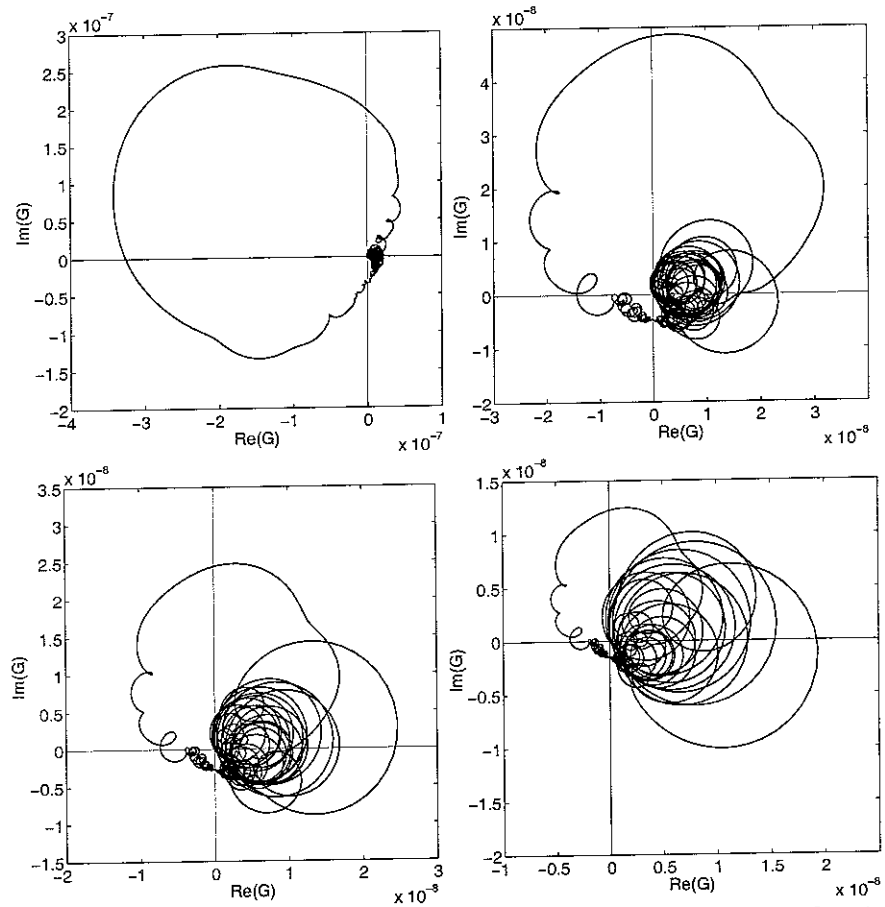


**Figure 33:** *Nyquist plots of the frequency response between a micro-accelerometer and a piezoelectric patch strain actuator of different masses in the 10 Hz-50 KHz frequency range. From left to right it is shown the results for a piezoelectric patch strain actuator of mass 0 g, 2.5 g, 5 g and 10 g.*

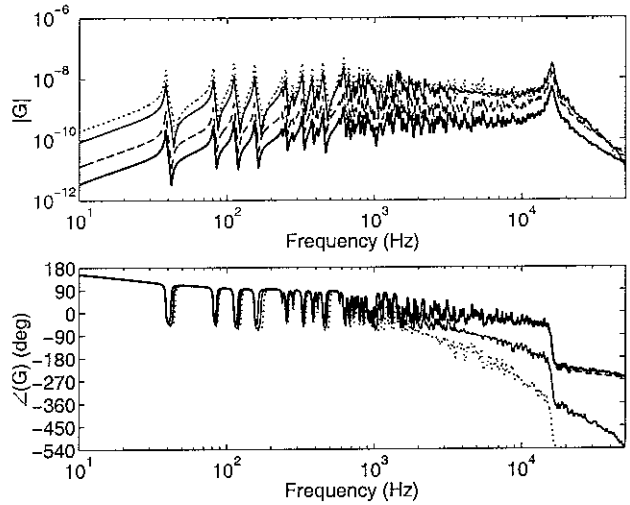


**Figure 34:** *frequency response amplitude (top plot) and phase (bottom plot) between a micro-accelerometer and a piezoelectric square patch strain actuator of different dimensions but same masses in the 10 Hz-50 KHz frequency range. The thick solid line represents a piezoelectric square patch strain actuator of side 5 mm, the dashed line is referred to a side of 10 mm, the thin solid line is referred to a mass of 30 mm and the dotted line is referred to a mass of 50 mm.*

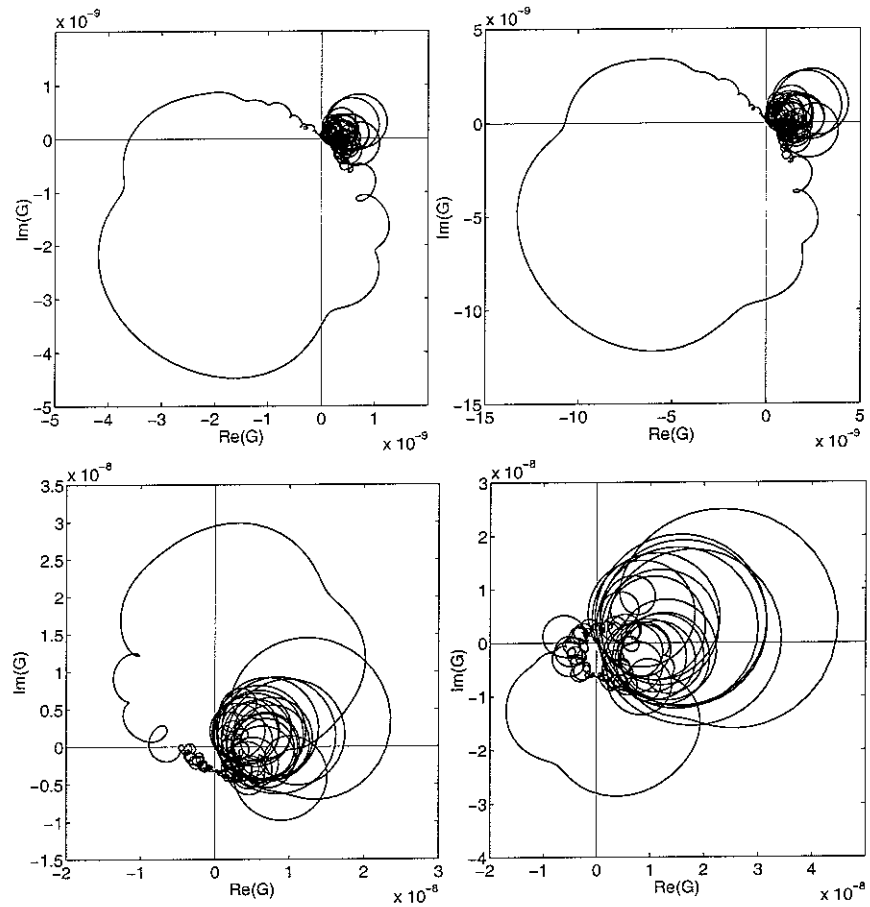


**Figure 35:** *Nyquist plots of the frequency response between a micro-accelerometer and a piezoelectric square patch strain actuator of different sides but the same mass in the 10 Hz-50 KHz frequency range. From left to right it is shown the results for a piezoelectric square patch strain actuator of side 5 mm, 10 mm, 30 mm and 50 mm.*

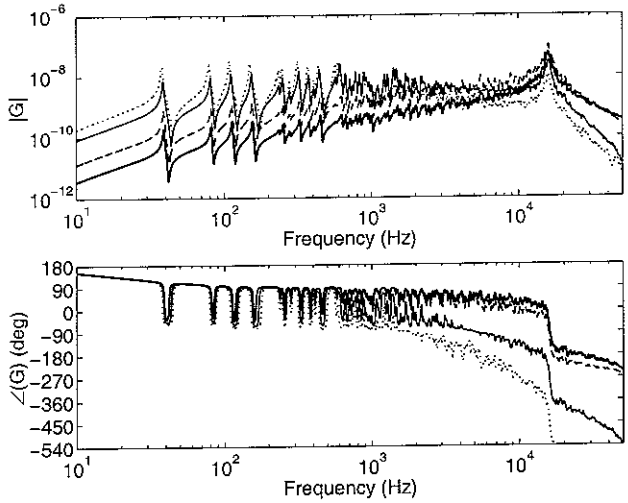


**Figure 36:** *frequency response amplitude (top plot) and phase (bottom plot) between a micro-accelerometer and a piezoelectric square patch strain actuator of different dimensions and then different masses in the 10 Hz-50 KHz frequency range. The thick solid line represents a piezoelectric square patch strain actuator of side 5 mm and mass of 0.11 g, the dashed line is referred to a side of 10 mm and mass of 0.46 g, the thin solid line is referred to a mass of 30 mm and mass of 4.1 g and the dotted line is referred to a side of 50 mm and mass of 11.5 g.*

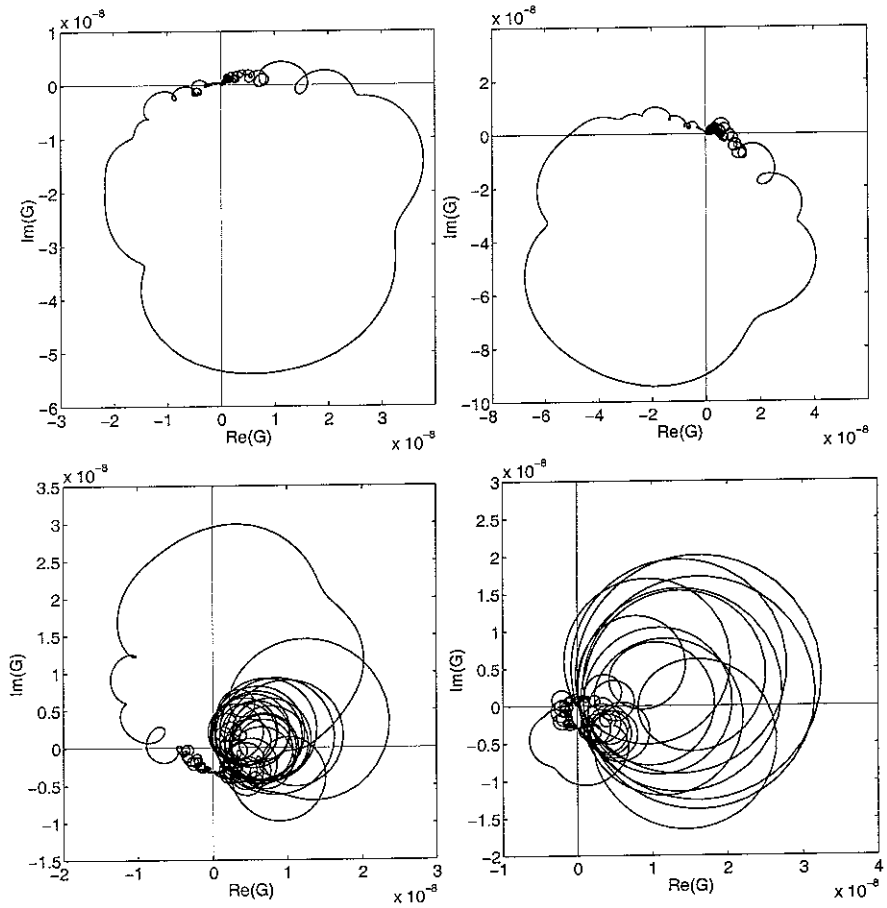


**Figure 38:** *Nyquist plots of the frequency response between a micro-accelerometer and a piezoelectric square patch strain actuator of different sides and then different mass in the 10 Hz-50 KHz frequency range. From left to right it is shown the results for a piezoelectric square patch strain actuator of side 5 mm, 10 mm, 30 mm, and 50 mm and correspondent mass 0.11 g, 0.46 g, 4.1 g and 11.5 g.*

If the same type of piezoelectric material is considered then the weight of the transducer can be changed by changing the dimensions. Figures 36 and 37 show the modulus and phase and the Nyquist plot of the sensor–actuator frequency response function when the density of the piezoelectric patches is $7650\,\mathrm{kg/m^3}$ and dimensions 5, 10, 30 and 50 mm so that their masses are 0.11 g, 0.46 g, 4.1 g and 11.5 g respectively. The results shown in these two figures indicate that the mass effect tends to dominate over the size effect. In fact, in this case, as the size, and therefore the mass, of the piezoelectric patch actuator is increased, as the amplitude of the sensor–actuator frequency response function at higher frequencies is reduced.

In conclusion this parametric study on the size and mass of the piezoelectric actuator highlights that the sensor–actuator control unit could be made more stable by using a relatively heavy and small piezoelectric patch actuator so that the efficient higher frequency excitation of the panel by the piezoelectric patch is brought down. However it is the resonance effect of the accelerometer which produces the higher frequency peak and the 180° phase lag that still causes instability conditions. This resonance effect could also be reduced by increasing the mass of the piezoelectric patch but the parametric study shown in figure 32 indicates that relatively large and thus impractical mass should be used. It is therefore necessary to investigate how the higher frequency amplitude of the open loop sensor–actuator frequency response function could be brought further down by choosing an accelerometer sensor with an appropriate natural frequency and eventually a larger damping effect.

### 3.6 Sensor natural frequency and damping effects

As mentioned in the previous sections the fundamental resonance of the accelerometer sensor is an important cause of instability in the feedback loop with a closely located piezoelectric patch actuator since it introduces a 180° extra phase shift and a significant increase of the amplitude in the sensor–actuator frequency response function so that the Nyquist plot of the open loop the sensor–actuator frequency response function is characterised by left hand side loop which is as large as or even larger than the loops on the right hand side. Thus even with small control gains the control system goes unstable.

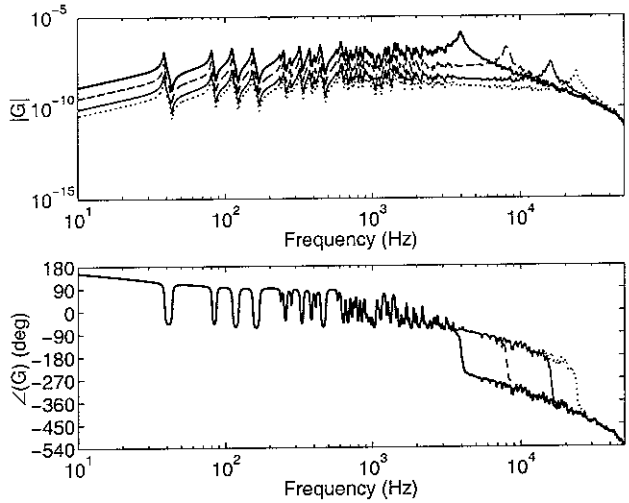


**Figure 39:** *frequency response amplitude (top plot) and phase (bottom plot) between a micro-accelerometer of different natural frequencies and a piezoelectric patch strain actuator in the 10 Hz-50 KHz frequency range. The thick solid line represents a accelerometer of natural frequency 3.97 KHz, the dashed line is referred to natural frequency 8.06 KHz, the thin solid line is referred to natural frequency 15.9 KHz and the dotted line is referred to natural frequency 23.8 KHz.*

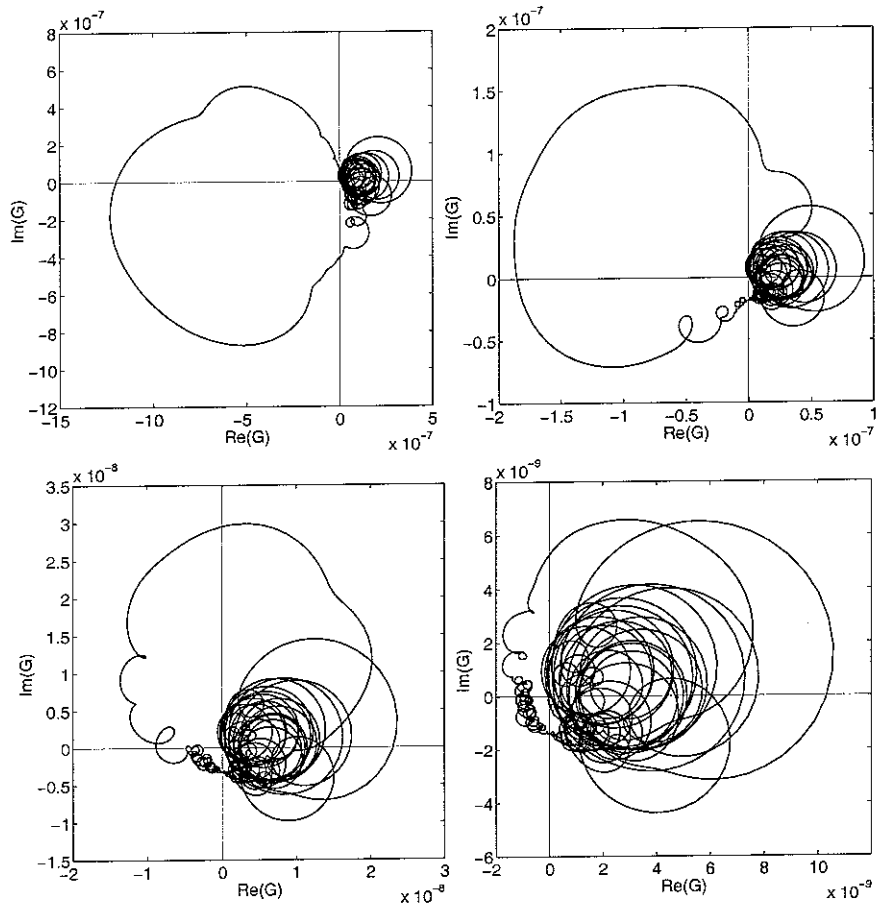


**Figure 40:** *Nyquist plots of the frequency response between a micro-accelerometer of different natural frequencies and a piezoelectric patch strain actuator in the 10 Hz-50 KHz frequency range. From left to right it is shown the results for a micro-accelerometer of natural frequency 3.97 kHz, 8.06 kHz (the reference value), 15.9 kHz and 23.8 kHz.*

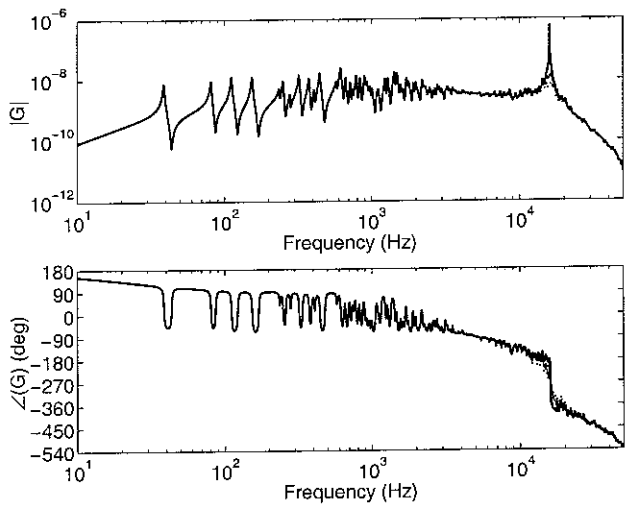


**Figure 41:** *frequency response amplitude (top plot) and phase (bottom plot) between micro-accelerometers of different damping coefficient and a piezoelectric patch strain actuator in the 10 Hz-50 KHz frequency range. The thick solid line represents an accelerometer with a damping ratio of 0.001%, the dashed line is referred to a damping ratio of 0.01% , the thin solid line is referred to a damping ratio of 0.05% and the dotted line is referred to a damping ratio of 0.1%.*

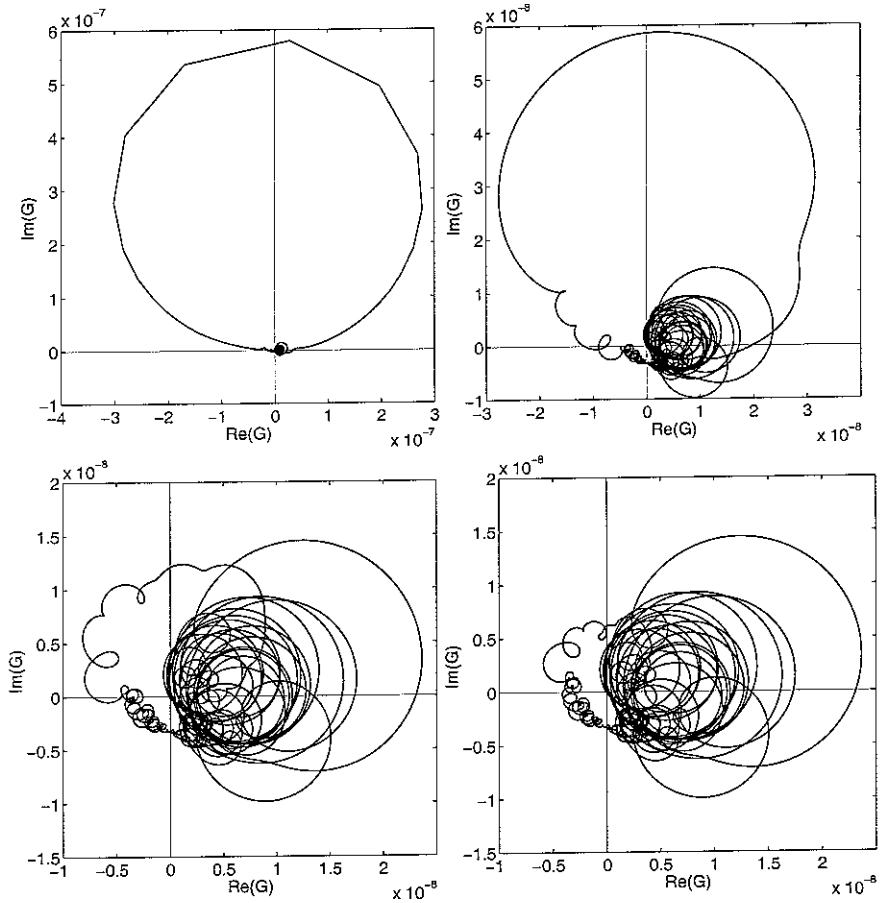


**Figure 42:** *Nyquist plots of the frequency response between micro-accelerometers with different damping coefficient and a piezoelectric patch strain actuator in the 10 Hz-50 KHz frequency range. From left to right it is shown the results for a micro-accelerometer with damping ratio of 0.001%, 0.01%, 0.05 and 0.1%.*

Although changing the size and mass of the piezoelectric actuator brings in some benefits, it is necessary to act on the resonance of the accelerometer sensor. There are two parameters that could be changed: first the natural frequency of the accelerometer and second the passive damping acting on the inertial mass of the accelerometer.

Figure 39 shows the sensor–actuator frequency response function when the accelerometer sensor has natural frequencies $f_{a1}$=3.97 kHz, $f_{a2}$=8.06 kHz, $f_{a3}$=15.9 kHz, and $f_{a4}$=23.8 kHz and the 30×30 mm piezoelectric patch actuator of 4.1 g is used. The top plot in Figure 39 shows that as the natural frequency of the accelerometer is reduce as the intrinsic rising effect of the amplitude with frequency due to the moment excitation generated by the piezoelectric patch actuator is cut down at lower frequency[1]. This is because beyond the resonance frequency the accelerometer output naturally rolls off. Also, as one would expect, the phase shift of 180° is moved down in frequency. The Nyquist plots for the four systems, which are shown in Figure 40, indicate that with relatively low natural frequencies the left hand side loop is relatively large and makes the system unstable. In contrast with higher natural frequencies the left hand side loop is not so critical and this is because at higher frequencies the inertial effect of the piezoelectric patch actuator is larger and thus produces a larger roll of effect. But more importantly, at higher frequencies the inertial effect of the mass produces a larger phase lag so that the large loop due to the accelerometer resonance is turned by 270° (bottom left plot in Figure 40) or even 360° (bottom right plot in Figure 40) so that the left hand side is relatively small compared to the right hand of the Nyquist plot. In conclusion the four plots in Figure 40 indicates that it is preferable to use accelerometer sensor with higher natural frequencies rather than, as one would intuitively do, with relatively low natural frequencies.

The final parametric study is concerned on the damping effect in the accelerometer sensor. The sensor–actuator frequency response function considering the accelerometer sensor with the following damping rations is therefore studied: $\zeta_{a1} = 0.001\%$, $\zeta_{a2} = 0.01\%$, $\zeta_{a3} = 0.05\%$ and $\zeta_{a4} = 0.1\%$. Figure 41 shows that with relatively large damping values the accelerometer resonance is cut down and then, as shown in the bottom Nyquist plots of Figure

[1] Note that as the resonance frequency is increased as the sensor–actuator frequency response function is shifted down since, as discussed in section 3.1, the sensitivity of the accelerometer sensor is inversely proportional to the square of the natural frequency.

42 the loop on the left hand side is comparatively smaller than those on the right hand side so that a feedback loop could be implemented with a limited range of control gains.

# 4. DVFB USING AN ACCELEROMETER SENSOR WITH EMBEDDED A VELOCITY FEEDBACK CONTROL LOOP

The study presented in Chapter 3 has shown that there are a number of problems in using an accelerometer sensor in order to implement direct velocity feedback. First, the signal output must be integrated in order to be proportional to the velocity at the errors sensor position. This has to be done in real time via a classic integration analogue circuit [12] which produces the wanted integration only above a cut off frequency so that at low frequencies there could be instability conditions. Second, the output signal is proportional to acceleration only below the fundamental resonance frequency of the accelerometer. Thus in order to implement control up to a relatively high frequency the resonance frequency must be well above this limit. As a result an accelerometer with a relatively high resonance frequency must be used so that the magnitude of the signal output, which is proportional to the inverse of the square natural frequency, will be relatively small. Third, at the fundamental resonance frequency there is a phase lag of $180^{o}$ that also would destabilise the control system.

In this section a new type of sensor is considered which is made with a spring–mass seismic principal sensor with embedded an active damper system that produces two important effects: first it damps down the response of this system at its fundamental resonance frequency without degrading the amplitude roll off at higher frequencies and second, provided the control gain of the active damper embedded in the sensor is properly tuned, below the fundamental resonance frequency, it provides a signal output proportional to the opposite of the velocity at the base of the sensor itself. Thus this type of sensor, which will be referred as the "velocity sensor" in the remaining part of the report, should provide the ideal output signal for a direct velocity feedback control system where, at frequencies below its fundamental resonance, the output signal is directly proportional to the velocity at the base of the sensor itself and then it rolls off at higher frequencies.

## 4.1 Velocity sensor response function when the velocity feedback control loop is implemented using an ideal velocity control sensor

Figure 43 shows the scheme of the new velocity sensor which is formed by two sensors: the

principal sensor with attached a control sensor. The principal sensor is made with a seismic mass $m_a$ connected to a vibrating base via a piezoelectric elastic element of stiffness $k_a$ and a dashpot with a damping coefficient $c_a$. As with the ordinary accelerometer sensors, the output signal is given by the elastic element which, as given in equation (3.1) generates a signal output directly proportional to the relative displacement between the inertial mass and the vibrating base, that is $v_a = c_\sigma (w_{c2} - w_{c1})$. A feedback control system is embedded on the principal sensor which consists of a velocity control sensor on the inertial mass, $m_a$, and a reactive control force between the inertial mass, $m_a$, and the vibrating base, thus in parallel with the piezoelectric elastic element. The output signal from the velocity control sensor is feedback to the actuator via a negative control gain so that the control force, $f_s$, is directly proportional to the opposite of the velocity of the mass and thus, as shown in section 2.1, sky hook damping is generated on the system [7].

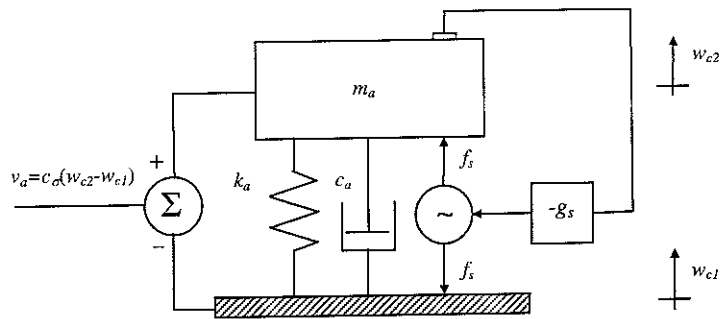


**Figure 43:** *schematic representation of the velocity sensor formed by a principal sensor which is made of a spring mass system with embedded a velocity feedback control loop.*

Following the formulation presented in section 3.1 and assuming the control sensor fixed on the inertial mass, $m_a$, to be an ideal velocity sensor, the equation of motion for such a system can be derived from Newton's second law which gives:

$$m_a \ddot{w}_{c2} = -c_a (\dot{w}_{c2} - \dot{w}_{c1}) - k_a (w_{c2} - w_{c1}) + f_s, \tag{4.1}$$

where $w_{c1}$ and $w_{c2}$ are the displacements of the base and suspended mass respectively and $f_s$ is the feedback control force of the control loop in the velocity sensor. Defining

$$z = w_{c2} - w_{c1}, \tag{4.2}$$

equation 4.1 gives:

$$m_a\ddot{z} + c_a\dot{z} + k_a z = f_s - m_a\ddot{w}_{c1}, \tag{4.3}$$

where $z$ represents the relative displacement between the seismic mass and the vibrating base. In order to implement negative velocity feedback the output signal from the velocity control sensor is feedback to the control force actuator via a fixed negative feedback gain so that:

$$f_s = -g_s\dot{w}_{c2} \tag{4.4}$$

and equation (4.3) becomes

$$m_a\ddot{z} + c_a\dot{z} + k_a z = -g_s\dot{w}_{c2} - m_a\ddot{w}_{c1}, \tag{4.5}$$

which, using the expression for the relative displacement in (4.2), could be reworked as follows:

$$m_a\ddot{z} + c_a\dot{z} + k_a z = -g_s\dot{z} - g_s\dot{w}_{c1} - m_a\ddot{w}_{c1}. \tag{4.6}$$

Considering harmonic motion such that, the displacements of the vibrating base and seismic mass and the relative displacement between the seismic mass and the vibrating base are given respectively by equations (3.5a,b) and (3.6), then equation (4.6) can be formulated in terms of the phasors $w_{c1}(\omega)$, $w_{c2}(\omega)$ and $z(\omega)$, so that:

$$\left\{-\omega^2 m_a + j\omega(c_a + g_s) + k_a\right\} z e^{j\omega t} = (\omega^2 m_a - j\omega g_s) w_{c1} e^{j\omega t}. \tag{4.7}$$

Thus the ratio between the phasors of the relative displacement $z = w_{c2} - w_{c1}$ and velocity $\dot{w}_{c1}$ of the base is:

$$\frac{z}{j\omega w_{c1}} = \frac{z}{\dot{w}_{c1}} = -\frac{g_s + j\omega m_a}{(k_a - \omega^2 m_a) + j\omega(c_a + g_s)} = -\frac{\frac{g_s}{k_a} + j\frac{\omega}{\omega_a^2}}{\left(1 - \frac{\omega^2}{\omega_a^2}\right) + j2\zeta_a \frac{\omega}{\omega_a}\left(1 + \frac{g_s}{c_a}\right)}, \quad (4.8)$$

which, following the formulation presented in section 3.1, can be rewritten in compact form as follows:

$$\frac{z}{\dot{w}_{c1}} = -\left\{\frac{g_s}{k_a} + j\frac{\omega}{\omega_a^2}\right\}\left|H_v\left(\frac{\omega}{\omega_a}\right)\right|e^{-j\phi_v}, \quad (4.9)$$

where

$$H_v\left(\frac{\omega}{\omega_a}\right) = \frac{1}{\left(1 - \frac{\omega^2}{\omega_a^2}\right) + j2\zeta_a\left(1 + \frac{g_s}{c_a}\right)\frac{\omega}{\omega_a}} = \frac{1}{\left(1 - \frac{\omega^2}{\omega_a^2}\right) + j2\bar{\zeta}_a \frac{\omega}{\omega_a}}, \quad (4.10)$$

so that

$$\left|H_v\left(\frac{\omega}{\omega_a}\right)\right| = \frac{1}{\left[\left(1 - \frac{\omega^2}{\omega_a^2}\right)^2 + \left(2\bar{\zeta}_a \frac{\omega}{\omega_a}\right)^2\right]^{\frac{1}{2}}}, \qquad \tan\phi_v = \frac{2\bar{\zeta}_a \frac{\omega}{\omega_a}}{1 - \frac{\omega^2}{\omega_a^2}}. \quad (4.11a,b)$$

The function $H_v\left(\frac{\omega}{\omega_a}\right)$ is a typical complex frequency response function of a single degree of freedom system where the damping effect is given by an "active damping ratio"

$$\bar{\zeta}_a = \zeta_a\left(1 + \frac{g_s}{c_a}\right), \quad (4.12)$$

which indicates that for control gains

$$g_s \geq c_a\left(\frac{1}{\zeta_a}-1\right), \tag{4.13}$$

the sensor is either critically or over damped. Considering frequencies below the natural frequency such that

$$\omega = \Omega\omega_a, \tag{4.14}$$

then equation (4.8) becomes

$$\frac{z}{\dot{w}_{c1}} = -\frac{\frac{g_s}{k_a}+j\frac{\Omega}{\omega_a}}{\left(1-\Omega^2\right)+j2\zeta_a\Omega\left(1+\frac{g_s}{c_a}\right)}. \tag{4.15}$$

Multiplying the numerator and denominator by the conjugate of the denominator this equation becomes

$$\frac{z}{\dot{w}_{c1}} = H_g(\Omega, g_s) = -\frac{\left(\frac{g_s}{k_a}+j\frac{\Omega}{\omega_a}\right)\left[\left(1-\Omega^2\right)-j2\zeta_a\Omega\left(1+\frac{g_s}{c_a}\right)\right]}{\left(1-\Omega^2\right)^2+\left[2\zeta_a\Omega\left(1+\frac{g_s}{c_a}\right)\right]^2}, \tag{4.16}$$

which can be reworked in terms of a real and imaginary parts

$$\frac{z}{\dot{w}_{c1}} = -\frac{\frac{g_s}{k_a}\left(1-\Omega^2\right)+\frac{2\zeta_a\Omega^2}{\omega_a}\left(1+\frac{g_s}{c_a}\right)}{\left(1-\Omega^2\right)^2+\left[2\zeta_a\Omega\left(1+\frac{g_s}{c_a}\right)\right]^2} - j\frac{\frac{\Omega}{\omega_a}\left(1-\Omega^2\right)-\frac{2\zeta_a\Omega g_s}{k_a}\left(1+\frac{g_s}{c_a}\right)}{\left(1-\Omega^2\right)^2+\left[2\zeta_a\Omega\left(1+\frac{g_s}{c_a}\right)\right]^2}. \tag{4.17}$$

Thus, the relative displacement between the suspended mass and vibrating base, $z = w_{c2} - w_{c1}$, and therefore the sensor output signal, $v_a = c_\sigma (w_{c2} - w_{c1})$, could be directly proportional to the velocity of the base, $\dot{w}_{c1}$, if the imaginary part of equation (4.17) is zero, that is

$$\frac{\Omega}{\omega_a}\left(1-\Omega^2\right)-\frac{2\zeta_a \Omega g_s}{k_a}\left(1+\frac{g_s}{c_a}\right)=0. \tag{4.18}$$

This equation has two roots

$$\hat{g}_{s1,2}(\Omega)=-\frac{-\frac{2\zeta_a\Omega}{k_a}\pm\sqrt{\left(\frac{2\zeta_a\Omega}{k_a}\right)^2-4\frac{\Omega}{\omega_a}\left(1-\Omega^2\right)\frac{2\zeta_a\Omega}{c_a k_a}}}{2\frac{\Omega}{\omega_a}\left(1-\Omega^2\right)}. \tag{4.19}$$

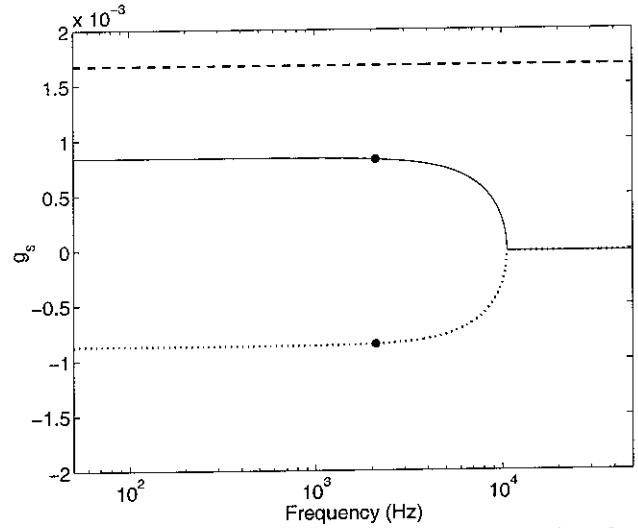


**Figure 44:** *control gains of the velocity feedback control loop embedded in the velocity sensor that would produce an output signal from the principal sensor directly proportional to the base velocity (solid and dotted lines) or would produce the maximum damping effect of the fundamental resonance frequency of the principal sensor (dashed line).*

The solid and dashed lines in Figure 44 give the two control gains, $\hat{g}_{s1,2}(\Omega)$, that would produce exactly an output signal directly proportional to the velocity of the base. However only the feedback gains of the solid line could be implemented in practice since those given by the dotted line would produce a positive velocity feedback loop which is intrinsically

unstable. Thus, provided the control gain functions, $\hat{g}_{s1,2}$, in equation (4.19) are implemented, then the relative displacement between the inertial mass and the base of the sensor is given by the following function

$$\frac{z}{\dot{w}_{c1}} = \hat{H}_{g1,2}(\Omega) = -\frac{\frac{\hat{g}_{s1,2}}{k_a}\left(1-\Omega^2\right)+\frac{2\zeta_a\Omega^2}{\omega_a}\left(1+\frac{\hat{g}_{s1,2}}{c_a}\right)}{\left(1-\Omega^2\right)^2+\left[2\zeta_a\Omega\left(1+\frac{\hat{g}_{s1,2}}{c_a}\right)\right]^2}, \tag{4.20}$$

which is real and frequency dependent. Figure 45 shows the amplitude and phase of the ratio between the relative displacement of the mass, $m_a$, and the vibrating base of the principal sensor when there is no feedback control gain (thick solid line) or a negative velocity feedback loop is implemented with the optimal control gain given by the solid line in Figure 44 (faint solid line) and, for completeness, with the optimal control gain given by the dotted line in Figure 44 (dotted line).

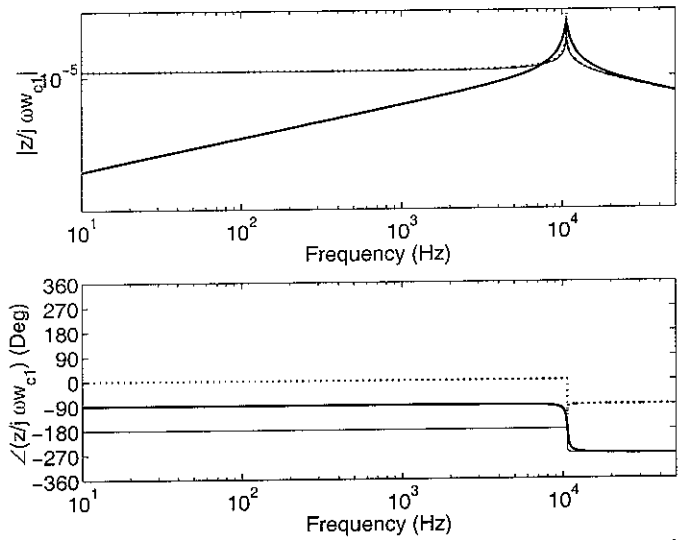


**Figure 45:** *amplitude (top plot) and phase (bottom plot) of the ratio between the relative displacement of the mass, $m_a$, and vibrating base and the velocity of the base of the sensor with embedded a feedback loop using an ideal velocity sensor when there is no feedback control gain (thick solid line) or a velocity feedback loop is implemented with the control gains of the solid line in Figure 44 (faint solid line) or the control gains of the dotted line in Figure 44 (dotted line).*

This plot confirms that in the ideal case where the control gain functions given by equation (4.19) are implemented then the relative displacement between the inertial mass, $m_a$, and the base of the principal sensor, and thus the velocity sensor output signal, is directly proportional

to the velocity at the base of the velocity sensor itself. In particular, when the control gain function described by the solid line in Figure 44 is implemented, then the relative displacement between the inertial mass, $m_a$, and the vibrating base is proportional to the opposite of the velocity at the vibrating base of the principal sensor and thus of the velocity sensor. However it is important to note that the optimal control gain tends to zero in proximity to the resonance frequency of the principal sensor so that the relative displacement between the inertial mass and the vibrating base, and thus the velocity sensor output signal, remains characterised by a lightly damped resonance peak. This is a negative effect since, as highlighted in Chapter 3, this peak tends to magnify the intrinsic non perfect collocation–duality properties of the velocity sensor and piezoelectric patch actuator at higher frequencies that generates instabilities and thus compromise the implementation of a velocity feedback loop.

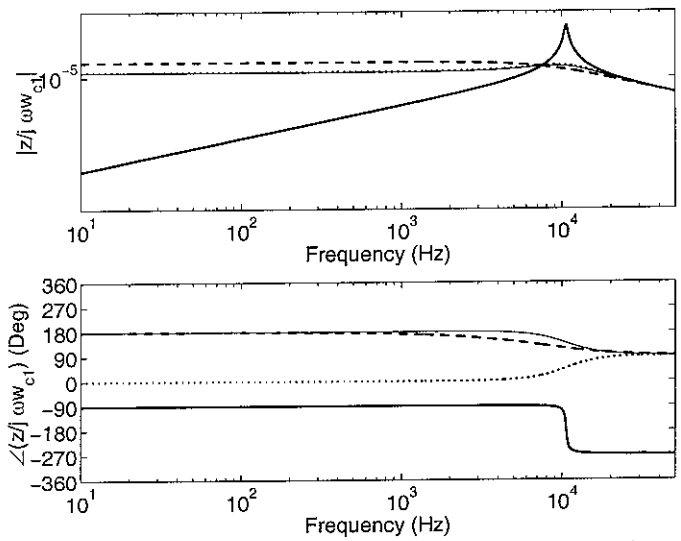


**Figure 46:** *amplitude (top plot) and phase (bottom plot) of the ratio between the relative displacement of the mass, $m_a$, and vibrating base and the velocity of the base of the sensor with embedded a feedback loop using an ideal velocity sensor when there is no feedback control gain (thick solid line) and when a velocity feedback loop is implemented with the control gain marked by a bullet in the solid line in Figure 44 $g_s$=5.35·10$^{-4}$ (faint solid line) or the control gain marked by a bullet in the dotted line in Figure 44, $g_s$=-5.35·10$^{-4}$ (dotted line) or a velocity feedback loop is implemented with the control gain that generates maximum damping $\overline{g}_s$ given by the dashed line in Figure 44 (dashed line).*

As discussed above, the fundamental resonance of the principal sensor could be damped down by implementing a control gain $\overline{g}_s = c_a\left(\frac{1}{\zeta_a} - 1\right)$, which is given by the dashed line in Figure 44, that would produce a critical damping ration $\overline{\zeta}_a$. Indeed the dashed line in Figure 46

shows that when the control gain $\bar{g}_s$ is implemented then the response of the sensor in the vicinity of the resonance frequency of the principal sensor is completely flatten and monotonically falls down at higher frequencies. It is interesting to note that the control gain $\bar{g}_s$ generates a low frequency output with phase 180° so that the relative displacement between the inertial mass, $m_a$, and the vibrating base of the principal sensor, and thus the output signal of the velocity sensor, is proportional to the opposite of the velocity of the base. However, the high levels of active damping generated by the feedback control system embedded in sensor tend to stretch out the phase change in the vicinity of the resonance frequency. As a result the relative displacement between the inertial mass, $m_a$, and the vibrating base of the sensor is constrained to be directly proportional to the opposite of the velocity of the base of the velocity sensor only at relatively low frequencies such that $\Omega < 1/25$, that is for $\omega < \omega_a/25$.

The implementation of a negative feedback control loop with a fixed control gain is much more practical than that with a frequency shaped control gain. A reasonable approach will therefore be the implementation of a fixed control gain that produces a relative displacement between the inertial mass, $m_a$, and the base of the sensor proportional to the opposite of the velocity of the base up to a certain fraction of the natural frequency $\Omega_{\max} < 1$ and also produces enough active damping effect in such a way as to cancel the amplification effect of the resonance of the principal sensor so that the relative displacement between the inertial mass, $m_a$, and the vibrating base of the principal sensor, and thus the output signal of the velocity sensor, monotonically rolls off from about $\Omega = 1$, that is $\omega = \omega_a$. A trial and error approach has been used to chose the fixed feedback gain from the optimal ones given in Figure 44. Figure 46 show the response of the accelerometer when the optimal fixed feedback gain for $\Omega = 0.645$, $\breve{g}_s = 5.35 \cdot 10^{-4}$, highlighted by the bullet points in Figure 44, is implemented at all frequencies. With this fixed feedback gain the relative displacement between the inertial mass, $m_a$, and the vibrating base of the principal sensor is found to be proportional to the velocity of the base of the velocity sensor up to about $\Omega = 0.5$, that is $\omega = \omega_a/2$.

The stability of the velocity feedback control system embedded in the principal sensor can be analysed by considering equation (4.1) when $w_{c1} = 0$ so that

$$\frac{\dot{w}_{c1}}{f_s} = \frac{j\omega}{k_a - \omega^2 m_a + j\omega c_a} = \frac{j\omega}{k_a} H\left(\frac{\omega}{\omega_a}\right) = \frac{j\omega}{k_a}\left|H\left(\frac{\omega}{\omega_a}\right)\right| e^{-j\phi}, \tag{4.21}$$

where, as defined in the previous chapter

$$H\left(\frac{\omega}{\omega_a}\right) = \frac{1}{\left(1 - \frac{\omega^2}{\omega_a^2}\right) + j2\zeta_a \frac{\omega}{\omega_a}} \tag{4.22}$$

and

$$\left|H\left(\frac{\omega}{\omega_a}\right)\right| = \frac{1}{\left[\left(1 - \frac{\omega^2}{\omega_a^2}\right)^2 + \left(2\zeta_a \frac{\omega}{\omega_a}\right)^2\right]^{\frac{1}{2}}}, \qquad \tan\phi = \frac{2\zeta_a \frac{\omega}{\omega_a}}{1 - \left(\frac{\omega}{\omega_a}\right)^2}. \tag{4.23b,c}$$

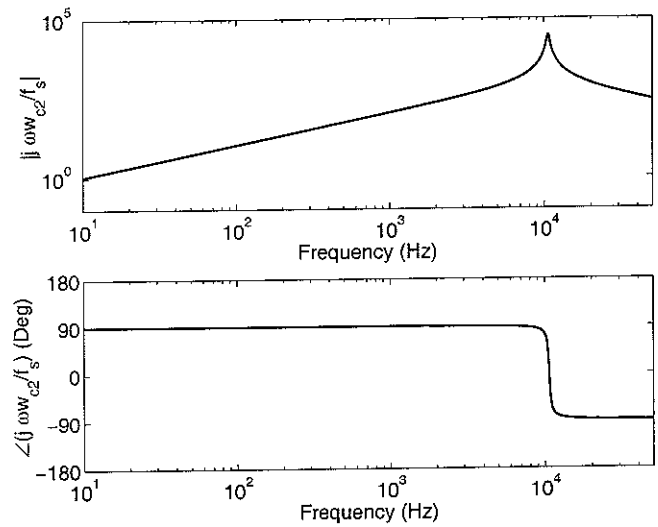


**Figure 47:** *amplitude (top plot) and phase (bottom plot) of the ratio between the velocity of the inertial mass, $m_a$, and the control force, $f_s$, of the velocity feedback control system embedded in the accelerometer.*

Figure 47 shows the Nyquist plot of the frequency response function between the velocity, $\dot{w}_{c2}$, measured by the ideal velocity control sensor mounted on the inertial mass, $m_a$, and the control force $f_s$ exerted by the actuator embedded in the principal sensor. This plot confirms that the negative velocity feedback loop embedded in the principal sensor is unconditionally stable.

## 4.2 Velocity sensor and piezoelectric patch actuator frequency response function when an ideal velocity control sensor is considered for the internal feedback control loop.

In this section the frequency response function between the signal output from the velocity sensor described in the previous section and the input signal to the closely located piezoelectric patch actuator is studied. As shown in Figure 48, the base of the accelerometer is mounted on the plate at the control position. As discussed in chapter 3, the fully coupled equations of motion of the plate with the piezoelectric patch actuator and the velocity sensor with embedded a velocity feedback control loop have been derived considering the system composed by four elements: first the plate, second the equivalent lumped mass of the piezoelectric patch actuator $m_{pzt}$; third, the elastic system which is made by a spring, $k_a$, and dashpot, $c_a$ of the principal sensor and fourth, the seismic mass $m_a$ of the principal sensor.

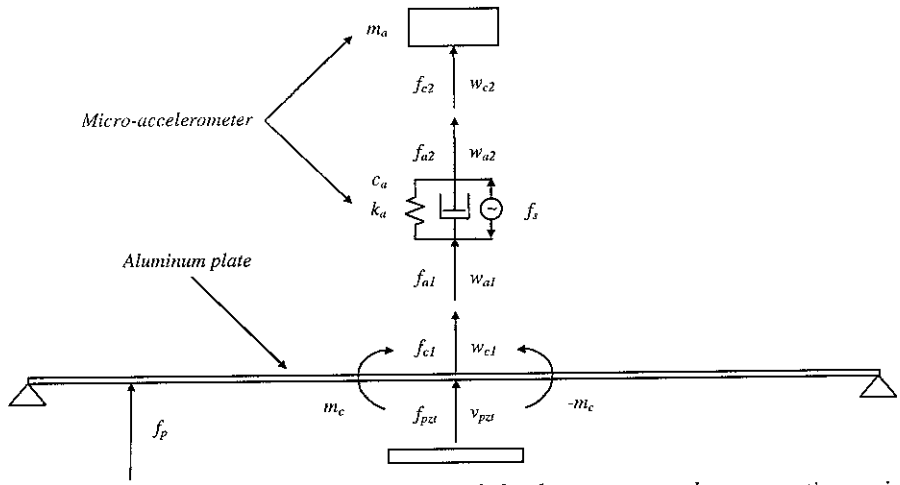


**Figure 48:** *scheme with the notation for the forces and displacements at the connecting points between the elements of the velocity sensor which is mounted on an aluminium plate with a closely located piezoelectric patch actuator.*

The velocities $\dot{w}_{c1}$ of the plate and $\dot{w}_{c2}$ of the inertial mass of the principal sensor have therefore been derived using the mobility model described in Sections 3.2 and 3.3. In order to take into account the effect of the control force generated by the feedback loop in the principal sensor, equation (3.43) has been modified as follows

$$\begin{Bmatrix} f_{c1} \\ f_{c2} \end{Bmatrix} = -\begin{bmatrix} Z_{11}^a & Z_{12}^a \\ Z_{21}^a & Z_{22}^a \end{bmatrix} \begin{Bmatrix} \dot{w}_{c1} \\ \dot{w}_{c2} \end{Bmatrix} - \begin{bmatrix} Z_{pzt} & 0 \\ 0 & 0 \end{bmatrix} \begin{Bmatrix} \dot{w}_{c1} \\ \dot{w}_{c2} \end{Bmatrix} + \begin{bmatrix} +1 \\ -1 \end{bmatrix} f_s , \tag{4.24}$$

which can be written in the following compact form

$$\mathbf{f} = -\overline{\mathbf{Z}}\dot{\mathbf{w}} + \mathbf{h}_s f_s, \tag{4.25}$$

where:

$$\overline{\mathbf{Z}} = \begin{bmatrix} Z_{11}^a + Z_{pzt} & Z_{12}^a \\ Z_{21}^a & Z_{22}^a \end{bmatrix}, \qquad \mathbf{h_s} = \begin{bmatrix} +1 \\ -1 \end{bmatrix}. \tag{4.26a,b}$$

and $Z_{11}^a$, $Z_{12}^a$, $Z_{21}^a$, $Z_{22}^a$ and $Z_{pzt}$ are given in equations (3.27), (3.28) and (3.42). Substituting equation (4.25) into equation (3.16) and solving respect the velocity vector the following expression is derived:

$$\dot{\mathbf{w}} = (\mathbf{I} + \mathbf{Y}\overline{\mathbf{Z}})^{-1}\left\{\mathbf{Y}\mathbf{h}_s f_s + \mathbf{Y}_p f_p + \mathbf{Y}_c u_c\right\}, \tag{4.27}$$

where the matrices $\mathbf{Y}$, $\mathbf{Y}_p$ and $\mathbf{Y}_c$ are respectively given in equations (3.18), (3.20) and (3.21). When, as shown in Figure 49, a direct velocity feedback is implemented within the principal sensor, then the control force is give by:

$$f_s = -g_s \dot{w}_{c2} = -g_s \mathbf{d}_s \dot{\mathbf{w}}, \tag{4.28}$$

where

$$\mathbf{d}_s = [0 \quad 1]. \tag{4.29}$$

Thus equation (4.27) becomes

$$\dot{\mathbf{w}} = (\mathbf{I} + g_s(\mathbf{I} + \mathbf{Y}\overline{\mathbf{Z}})^{-1}\mathbf{Y}\mathbf{h}_s\mathbf{d}_s)^{-1}(\mathbf{I} + \mathbf{Y}\overline{\mathbf{Z}})^{-1}\left\{\mathbf{Y}_p f_p + \mathbf{Y}_c u_c\right\}. \tag{4.30}$$

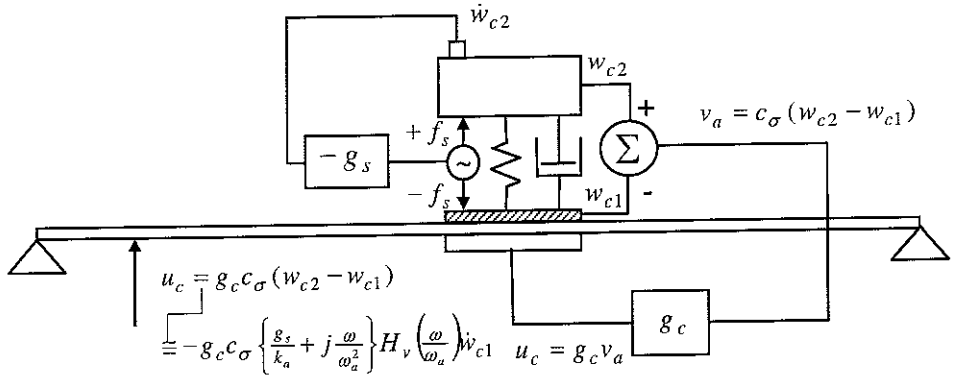


**Figure 49:** *scheme of the velocity sensor with embedded a velocity feedback control loop mounted on an aluminium plate with a closely located piezoelectric patch actuator.*

Following the scheme shown in Figure 49, the output signal provided by the elastic piezoelectric element in the principal sensor, which is proportional to the relative displacement between the seismic mass, $m_a$, and the vibrating base, that is $v_a = c_\sigma (w_{c2} - w_{c1})$, is first magnified by a constant gain $g_c$ and then feedback to the piezoelectric patch control actuator so that the input control signal to the piezoelectric patch control actuator is $u_c = g_c v_a = g_c c_\sigma (w_{c2} - w_{c1})$. Thus, according to the results discussed in previous section, provided the optimal control gain $\hat{g}_{s1}$ given by equation (4.19) is implemented, then $u_c = g_c c_\sigma \hat{H}_{g1}(\Omega)\dot{w}_{c1}$ where the function $\hat{H}_{g1}(\Omega)$ is real negative for all $\Omega$ so that $u_c = -g_c c_\sigma \left|\hat{H}_{g1}(\Omega)\right| \dot{w}_{c1}$. Thus a control excitation directly proportional to the opposite of the velocity at the control point is generated which indeed produces active damping. Alternatively if a fixed control gain is implemented in the feedback loop embedded in the velocity sensor, then $u_c = g_c c_\sigma H_g(\Omega)\dot{w}_{c1}$ where, in this case, the function $H_g(\Omega)$ is real negative only for a limited range of $\Omega < 1$. For example, if the control gain indicated with the positive bullet point in Figure 44 is implemented, then, according to Figure 46, $H_g(\Omega)$ is real negative up to about $\Omega \approx 0.5$ and thus the control signal feed to the piezoelectric patch is directly proportional to the base velocity only up to frequencies $\omega < 0.5\omega_a$. This implies that an active damping effect is generated indeed up to $\omega_a/2$.

As seen in section 3.2, the signal output from the principal sensor with embedded the velocity feedback control system could expressed in terms of the displacement vector

$\mathbf{w} = \{w_{c1} \quad w_{c1}\}^T$ with the following matrix relation

$$v_a = c_\sigma \mathbf{d}_c \mathbf{w}, \tag{4.31}$$

where

$$\mathbf{d}_c = [-1 \quad 1] \tag{4.32}$$

and, in this case, the displacement vector $\mathbf{w}$ can be derived by pre-multiplying equation (4.30) by $\frac{1}{j\omega}$ so that, assuming $f_p = 0$, the output signal from the sensor is given by

$$v_a = c_\sigma \mathbf{d}_c \left\{ \frac{1}{j\omega} (\mathbf{I} + g_s (\mathbf{I} + \mathbf{Y}\overline{\mathbf{Z}})^{-1} \mathbf{Y}\mathbf{h}_s \mathbf{d}_s)^{-1} (\mathbf{I} + \mathbf{Y}\overline{\mathbf{Z}})^{-1} \mathbf{Y}_c u_c \right\}. \tag{4.33}$$

Therefore, the open loop velocity sensor with embedded a velocity feedback loop and piezoelectric patch actuator frequency response function is given by

$$G(\omega) = \frac{v_a}{u_c} = \frac{c_\sigma}{j\omega} \mathbf{d}_c (\mathbf{I} + g_s (\mathbf{I} + \mathbf{Y}\overline{\mathbf{Z}})^{-1} \mathbf{Y}\mathbf{h}_s \mathbf{d}_s)^{-1} (\mathbf{I} + \mathbf{Y}\overline{\mathbf{Z}})^{-1} \mathbf{Y}_c, \tag{4.34}$$

where the mobility term $Y_{cc}$ in the vector $\mathbf{Y}_c$ is given by equation (2.7) with the modal excitation terms in equation (2.14).

Figure 50 shows the amplitude and phase of the frequency response function between the piezoelectric patch actuator and the velocity sensor with either the fixed control gain represented by the positive bullet point in Figure 44, $\breve{g}_s = \hat{g}_{s1}(\Omega = 0.645)$, (left hand side plot) or the maximum damping control gain $\overline{g}_s = c_a(1/\zeta_a - 1)$, (right hand side plot). In both cases the active damping generated by the velocity feedback loop in the principal sensor cuts down the resonance peak of the principal sensor. Also, as discussed in section 2.1, the higher frequencies roll off effect is not affected by the large amount of damping introduced by the velocity feedback loop. Finally the phase plot indicates that, up to about 10 kHz, the phase of the signal output from this sensor corresponds to that obtained with the accelerometer sensor

and an ideal time integrator which is shown in Figure 25. Therefore the phase is confined between $\pm 90^o$ up to about 4 kHz while at higher frequencies there is a constant phase lag which however is not characterised by the brusque $-180^o$ drop at the resonance frequency so that the phase falls down less rapidly and thus at 50 kHz there is a phase lag of $-450^o$ against the $-540^o$ shown in Figure 25 for the accelerometer sensor with ideal time integrator.

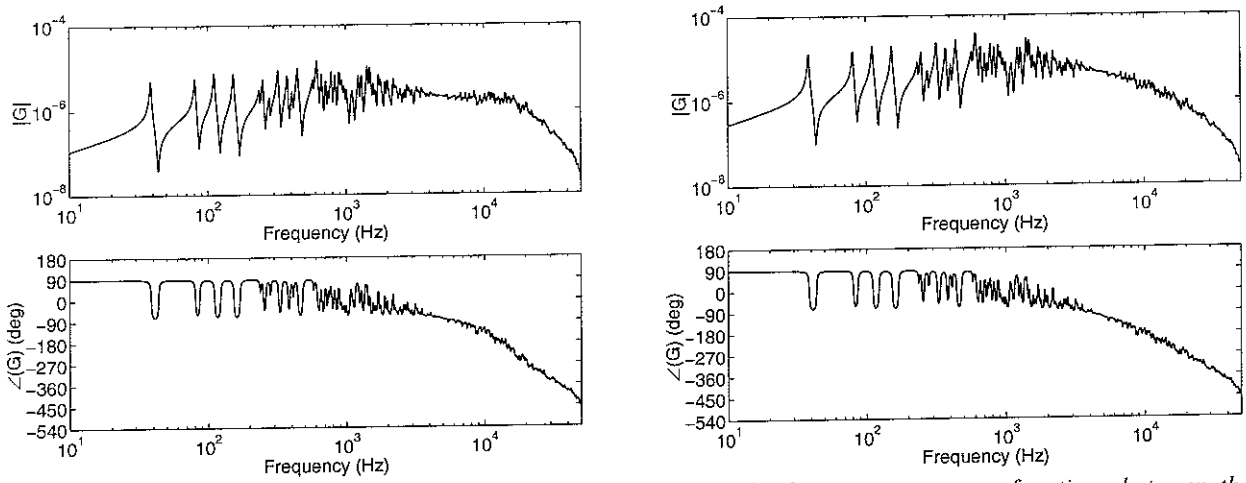


**Figure 50:** *amplitude (top plot) and phase (bottom plot) of the frequency response functions between the piezoelectric patch actuator and the velocity sensor with either the fixed control gain indicated by the bullet point in figure 44 (left hand side plot) or with the maximum damping gain given by equation (4.13) (right hand side plot).*

Figure 51 shows the Nyquist plots of the frequency response functions between the piezoelectric patch actuator and the sensor with either the fixed control gain $\breve{g}_s = \hat{g}_{s1}(\Omega = 0.645)$ (left hand side plot) or the maximum damping control gain $\overline{g}_s = c_a\left(1/\zeta_a - 1\right)$ (right hand side plot). Both plots show the benefit of the active damping generated by the feedback control loop in the sensor which cuts the higher frequency resonance peak in such a way as the frequency response function gently rolls off above about 4 kHz and thus the loops in the left hand side of the two Nyquist plots are much smaller than those on the co-respective right hand sides. Therefore, although the control system is still conditionally stable, now it is possible to implement realistic control gains that would produce enough active damping without compromising the stability of the system.

At first sight Figures 50 and 51 highlights little differences between the cases where the internal loop implements a control gain that either gives a velocity output over a wider frequency band or maximise the active damping effect over the fundamental resonance

frequency of the system. Indeed this is true when the stability of the control system is considered, however it is important to underline that in order to generate active damping the piezoelectric patch control actuator must be driven by a signal proportional to velocity. Thus although the output signals of the velocity sensor for the two internal control gains are relatively small they are not negligible when it comes into consideration the effective damping action generated by the control piezoelectric patch actuator.

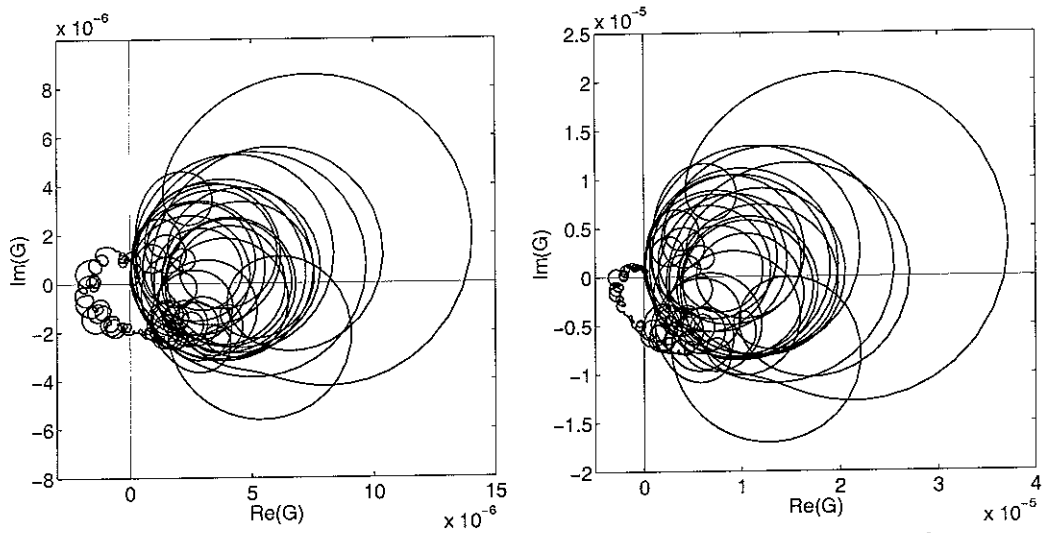


**Figure 51:** *Nyquist plots of frequency response functions between the piezoelectric patch actuator and the velocity sensor with either the fixed control gain indicated by the bullet point in figure 44 (left hand side plot) or with the maximum damping gain given by equation (4.13) (right hand side plot).*

The parametric analysis presented in sections 3.4 and 3.5 showed that the smaller is the piezoelectric patch actuator the higher will be the cut off frequency where the phase delay exceed $-90^{o}$. Also, as the mass of the piezoelectric patch actuator is increased as the higher frequency rise of the modulus of the velocity sensor and piezoelectric patch actuator frequency response function is attenuated. Therefore the stability of the sensor–actuator system could be improved by appropriately choosing the size and mass of the actuator patch.

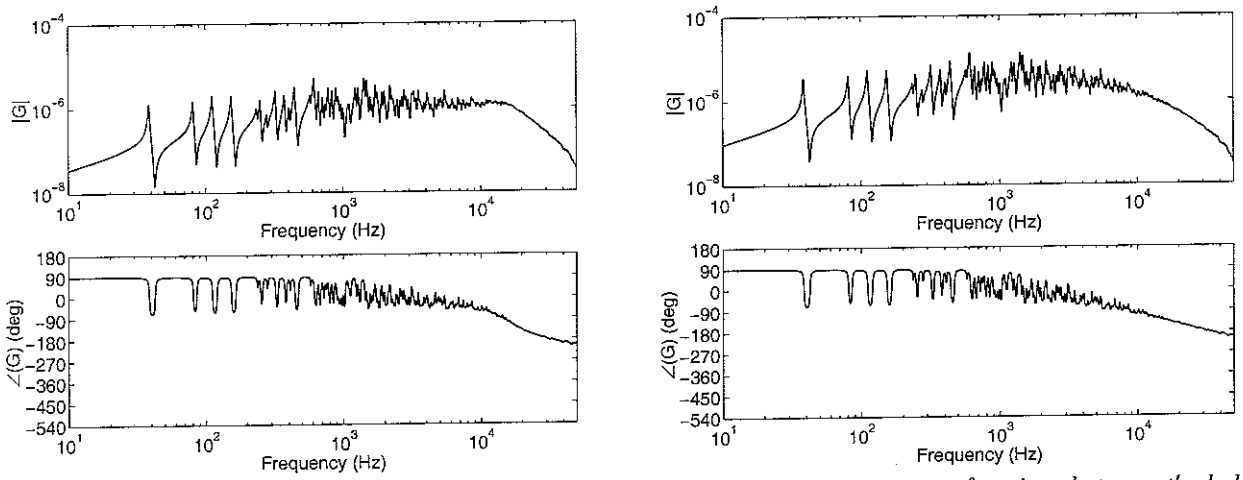


**Figure 52:** *amplitude (top plot) and phase (bottom plot) of the frequency response functions between the half size and 4.1 g mass piezoelectric patch actuator and the velocity sensor with either the feedback gain indicated by the bullet point in figure 44 (left hand side plot) or with the maximum damping gain given by equation (4.13) (right hand side plot).*

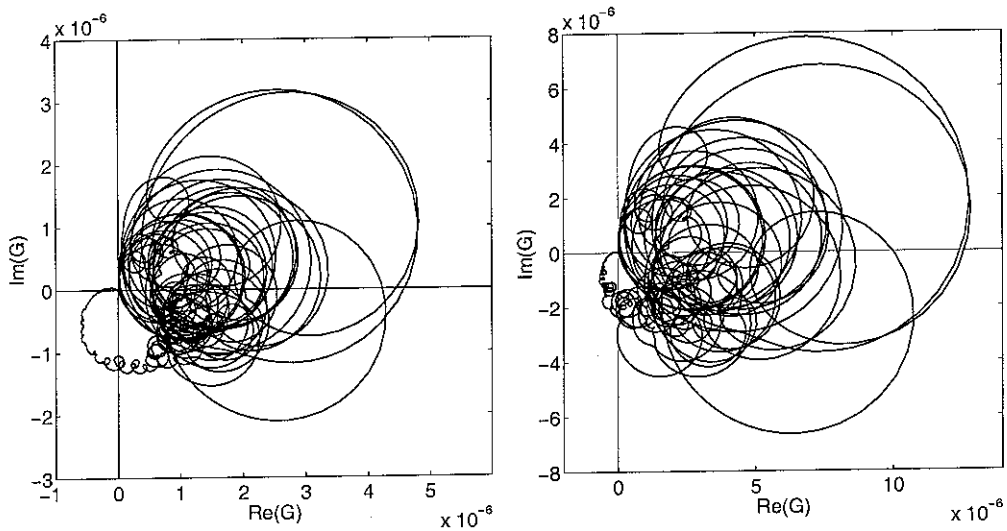


**Figure 53:** *Nyquist of the frequency response functions between the half size and 4.1 g mass piezoelectric patch actuator and the velocity sensor with either the feedback gain indicated by the bullet point in figure 44 (left hand side plot) or with the maximum damping gain given by equation (4.13) (right hand side plot).*

For example Figures 52 and 53 show the amplitude–phase and Nyquist plots for a sensor–actuator pair where the piezoelectric patch actuator dimensions are reduced to half, that is $a_x \times a_y = 15 \times 15$ mm, but the total weight is left unaltered to 4.1 g by increasing the thickness of the patch by a factor of 4, that is $h_{pe} = 2$ mm. Both figures highlights that having reduced the size of the patch but kept its total mass to be the same gives a sensor–actuator pair with a larger gain margin since the relative size of the loop on the left hand side and those on the

right hand side of Nyquist plots is much smaller that that found in the previous case as shown in the two plots of Figure 51.

The stability of the internal feedback loop embedded in the sensor can be assessed by considering equation (4.27) when the primary force is set to zero so that:

$$\dot{\mathbf{w}} = (\mathbf{I} + \mathbf{Y}\overline{\mathbf{Z}})^{-1}\{\mathbf{Y}\mathbf{h}_s f_s + \mathbf{Y}_c u_c\}. \tag{4.35}$$

According to the formulation presented in section 4.1 the output signal from the sensor is proportional to the opposite of the base velocity, thus in order to implement velocity feedback, the control signal input to the piezoelectric patch actuator is set to be

$$u_c = g_c v_a = g_c c_\sigma (w_{c2} - w_{c1}). \tag{4.36}$$

Therefore equation (4.35) becomes

$$\dot{\mathbf{w}} = \left(\mathbf{I} - (\mathbf{I} + \mathbf{Y}\overline{\mathbf{Z}})^{-1}\mathbf{Y}_c g_c \frac{c_\sigma}{j\omega}\mathbf{d}_c\right)(\mathbf{I} + \mathbf{Y}\overline{\mathbf{Z}})^{-1}\mathbf{Y}\mathbf{h}_s f_s, \tag{4.37}$$

so that, the ratio between the velocity of the seismic mass of the principal sensor, $m_a$, and the control force generated by the feedback control loop embedded in the sensor, $f_s$, is given by

$$\frac{\dot{w}_{c2}}{f_s} = G_s = \mathbf{d}_s\left(\mathbf{I} - (\mathbf{I} + \mathbf{Y}\overline{\mathbf{Z}})^{-1}\mathbf{Y}_c g_c \frac{c_\sigma}{j\omega}\mathbf{d}_c\right)(\mathbf{I} + \mathbf{Y}\overline{\mathbf{Z}})^{-1}\mathbf{Y}\mathbf{h}_s \quad . \tag{4.38}$$

Figure 54 shows the open loop frequency response function between the velocity of the seismic mass of the principal sensor, $m_a$, and the control force generated by the feedback control loop embedded in the sensor, $f_s$, when either the fixed control gain $\breve{g}_s = \hat{g}_{s1}(\Omega = 0.645)$ (solid line) or the maximum damping control gain $\overline{g}_s = c_a(1/\zeta_a - 1)$ (dashed line) are used in the feedback loop to drive the piezoelectric patch.

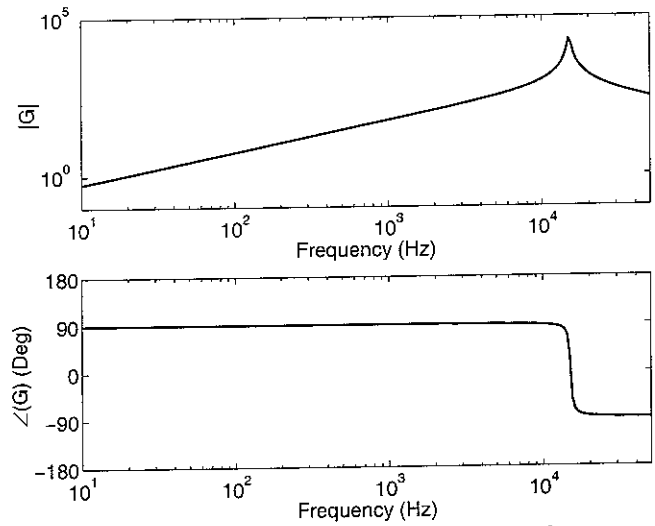


**Figure 54:** *amplitude (top plot) and phase (bottom plot) of the open loop frequency response function between the velocity of the seismic mass of the principal sensor, $m_a$, and the control force generated by the feedback control loop embedded in the sensor, $f_s$.*

This figure indicates that the internal control loop in the sensor is not affected by the dynamics effects of the plate structure and piezoelectric patch actuator. As a result the response is characterised by the fundamental resonance of the principal sensor spring–mass system so that the phase is constrained between $\pm 90^o$ which guarantees that the internal loop is unconditionally stable.

## 4.3 Velocity sensor response function when the velocity feedback control loop is implemented using a practical accelerometer sensor with time integrator

The study presented in section 4.1 for the velocity sensor with internal feedback loop does not take into account the dynamics effects and the true response of the sensor that provides the signal proportional to the velocity of the inertial mass $m_a$. In this section the dynamics effects of an accelerometer sensor mounted on the inertial mass $m_a$ are therefore considered. Also the response of an R-C analogue integrator as that presented in section 3.4 will be considered.

As shown in Figure 53 below, the velocity sensor used for the internal feedback control loop is a standard seismic accelerometer with a spring, $k_s$, a damper, $c_s$, and a mass, $m_s$, which has higher natural frequency $\omega_s = \sqrt{k_s / m_s}$ than that of the principal mass–spring velocity sensor which is given by $\omega_a = \sqrt{k_a / m_a}$ .

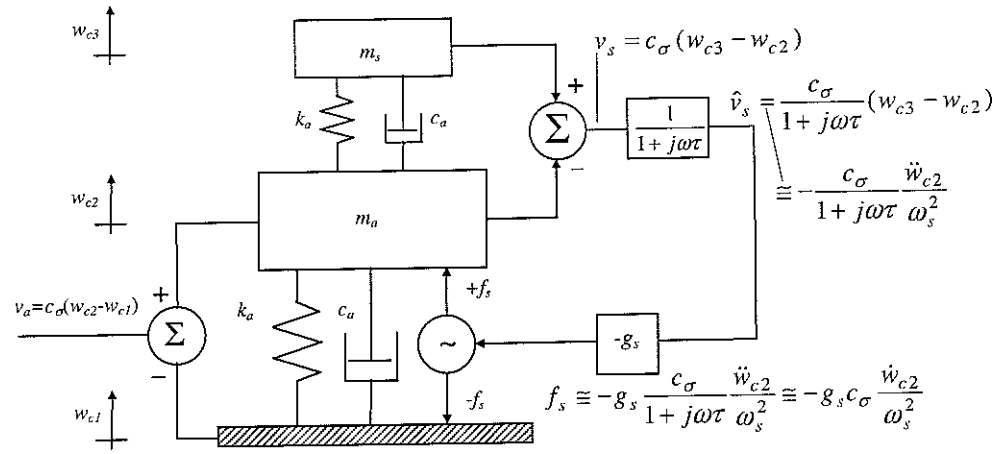


**Figure 53:** *schematic representation of the velocity sensor with an accelerometer mounted on the seismic mass $m_a$.*

In this case, the output signal provided by the elastic piezoelectric element of the accelerometer is proportional to the relative displacement between the inertial masses $m_a$ and $m_s$, that is

$$v_s = c_\sigma (w_{c3} - w_{c2}). \tag{4.39}$$

According to section 3.1, at frequencies lower than the fundamental resonance frequency, $\sqrt{1-2\zeta_s}\omega_s$, where $\zeta_s = c_s / 2m_s\omega_s$, the signal output is proportional to the acceleration of the inertial mass $m_a$, that is $v_s \cong -c_\sigma \frac{\ddot{w}_{c2}}{\omega_s^2}$. Therefore, in order to implement a direct velocity feedback control loop that drives the control forces $\pm f_s$ in such a way as to produce active damping on the mass $m_a$, the output signal from the accelerometer must be integrated for example with an R-C analogue circuit as shown in Figure 27 with time integration constant $\tau = RC$ such that the cut off frequency $\omega_c = \frac{1}{\tau} = \frac{1}{RC}$ is equal to 20 Hz. Thus, as shown in Figure 53, the integration transfer function given by equation (3.47) is also taken into account in the analysis of the system so that the signal feedback to the control actuator is proportional to

$$\hat{v}_s = -\frac{c_\sigma}{1+j\omega\tau}(w_{c3} - w_{c2}), \tag{4.40}$$

via a constant positive feedback gain $g_s$. In this way, at frequencies higher than the integration cut off frequency, $\omega_c = 1/RC$, and lower than the fundamental resonance frequency of the accelerometer sensor, $\sqrt{1-2\zeta_a}\omega_s$, the control forces $\pm f_s$ are directly proportional to the opposite of the velocity of the mass $m_a$, $\hat{v}_s \cong -c_\sigma \frac{\ddot{w}_{c2}}{j\omega\tau\omega_s^2} = -c_\sigma \frac{\dot{w}_{c2}}{\tau\omega_s^2}$, so that active damping could be produced. It must be underlined that once the accelerometer sensor is mounted on the mass–spring system of the principal sensor then its natural frequency should be referred to the second natural frequency of the two degrees of freedom spring–mass–spring–mass system which, as known from text books [5], it is slightly higher than that of the accelerometer on its own.

The equations of motion for the two degrees of freedom system shown in Figure 53 can be derived by applying Newton's second law to the two masses so that:

$$\begin{cases} m_a\ddot{w}_{c2} + c_a(\dot{w}_{c2} - \dot{w}_{c1}) - c_s(\dot{w}_{c3} - \dot{w}_{c2}) + k_a(w_{c2} - w_{c1}) - k_s(w_{c3} - w_{c2}) = f_s \\ m_s\ddot{w}_{c3} + c_s(\dot{w}_{c3} - \dot{w}_{c2}) + k_s(w_{c3} - w_{c2}) = 0 \end{cases}, \quad (4.41)$$

where $w_{c1}$, $w_{c2}$ and $w_{c3}$ are respectively the displacement of the vibrating base, of the mass $m_a$ and of the mass $m_s$. If the relative displacement between the seismic masses $m_s$ and $m_a$ and between the seismic mass $m_a$ and vibrating base are respectively:

$$s = w_{c3} - w_{c2}, \quad (4.42)$$

$$z = w_{c2} - w_{c1}, \quad (4.43)$$

then equation (4.39) can be rewritten in the following form:

$$\begin{cases} m_a\ddot{z} + c_a\dot{z} - c_s\dot{s} + k_a z - k_s s = f_s - m_a\ddot{w}_{c1} \\ m_s\ddot{s} + c_s\dot{s} + k_s s = -m_s\ddot{w}_{c2} \end{cases}. \quad (4.44)$$

According to the notation introduced in sections 2.2 and 3.1, the harmonic motions of the base

and seismic masses are defined as:

$$w_{c1}(t) = \mathrm{Re}\left\{w_{c1}(\omega)e^{j\omega t}\right\} \quad , \quad w_{c2}(t) = \mathrm{Re}\left\{w_{c2}(\omega)e^{j\omega t}\right\} \quad , \quad w_{c2}(t) = \mathrm{Re}\left\{w_{c2}(\omega)e^{j\omega t}\right\} \quad (4.45a\text{-}c)$$

and thus

$$z(t) = \mathrm{Re}\left\{z(\omega)e^{j\omega t}\right\}, \qquad s(t) = \mathrm{Re}\left\{s(\omega)e^{j\omega t}\right\}, \qquad (4.46a,b)$$

where $w_{c1}(\omega)$, $w_{c2}(\omega)$ $w_{c3}(\omega)$ are respectively the phasors of the motion of the base and inertial masses $m_a$ and $m_s$ and $z(\omega)$, $s(\omega)$ are respectively the phasors of the relative displacement between the mass $m_a$ and the vibrating base and between the two masses $m_a$ and $m_s$. Substituting equations (4.45) and (4.46) into equation (4.44) it is found:

$$\begin{cases} (-\omega^2 m_a + j\omega c_a + k_a)ze^{j\omega t} - (j\omega c_s + k_s)se^{j\omega t} = \omega^2 m_a w_{c1} e^{j\omega t} + f_s \\ (-\omega^2 m_s + j\omega c_s + k_s)se^{j\omega t} = \omega^2 m_s w_{c2} e^{j\omega t} \end{cases} . \qquad (4.47)$$

As mentioned above, the internal feedback loop drives the control force $f_s$ with a signal proportional to the output signal from the control accelerometer sensor with an R-C integrator, $\hat{v}_s$, via a fixed control gain, $g_s$, so that,

$$f_s = g_s \frac{c_\sigma}{1 + j\omega\tau} s \, . \qquad (4.48)$$

Supposing the time dependent terms $\exp(j\omega t)$ to be implicit in all expressions the two equations in (4.47) become

$$\begin{cases} (-\omega^2 m_a + j\omega c_a + k_a)z - (j\omega c_s + k_s)s = \omega^2 m_a w_{c1} + g_s \dfrac{c_\sigma}{1 + j\omega\tau} s \\ (-\omega^2 m_s + j\omega c_s + k_s)s = \omega^2 m_s w_{c2} \end{cases} . \qquad (4.49)$$

The second equation in (4.49) can be expressed in terms of the base displacement since $\omega^2 m_s w_{c2} = \omega^2 m_s z + \omega^2 m_s w_{c1}$ and thus

$$\begin{cases} A_a z - A_s s = +g_s I s + M_a w_{c1} \\ B_s s = M_s z + M_s w_{c1} \end{cases}, \tag{4.50}$$

where

$$A_a = (-\omega^2 m_a + j\omega c_a + k_a), \qquad A_s = (j\omega c_s + k_s), \quad B_s = (-\omega^2 m_s + j\omega c_s + k_s) \tag{4.51a-c}$$

and

$$I = \frac{c_\sigma}{1 + j\omega\tau}, \qquad M_s = \omega^2 m_s, \qquad M_a = \omega^2 m_a. \tag{4.52a-c}$$

Isolating the relative displacement between the two inertial masses $m_s$ and $m_a$, $s$, the second equation in (4.50) gives

$$s = \frac{M_s}{B_s}\{z + w_{c1}\}, \tag{4.53}$$

which can be substituted into the first equation in (4.50) so that the relative displacement between the inertial mass $m_a$ and the base, $z$, can be expressed in terms of the base displacement $w_{c1}$

$$z = \frac{B_s M_a + (A_s + g_s I) M_s}{B_s A_a - (A_s + g_s I) M_s} w_{c1}. \tag{4.54}$$

Therefore the ratio between the relative displacement of the inertial mass, $m_a$, and vibrating base and the velocity of the base itself is given by

$$\frac{z}{j\omega w_{c1}} = \frac{z}{\dot{w}_{c1}} = \frac{1}{j\omega}\frac{B_s M_a + (A_s + g_s I)M_s}{B_s A_a - (A_s + g_s I)M_s}. \tag{4.55}$$

The solid and dashed lines in Figure 55 give the two control gains, $\hat{g}^i_{s1,2}(\alpha)$, that, considering the accelerometer sensor with an ideal integrator such that $I = 1/j\omega$, would produce an output signal from the principal sensor, $v_a$, exactly proportional to the velocity of the vibrating base. Also in this case only the feedback gains of the solid line could be implemented in practice since those given by the dotted line would produce a positive velocity feedback loop which is intrinsically unstable.

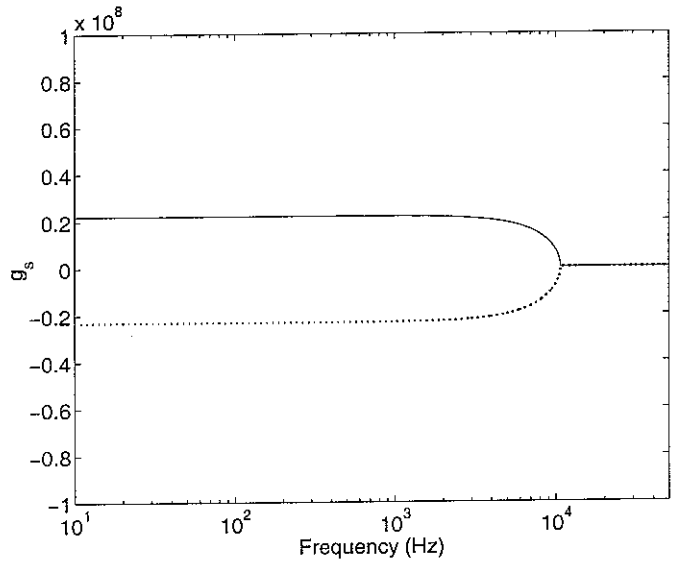


**Figure 55:** *control gains of the velocity feedback control loop embedded in the velocity sensor using an accelerometer sensor with ideal integrator that would produce an output signal from the principal sensor directly proportional to the base velocity (solid and dotted lines).*

Figure 56 shows the amplitude and phase of the ratio between the relative displacement of the mass $m_a$ and vibrating base, $z$, and the velocity of the base, $\dot{w}_{c1}$, considering the control accelerometer with an ideal time integrator in the internal feedback loop, when there is no feedback control gain (thick solid line) or a negative velocity feedback loop is implemented with the optimal control gain given by the solid line in Figure 55 (faint solid line) and, for completeness, with the optimal control gain given by the dotted line in Figure 55 (dotted line). This plot confirms that in the ideal case where the control gain functions brings to zero the imaginary part in equation (4.55) are implemented then the relative displacement between the

inertial mass, $m_a$, and the base of the accelerometer, $z$, and thus the velocity sensor output signal, $v_a$, is directly proportional to the velocity at the base of the sensor, $\dot{w}_{c1}$. In particular, when the control gain function described by the solid line in Figure 55 is implemented, then the relative displacement between the inertial mass, $m_a$, and the base, $z$, is proportional to the opposite of the velocity at the base of the sensor, $\dot{w}_{c1}$.

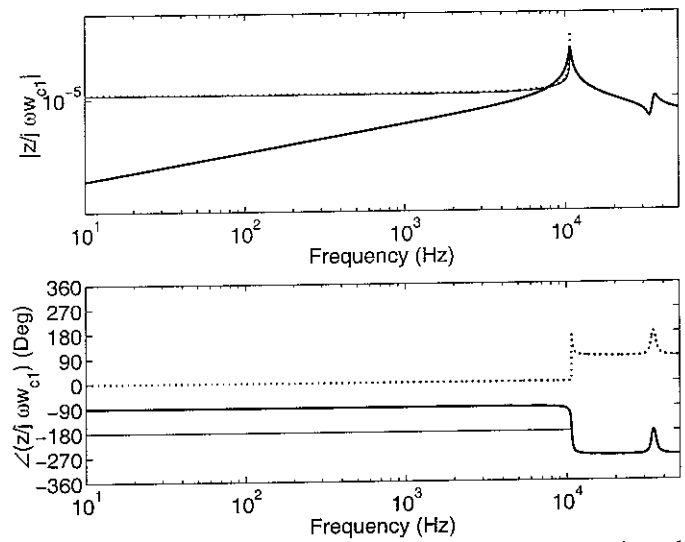


**Figure 56:** *amplitude (top plot) and phase (bottom plot) of the ratio between the relative displacement of the mass, $m_a$, and vibrating base and the velocity of the base of the sensor with embedded a feedback loop using an accelerometer sensor with ideal time integrator when there is no feedback control gain (thick solid line) or a velocity feedback loop is implemented with the control gains of the solid line in Figure 55 (faint solid line) or the control gains of the dotted line in Figure 55 (dotted line).*

The solid and dashed lines in Figure 57 give the two control gains, $\hat{g}^r_{s1,2}(\alpha)$, that, considering the accelerometer control sensor with an R-C analogue integrator such that $I = \dfrac{1}{1 + j\omega\tau}$, would produce an output signal from the principal sensor, $v_a$, exactly proportional to the velocity of the vibrating base. Again only the feedback gains of the solid line could be implemented in practice since those given by the dotted line would produce a positive velocity feedback loop which is intrinsically unstable. The two curves are quite similar to those found in Figure 55 except at low frequencies where the time integration of the signal output from the control accelerometer with the R-C system does not provide the necessary velocity signal for the feedback loop.

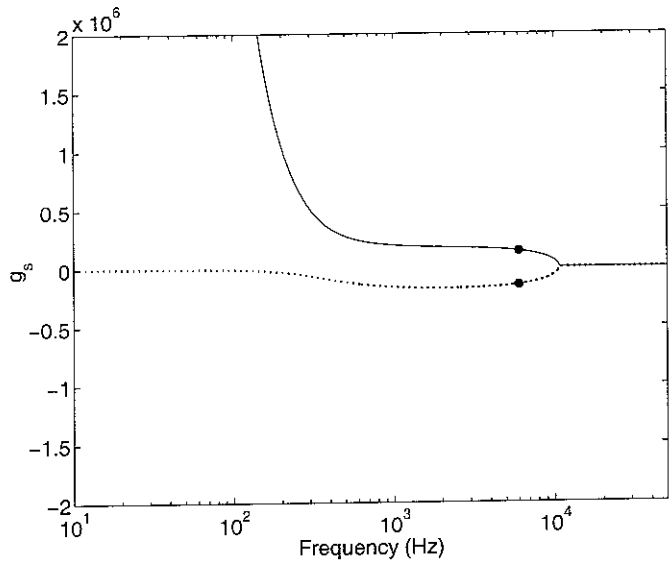


**Figure 57:** *control gains of the velocity feedback control loop embedded in the velocity sensor using an accelerometer sensor with an R-C time integrator that would produce an output signal from the principal sensor directly proportional to the base velocity (solid and dotted lines).*

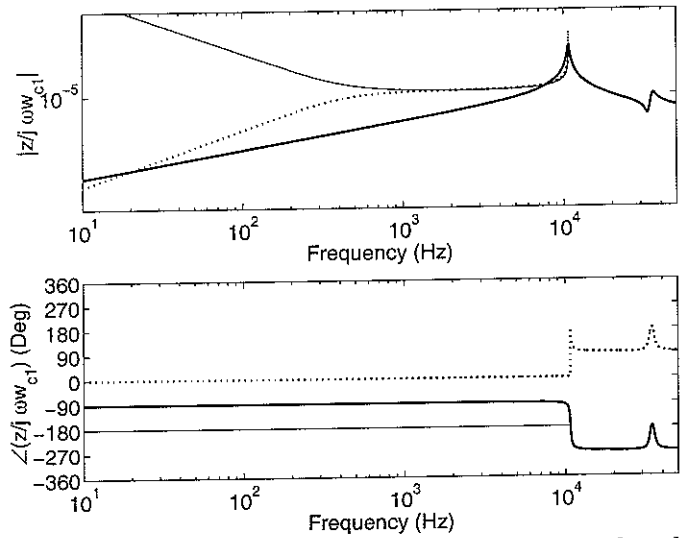


**Figure 58:** *amplitude (top plot) and phase (bottom plot) of the ratio between the relative displacement of the mass, $m_a$, and vibrating base and the velocity of the base of the sensor with embedded a feedback loop using an accelerometer sensor with an R-C time integrator when there is no feedback control gain (thick solid line) or a velocity feedback loop is implemented with the control gains of the solid line in Figure 57 (faint solid line) or the control gains of the dotted line in Figure 57 (dotted line).*

Figure 58 shows the amplitude and phase of the ratio between the relative displacement of the mass $m_a$ and the vibrating base, $z$, and the velocity of the base, $\dot{w}_{c1}$, considering the control accelerometer with an R-C analogue time integrator in the internal feedback loop, when there is no feedback control gain (thick solid line) or a negative velocity feedback loop is implemented with the optimal control gain given by the solid line in Figure 57 (faint solid line) and, for completeness, with the optimal control gain given by the dotted line in Figure 57

(dotted line). Also in this case it is found that the relative displacement between the inertial mass, $m_a$, and the base of the accelerometer, $z$, is directly proportional to the velocity at the base of the sensor, $\dot{w}_{c1}$. However, at relatively low frequencies the approximation introduced by the R-C analogue integrator produces either a lowering or rising effect for the modulus of the response function.

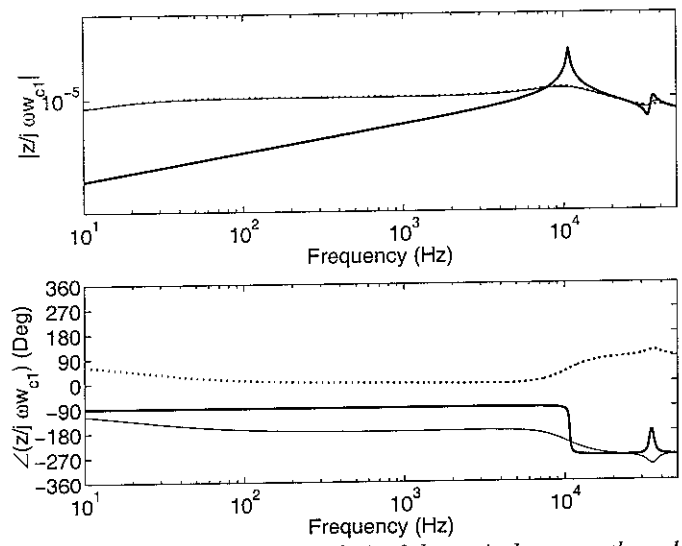


**Figure 59:** *amplitude (top plot) and phase (bottom plot) of the ratio between the relative displacement of the mass, $m_a$, and vibrating base and the velocity of the base of the sensor with embedded a feedback loop using an accelerometer sensor with an R-C time integrator when there is no feedback control gain (thick solid line) or a velocity feedback loop is implemented with the fixed control gain marked by a bullet in the solid line in Figure 57 (faint solid line) or with the fixed control gain marked by a bullet in the solid line in Figure 57 (dotted line).*

Figure 59 show the response of the velocity sensor when the fixed feedback gains for $\omega = 6000\,\text{Hz}$, $\breve{g}_s = 1.4116 \cdot 10^{-5}$, highlighted by the bullet points in Figure 57, are implemented at all frequencies. With this fixed feedback gains the relative displacement between the inertial mass, $m_a$, and the vibrating base of the sensor, $z$, is found to be proportional to the velocity of the base of the sensor, $\dot{w}_{c1}$, up to relatively high frequencies close to the fundamental resonance of the two degrees of freedom sensor.

The stability of the feedback control system embedded in the sensor can be analysed by considering equation (4.47) when $w_{c1} = 0$ so that, considering the terms defined in equations (4.51) and (4.52) it is found

$$\begin{cases} A_a z - A_s s = f_s \\ B_s s = M_s z \end{cases} \tag{4.56}$$

and thus

$$s = \frac{M_s}{A_a B_s - A_s M_s} f_s . \tag{4.57}$$

Therefore, the ratio between the integrated output signal from the accelerometer sensor, $\hat{v}_s$, and the internal control force $f_s$ is given by

$$\frac{\hat{v}_s}{f_s} = I \frac{M_s}{A_a B_s - A_s M_s} . \tag{4.58}$$

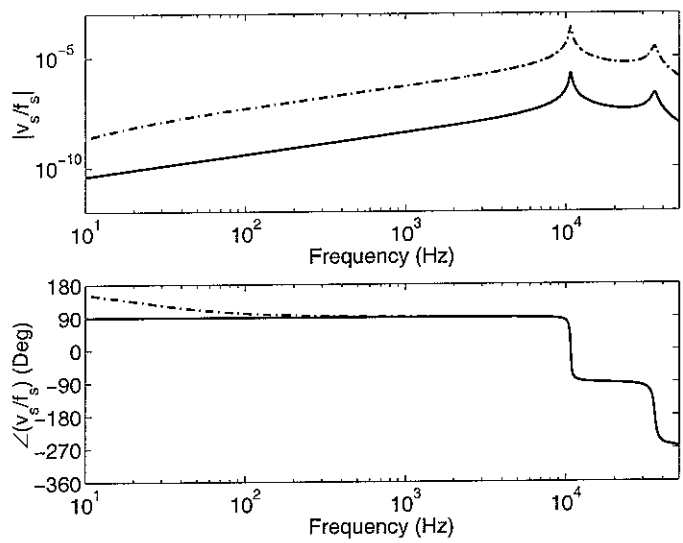


**Figure 60:** *amplitude (top plot) and phase (bottom plot) of the open loop frequency response function between the output signal of the control accelerometer with an ideal time integrator (solid line) or an analogue R-C time integrator (dashed line) and control force generated by the feedback control loop embedded in the sensor, $f_s$.*

Figure 60 shows the modulus and phase of the frequency response function of the internal sensor–actuator control system for the control loop using an ideal or an R-C analogue integrator. As one would expect, the two degrees of freedom spring–mass–spring–mass system generates two resonances which are characterised by 180° phase shifts so that at higher frequencies the phase exceed -90°.

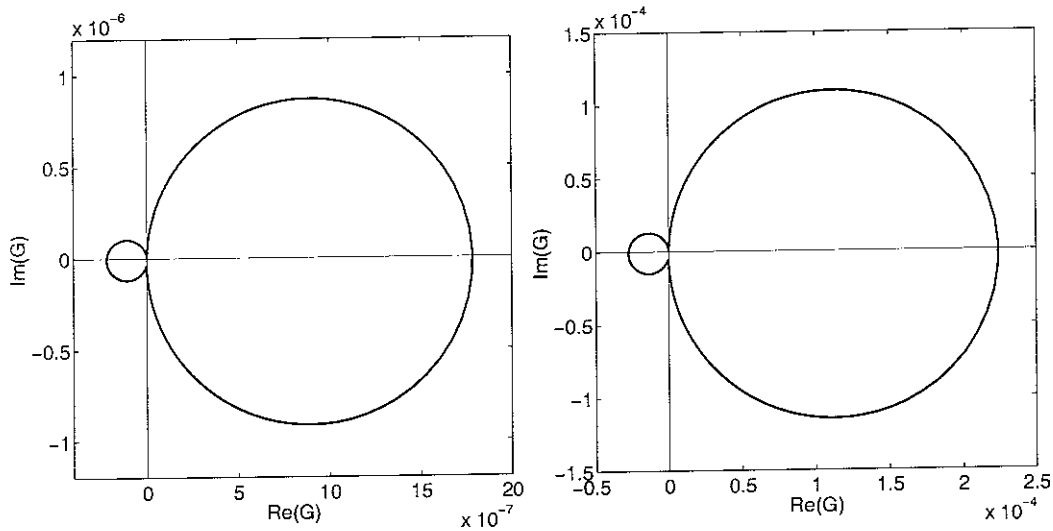


**Figure 61:** *Nyquist plots of the frequency response function of the open loop frequency response function between the output signal of the control accelerometer with an ideal time integrator (left hand side plot) or an analogue R-C time integrator (right hand side plot) and control force generated by the feedback control loop embedded in the sensor, $f_s$.*

The two Nyquist plots in Figure 61 confirms that the second resonance generated by the presence of the accelerometer mounted on the mass $m_a$, produces a second loop which is exactly on the negative hand side of the Nyquist plot. Thus the internal feedback loop is not unconditionally stable, although, as one can see in the plots above, there is a good gain margin, which could be even bigger if a phase lag compensator was properly designed for the internal loop under study.

## 4.4 Velocity sensor and piezoelectric patch actuator frequency response function when an accelerometer control sensor with R-C time integrator is considered for the internal feedback control loop.

Following the formulation presented in paragraph 4.2 it is possible to derive the frequency response function between the velocity sensor with embedded a velocity feedback control loop and a closely located piezoelectric patch actuator mounted on a plate. In this case the velocity sensor for the internal feedback loop consists of an inertial accelerometer which is modelled as a spring, $k_s$, damper, $c_s$, and mass, $m_s$, system mounted on the inertial mass, $m_a$, of the principal sensor. Figure 62 below shows a schematic representation of the system where the forces and velocities at the connecting points are defined in details.

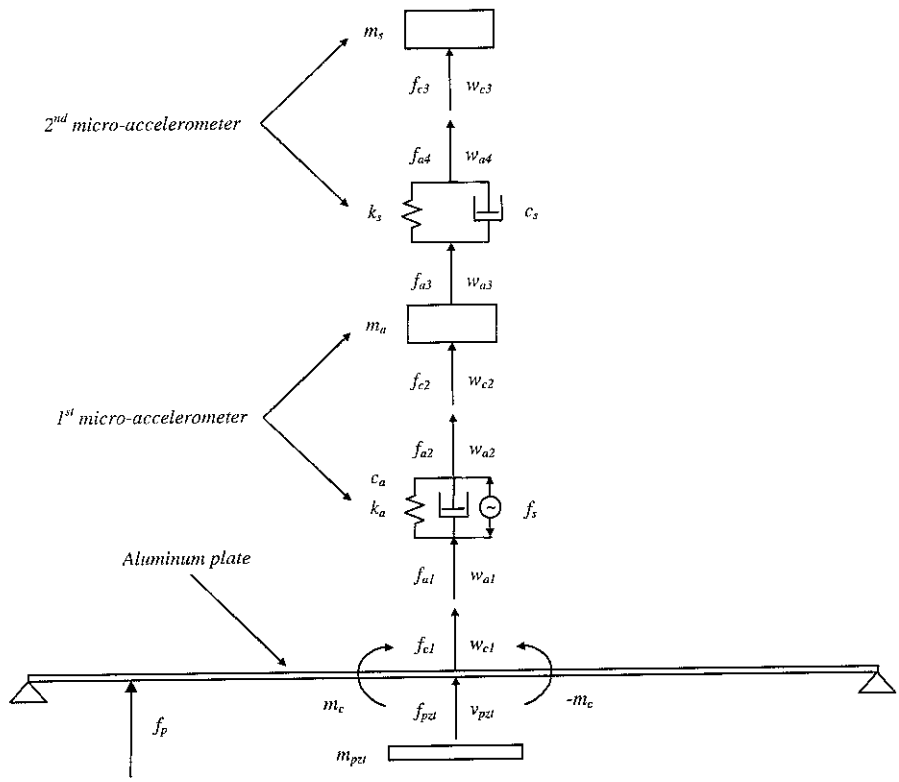


**Figure 62:** *scheme of the velocity sensor with the accelerometer control sensor mounted on the seismic mass $m_a$ of the principal sensor.*

The velocity $\dot{w}_{c1}$ of the plate and the velocities $\dot{w}_{c2}$ and $\dot{w}_{c3}$ of the two seismic masses $m_a$ and $m_s$ can be derived using the mobility approach as seen in section 3.2, so that:

$$\begin{cases} \dot{w}_{c1} = Y_{11} f_{c1} + Y_{cp} f_p + Y_{cc} m_c \\ \dot{w}_{c2} = Y_{22} f_{c2} \\ \dot{w}_{c3} = Y_{33} f_{c3} \end{cases}, \tag{4.59}$$

where $Y_{11}$ is the point-mobility of the plate at the control position $(x_1,y_1)$ as given in equation (3.13), $Y_{22}$ is the mobility of the seismic mass, $m_a$, as given in equation (3.15), and $Y_{33}$ is the mobility of the seismic mass, $m_s$, which, following the formulation in equation (3.14), is found to be

$$Y_{33} = \frac{\dot{w}_{c3}}{f_{c3}} = j\omega m_s . \tag{4.60}$$

Also $Y_{cp}$ and $Y_{cc}$ are the mobility terms giving the velocity at the control position per unit

primary force and unit control strength as given respectively in equations (2.6) and (2.7) and then (2.20) and (2.21). As done in section 3.2, equations (4.59) could be grouped in matrix form as follow:

$$\dot{\mathbf{w}} = \mathbf{Y}\mathbf{f} + \mathbf{Y}_{\mathrm{p}} f_p + \mathbf{Y}_{\mathrm{c}} u_c , \tag{4.61}$$

where in this case:

$$\dot{\mathbf{w}} = \begin{Bmatrix} \dot{w}_{c1} \\ \dot{w}_{c2} \\ \dot{w}_{c3} \end{Bmatrix}, \tag{4.62}$$

$$\mathbf{Y} = \begin{bmatrix} Y_{11} & 0 & 0 \\ 0 & Y_{22} & 0 \\ 0 & 0 & Y_{33} \end{bmatrix}, \tag{4.63}$$

$$\mathbf{f} = \begin{Bmatrix} f_{c1} \\ f_{c2} \\ f_{c3} \end{Bmatrix}, \tag{4.64}$$

$$\mathbf{Y}_{\mathrm{p}} = \begin{bmatrix} Y_{cp} \\ 0 \\ 0 \end{bmatrix}, \qquad \mathbf{Y}_{\mathrm{c}} = \begin{bmatrix} Y_{cc} \\ 0 \\ 0 \end{bmatrix}. \tag{4.65a,b}$$

The responses of the connecting elastic elements of the two spring–mass subsystems are derived in terms of impedances following the formulation presented in section 3.2 with equations (3.22) to (3.28) so that for the bottom elastic connecting element it is found that

$$\begin{Bmatrix} f_{a1} \\ f_{a2} \end{Bmatrix} = \begin{bmatrix} Z_{11}^{a} & Z_{12}^{a} \\ Z_{21}^{a} & Z_{22}^{a} \end{bmatrix} \begin{Bmatrix} \dot{w}_{a1} \\ \dot{w}_{a2} \end{Bmatrix} + \begin{Bmatrix} -f_s \\ +f_s \end{Bmatrix} \tag{4.66}$$

and for the top elastic connecting element

$$\begin{Bmatrix} f_{a2} \\ f_{a3} \end{Bmatrix} = \begin{bmatrix} Z_{11}^{s} & Z_{12}^{s} \\ Z_{21}^{s} & Z_{22}^{s} \end{bmatrix} \begin{Bmatrix} \dot{w}_{a2} \\ \dot{w}_{a3} \end{Bmatrix}. \tag{4.67}$$

where:

$$Z_{11}^{a} = Z_{22}^{a} = \frac{k_a}{j\omega} + c_a \quad \text{and} \quad Z_{11}^{s} = Z_{22}^{s} = \frac{k_s}{j\omega} + c_s, \tag{4.68a,b}$$

$$Z_{12}^{a} = Z_{21}^{a} = -\frac{k_a}{j\omega} - c_a \quad \text{and} \quad Z_{12}^{s} = Z_{21}^{s} = -\frac{k_s}{j\omega} - c_s. \tag{4.69a,b}$$

According to the notation sown in Figure 62, the compatibility and force equilibrium conditions at the connecting points 1, 2 and 3, are given by:

$$\begin{cases} \dot{w}_{a1} = \dot{w}_{c1} \\ \dot{w}_{a2} = \dot{w}_{c2} \\ \dot{w}_{a3} = \dot{w}_{c3} \end{cases} \tag{4.70}$$

and

$$\begin{cases} f_{a1} + f_{c1} + f_{pzt} = 0 \\ f_{a2} + f_{c2} = 0 \\ f_{a3} + f_{c3} = 0 \end{cases} \Rightarrow \begin{cases} f_{c1} = -f_{a1} - f_{pzt} \\ f_{c2} = -f_{a2} \\ f_{c3} = -f_{a3} \end{cases}, \tag{4.71}$$

where $f_{pzt}$ is the force due to the inertial effect of the piezoelectric patch strain actuator. Thus considering the equilibrium and compatibility conditions and using the impedance formulation for the two connecting elements, given in equations (4.66) and (4.67), and for the lumped mass effect of the piezoelectric patch actuator, given in equations (3.41) and (3.42), the following matrix expression can be derived:

$$\begin{Bmatrix} f_{a1} \\ f_{a2} \\ f_{a3} \end{Bmatrix} = \begin{bmatrix} Z_{11}^{a} + Z_{pzt} & Z_{12}^{a} & 0 \\ Z_{21}^{a} & Z_{22}^{a} + Z_{11}^{s} & Z_{12}^{s} \\ 0 & Z_{21}^{s} & Z_{22}^{s} \end{bmatrix} \begin{Bmatrix} \dot{w}_{a1} \\ \dot{w}_{a2} \\ \dot{w}_{a3} \end{Bmatrix} + \begin{Bmatrix} -f_s \\ +f_s \\ 0 \end{Bmatrix}. \tag{4.72}$$

which can be re-written in compact form as follows:

$$\mathbf{f} = -\overline{\mathbf{Z}}\dot{\mathbf{w}} + \mathbf{h}_s f_s, \tag{4.73}$$

where:

$$\overline{\mathbf{Z}} = \begin{bmatrix} Z_{11}^{a} + Z_{pzt} & Z_{12}^{a} & 0 \\ Z_{21}^{a} & Z_{22}^{a} + Z_{11}^{s} & Z_{12}^{s} \\ 0 & Z_{21}^{s} & Z_{22}^{s} \end{bmatrix} \quad \text{and} \quad \mathbf{h}_s = \begin{bmatrix} -1 \\ +1 \\ 0 \end{bmatrix}. \tag{4.74a,b}$$

Substituting equation (4.73) in equation (4.61) and solving with respect to the velocity vector $\dot{\mathbf{w}}$ it is found:

$$\dot{\mathbf{w}} = (\mathbf{I} + \mathbf{Y}\overline{\mathbf{Z}})^{-1}\left\{\mathbf{Y}\mathbf{h}_s f_s + \mathbf{Y}_p f_p + \mathbf{Y}_c u_c\right\}. \tag{4.75}$$

As shown in Figure 63 below, a direct velocity feedback is implemented within the velocity sensor. The output signal from the accelerometer mounted on the seismic mass $m_a$, $v_s = c_\sigma (w_{c3} - w_{c2}) \cong -c_\sigma \dfrac{\ddot{w}_{c2}}{\omega_s^2}$, is first integrated with an R-C analogue circuit with transfer function given by equation (3.4), so that, above the integrator cut off frequency, the signal becomes proportional to velocity , that is $\hat{v}_s = \dfrac{c_\sigma}{1 + j\omega\tau}(w_{c3} - w_{c2}) \cong -c_\sigma \dfrac{\ddot{w}_{c2}}{j\omega\tau\omega_s^2} = -c_\sigma \dfrac{\dot{w}_{c2}}{\tau\omega_s^2}$.

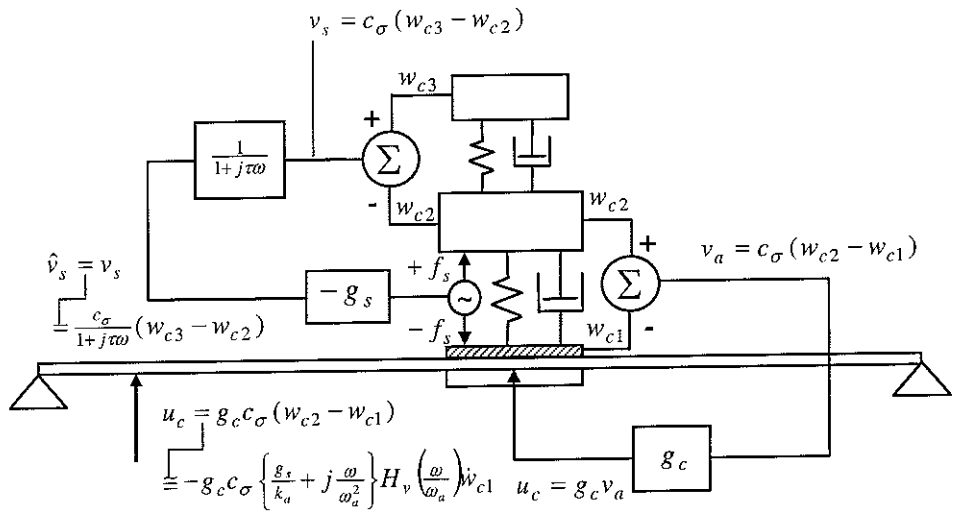


**Figure 63:** *scheme of the accelerometer mounted on an aluminium plate with either a collocated force actuator or closely located moment actuator piezoelectric patch actuator.*

Therefore, the velocity feedback control loop generates two control forces $\pm f_s$ acting between the inertia mass $m_a$ and the vibrating base which are directly proportional to the integrated output signal from the accelerometer via a feedback control gain $g_s$, that is

$$f_s = g_s \hat{v}_s = g_s \frac{c_\sigma}{1+j\omega\tau}(w_{c3} - w_{c2}) = g_s \frac{c_\sigma}{1+j\omega\tau}\mathbf{d}_s \dot{\mathbf{w}}, \tag{4.76}$$

where, in this case

$$\mathbf{d}_s = [0 \quad -1 \quad 1]. \tag{4.78}$$

Thus equation (4.75) becomes

$$\dot{\mathbf{w}} = (\mathbf{I} - g_s \frac{1}{j\omega} \frac{c_\sigma}{1+j\omega\tau}(\mathbf{I} + \mathbf{Y}\bar{\mathbf{Z}})^{-1}\mathbf{Y}\mathbf{h}_s\mathbf{d}_s)^{-1}(\mathbf{I} + \mathbf{Y}\bar{\mathbf{Z}})^{-1}\{\mathbf{Y}_p f_p + \mathbf{Y}_c u_c\}. \tag{4.79}$$

Following the scheme shown in Figure 63, the output signal provided by the elastic piezoelectric element in the principal sensor, which is proportional to the relative displacement between the seismic mass, $m_a$, and the base, that is $v_a = c_\sigma (w_{c2} - w_{c1})$, is first

magnified by a constant positive gain $g_c$ and then feedback to the piezoelectric patch control actuator so that the input control signal to the piezoelectric patch control actuator is $u_c = g_c v_a = g_c c_\sigma (w_{c2} - w_{c1})$. Thus, according to the results discussed in previous section, provided the optimal control gains $\hat{g}_{s1,2}$ that brings to zero the imaginary part in equation (4.55) are implemented, then the sensor output should be directly proportional to the base velocity, $\dot{w}_{c1}$, that is: $v_a = \mathrm{Re}\{H_g(\omega, g_s)\}\dot{w}_{c1}$. Moreover if the positive control gains $\hat{g}_{s1}$, given respectively by the solid line in Figure 55 or Figure 57, are implemented then, as shown by the faint solid lines in Figures 56 and 58, $\mathrm{Re}\{H_g(\omega, g_s)\} < 0$ and thus the output signal $v_a$ is directly proportional to the opposite of the base velocity, $\dot{w}_{c1}$. As a result, the control excitation generated by the piezoelectric patch actuator is directly proportional to the velocity measured at the base of the error sensor so that a dissipative control excitation, i.e. active damping, is generated. Alternatively if a fixed control gain is implemented in the feedback loop embedded in the velocity sensor, then $u_c = g_c c_\sigma H_g(\omega, \breve{g}_s)\dot{w}_{c1}$ where, in this case, the function $H_g(\omega, \breve{g}_s)$ is real negative only for a limited range of frequencies as shown with the fain line in figure 59. Therefore the piezoelectric patch control actuator produces a damping excitation only in a limited range of frequencies.

As seen in section 3.2 the signal output from the velocity sensor with embedded the velocity feedback control system could expressed in terms of the displacement vector $\mathbf{w} = \{w_{c1} \quad w_{c2} \quad w_{c3}\}^T$ with the following matrix relation

$$v_a = c_\sigma \mathbf{d}_c \mathbf{w}, \tag{4.80}$$

where in this case

$$\mathbf{d}_c = [-1 \quad 1 \quad 0] \tag{4.81}$$

and the displacement vector $\mathbf{w}$ can be derived by pre-multiplying equation (4.79) by $\frac{1}{j\omega}$ so that, assuming $f_p = 0$, the output signal from the sensor is given by

$$v_a = \frac{c_\sigma}{j\omega}\mathbf{d}_c\left\{(\mathbf{I} - g_s\frac{1}{j\omega}\frac{c_\sigma}{1+j\omega\tau}(\mathbf{I}+\mathbf{Y}\bar{\mathbf{Z}})^{-1}\mathbf{Y}\mathbf{h}_s\mathbf{d}_s)^{-1}(\mathbf{I}+\mathbf{Y}\bar{\mathbf{Z}})^{-1}\mathbf{Y}_c u_c\right\}. \quad (4.82)$$

Therefore, the open loop frequency response function of the piezoelectric patch actuator and the velocity sensor with embedded a velocity feedback loop using an accelerometer sensor with an R-C analogue integrator is given by

$$G(\omega) = \frac{v_a}{u_c} = \frac{c_\sigma}{j\omega}\mathbf{d}_c(\mathbf{I} - g_s\frac{1}{j\omega}\frac{c_\sigma}{1+j\omega\tau}(\mathbf{I}+\mathbf{Y}\bar{\mathbf{Z}})^{-1}\mathbf{Y}\mathbf{h}_s\mathbf{d}_s)^{-1}(\mathbf{I}+\mathbf{Y}\bar{\mathbf{Z}})^{-1}\mathbf{Y}_c, \quad (4.83)$$

where the mobility term $Y_{cc}$ in the vector $\mathbf{Y}_c$ is given by equation (2.7) with the modal excitation terms in equations (2.13) or (2.14) depending whether the control actuator is the point force or piezoelectric patch that generates lines of moments along the four edges.

Figure 64 shows the amplitude and phase of the frequency response function between the piezoelectric patch actuator and the velocity sensor with the fixed control gain $\breve{g}_s = \hat{g}_{s1}(\omega = 6000\,\text{Hz})$ given by the positive bullet point in Figure 57. The active damping generated by the velocity feedback loop embedded in the velocity sensor cuts down the resonance peak found with the accelerometer sensor as shown in Figure 62. Also, as discussed in section 2.1, the higher frequencies roll off effect is not affected by the large amount of damping introduced by the velocity feedback loop. Finally the phase plot indicates that, up to about 10 kHz, the phase of the signal output from this sensor is similar to that obtained with the accelerometer sensor and an ideal time integrator which is shown in Figure 52. Therefore the phase is confined between $\pm 90^o$ up to about 4 kHz while at higher frequencies there is a constant phase lag which however is not characterised by the brusque $-180^o$ drop at the resonance frequency so that the phase falls down less rapidly and thus at 50 kHz there is a phase lag of $-450^o$.

Figure 65 shows the Nyquist plots of the frequency response functions between the piezoelectric patch actuator and the velocity sensor with the fixed control gain $\breve{g}_s = \hat{g}_{s1}(\omega = 6000\,\text{Hz})$. This plot show the benefit of the active damping generated by the feedback control loop in the velocity sensor which cuts the higher frequency resonance peak in such a way as the frequency response function gently rolls off above about 4 kHz and thus

the loops in the left hand side of the two Nyquist plots are much smaller than those on the co respective right hand sides.

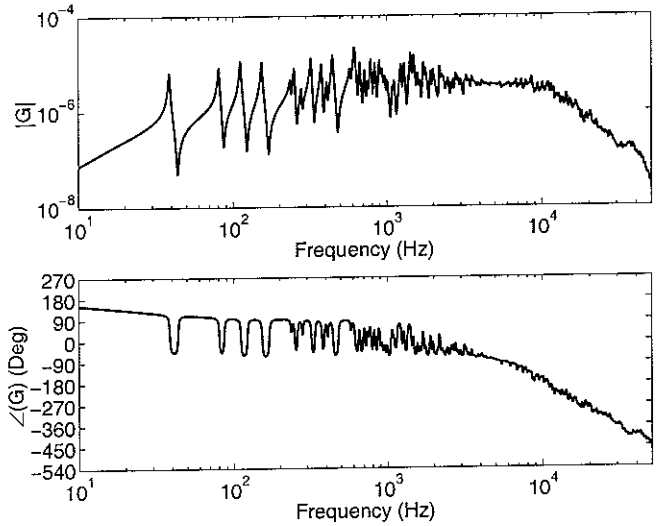


**Figure 64:** *amplitude (top plot) and phase (bottom plot) of the frequency response functions between the piezoelectric patch actuator and the velocity sensor with the fixed control gain indicated by the bullet point in figure 57.*

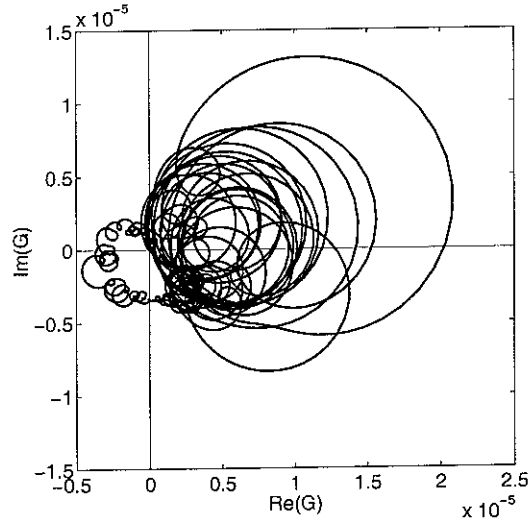


**Figure 65:** *Nyquist of the frequency response functions between the piezoelectric patch actuator and the sensor with the feedback gain indicated by the bullet point in figure 57.*

Therefore, although the control system with the piezoelectric patch actuator and velocity sensor with internal feedback control loop using an accelerometer sensor with an R-C time integrator is still conditionally stable, provided the internal control gain $g_s$ is properly tuned, it is possible to implement realistic control gains that would produce enough active damping without compromising the stability of the system.

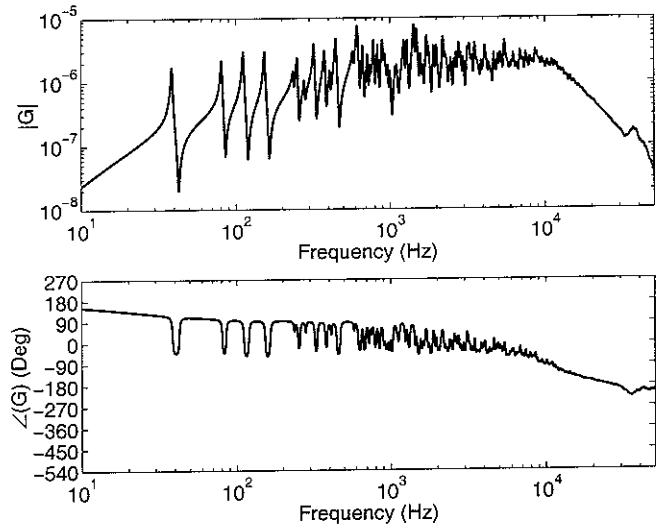


**Figure 66:** *amplitude (top plot) and phase (bottom plot) of the frequency response functions between the half size and 4.1 g mass piezoelectric patch actuator and the velocity sensor with either the feedback gain indicated by the bullet point in figure 57.*

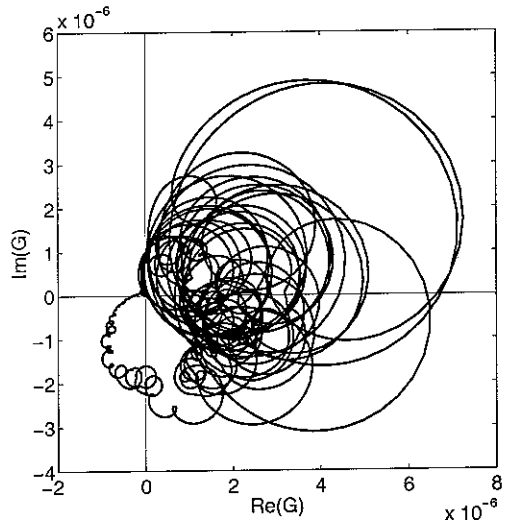


**Figure 67:** *Nyquist of the frequency response functions between the half size and 4.1 g mass piezoelectric patch actuator and the sensor with the feedback gain indicated by the bullet point in figure 57.*

As done in section 4.2 the case where the actuator size is reduced to half but the total weight is kept the same as in the previous study is considered. Figures 66 and 67 show the amplitude–phase and Nyquist plots for a sensor–actuator pair where the piezoelectric patch actuator dimensions are reduced to half, that is $a_x \times a_y = 15 \times 15$ mm, but the total weight is left unaltered to 4.1 g by increasing the thickness of the patch by a factor of 4, that is $h_{pe} = 2$ mm. Both figures highlight that having reduced the size of the patch but kept its total mass to be the same gives a sensor–actuator pair with a larger gain margin since the relative

size between the loop on the left hand side and those on the right hand side of Nyquist plot is much smaller that that found in the previous case as shown in the plots of Figure 65.

The stability of the internal feedback loop embedded in the sensor can be assessed by considering equation (4.75) when the primary force is set to zero so that:

$$\dot{\mathbf{w}} = (\mathbf{I} + \mathbf{Y}\overline{\mathbf{Z}})^{-1}\{\mathbf{Y}\mathbf{h}_s f_s + \mathbf{Y}_c u_c\}. \tag{4.84}$$

According to the formulation presented in section 4.3 the output signal from the sensor is proportional to the opposite of the base velocity, thus in order to implement velocity feedback, the control signal input to the piezoelectric patch actuator is set to be

$$u_c = g_c v_a = g_c c_\sigma (w_{c2} - w_{c1}). \tag{4.85}$$

Therefore equation (4.84) becomes

$$\dot{\mathbf{w}} = \left(\mathbf{I} - (\mathbf{I} + \mathbf{Y}\overline{\mathbf{Z}})^{-1}\mathbf{Y}_c g_c \frac{c_\sigma}{j\omega}\mathbf{d}_c\right)(\mathbf{I} + \mathbf{Y}\overline{\mathbf{Z}})^{-1}\mathbf{Y}\mathbf{h}_s f_s, \tag{4.86}$$

so that, the ratio between the integrated output signal from the accelerometer control sensor, $\hat{v}_s = \frac{c_\sigma}{1 + j\omega\tau}(w_{c3} - w_{c2})$ and the control force generated by the feedback control loop embedded in the sensor, $f_s$, is given by

$$\frac{\hat{v}_s}{f_s} = G_s = \frac{c_\sigma}{1 + j\omega\tau}\frac{1}{j\omega}\mathbf{d}_s\left(\mathbf{I} - (\mathbf{I} + \mathbf{Y}\overline{\mathbf{Z}})^{-1}\mathbf{Y}_c g_c \frac{c_\sigma}{j\omega}\mathbf{d}_c\right)(\mathbf{I} + \mathbf{Y}\overline{\mathbf{Z}})^{-1}\mathbf{Y}\mathbf{h}_s. \tag{4.38}$$

Figure 68 shows the modulus and phase and the Nyquist plot of the open loop frequency response function between the integrated output signal from the accelerometer control sensor and the control force $f_s$ of the actuator embedded in the velocity sensor when the fixed control gain gain $\breve{g}_s = \hat{g}_{s1}(\omega = 6000\,\text{Hz})$ is used in the internal feedback loop.

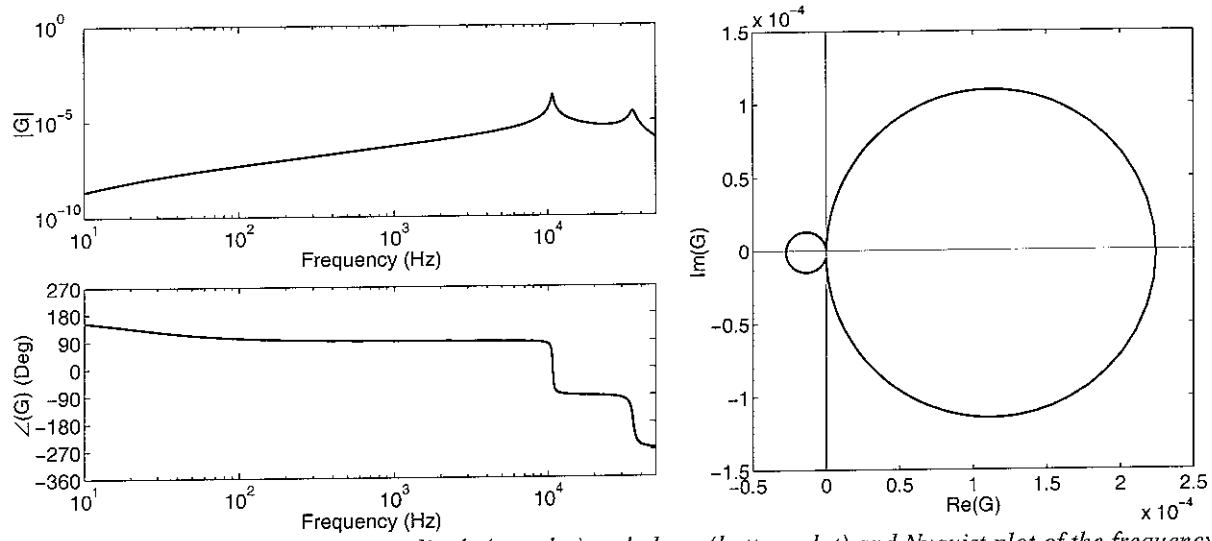


**Figure 68:** *frequency response amplitude (top plot) and phase (bottom plot) and Nyquist plot of the frequency response function between the integrated output signal from the accelerometer control sensor and the control force $f_s$ of the actuator embedded in the velocity sensor when the fixed control gain $\breve{g}_s = \hat{g}_{s1}(\omega = 6000\,\text{Hz})$ is used in the internal feedback loop.*

This figure indicates that the internal control loop in the sensor is not affected by the dynamics effects of the plate structure and piezoelectric patch actuator. As a result the response is characterised by the fundamental resonance which is controlled by the spring–mass principal sensor system and by a second resonance which is controlled by the spring–mass accelerometer sensor system. Both resonances generates a phase lag of 180°. The first resonance produces the large loop on the right hand side of the Nyquist plot while the second resonance produces the relatively smaller loop on the left hand side of the Nyquist plot. Thus the control loop embedded in the velocity sensor is only conditionally stable although the result presented in Figure 68 indicates that there is a good gain margin that could be improved by designing a proper compensator for the internal feedback loop.

# 5. CONCLUSIONS

This report has presented the design study of a new velocity sensor to be used in combination with a piezoelectric patch actuator which forms a closely located sensor–actuator pair for the implementation of a direct velocity feedback control loop in thin structures such as plates or shells. The velocity sensor consists of a principal spring–mass seismic sensor with embedded a direct velocity feedback control loop acting on the lumped mass itself. This simple control system could be bonded onto a panel or shell in order to generate active damping, which would reduce the vibration of the structure dominated by well separated low frequency resonances.

The response of the velocity sensor with the internal feedback control loop has been studied theoretically with a lumped parameter model which takes into account both the dynamics effect of the principal spring–mass sensor as well as the dynamics effects of the accelerometer control sensor used for the internal velocity feedback control loop. The study has shown that provided a proper frequency dependent control gain is implemented in the internal feedback loop, the velocity sensor output is proportional to the opposite of the velocity at the base of the sensor itself. Also, the internal feedback loop produces an active damping effect in such a way as the resonance of the spring–mass principal sensor is damped down and thus the response of the sensor is not characterised by the classic higher frequency resonance peak of accelerometers. Quite importantly, this active damping effect does not degrade the characteristic higher frequency roll off of the response of the spring–mass principal sensors. In this way the unwanted higher frequencies actuation and dynamics effects of the piezoelectric patch actuator that makes the sensor–actuator pair to be non-collocated and dual are filtered out. As a result relatively higher control gains could be implemented in the feedback loop to drive the piezoelectric patch actuator without the danger of instabilities. The study has also shown that if the frequency dependant control gain in the internal feedback control loop is replaced with its mean value than the output from the principal seismic sensor is still proportional to the opposite of the velocity at the base of the velocity sensor over a relatively wide frequency band. Also, the higher frequency active damping effect is still generated so that the resonance frequency of the principal spring–mass sensor is flattened down and the higher frequencies response roll off is preserved.

The study presented in the report has also considered the role of the piezoelectric patch actuator in the stability of the velocity feedback control loop. In particular, a parametric study has been carried out which has shown that the sensor–actuator control unit could be made more stable by using a relatively heavy and small piezoelectric patch actuator so that the efficient higher frequency excitation of the panel by the piezoelectric patch is brought down by the inertial effect of the piezoelectric patch and because of the reduced actuation strength at higher frequencies for relatively small patches.

For completeness a parametric study has also been carried out to assess the stability of a control loop with a standard spring–mass accelerometer sensor and a piezoelectric patch actuator. The fundamental resonance of an accelerometer sensor is an important cause of instability in such a velocity feedback since it introduces an $180^{o}$ extra phase shift and a significant increase of the amplitude in the sensor–actuator frequency response function which makes the system to be unstable even for relatively small control gains. This parametric study has shown that as the natural frequency of the accelerometer is reduce as the intrinsic rising effect of the amplitude with frequency due to the moment excitation generated by the piezoelectric patch actuator is cut down at lower frequency. This is because beyond the resonance frequency the accelerometer output naturally rolls off. Also, as one would expect, the phase shift of $180^{o}$ is moved down in frequency. However, the combined inertial effect of the piezoelectric patch, which tends to pull down the sensor output signal and also generates a constant phase lag with frequency becomes relevant at relatively higher frequencies. As a result it has been found that is better to use an accelerometer with relatively high natural frequency so that the $180^{o}$ phase shift due to the accelerometer resonance is combined with a $90^{o}$ or even $180^{o}$ phase lag introduce by the inertial mass of the actuator and thus the large output response generated by the resonance tends to assume real positive values so that the feedback loop is stabilised.

## ACKNOWLEDGEMENTS

Part of the work presented in this report has been carried out by Mr. Gavagni within the "European Doctorate in Sound and Vibration Studies" (EDSVS) which is supported by the European Commission through the 'Marie Curie Training Site' programme. This project has been supported by the Dipartimento di Ingegneria at the Università di Ferrara in Italy with a grant funded by the "Ministero dell'Istruzione dell'Università e Ricerca".

## REFERENCES


[1] S.J. Elliott, P. Gardonio, T.C. Sors and M.J. Brennan, 2001 *Active vibro-acoustic control with multiple feedback loops*, Journal of the Acoustical Society of America, Vol. 111, No. 2, pp. 908-915.

[2] P. Gardonio, E. Bianchi and S.J. Elliott. *Smart panel with multiple decentralized units for the control of sound transmission. Part I: theoretical predictions. Part II: design of the decentralised control units. Part III: control system implementation.* Journal of Sound and Vibration, **274**, 163-192, 193-213, 215-232.

[3] A. Preumont, 2002 *Vibration control of active structures.* (London: Kluwer Academic Publihers, 2nd Edition).

[4] J.Q. Sun, 1996 *Some observations on physical duality and collocation of structural control sensors and actuators*, Journal of Sound and Vibration, Vol. 194, pp. 765-770.

[5] M.J. Balas, 1979 *Direct velocity control of large space structures*, Journal of Guidance and Control, Vol. 2, pp. 252-253.

[6] S.S. Rao 1995 *Mechanical Vibration.* (New York: Addison-Wesley Publishing Company, 3rd Edition).

[7] S.J. Elliott, M. Serrand and P. Gardonio 2001 *Feedback stability limits for active isolation systems with reactive and inertial actuators.* Transactions of the ASME, Journal of Vibration and Acoustics **123**, 250 -261.

[8] P. Gardonio and S.J. Elliott. *Modal response of a beam with a sensor–actuator pair for the implementation of velocity feedback control.* Accepted for publication in the Journal of Sound and Vibration.

[9] P. Gardonio and S.J. Elliott 1999 *ISVR Technical Report No 277* Driving point and transfer mobility matrices for thin plates excited in flexure.

[10] C.R. Fuller, S.J. Elliott and P.A. Nelson, 1996 *Active Control of Vibration.* (London: Academic Press).

[11] G.F. Franklin, J.D. Powell and A. Emami-Naeini, 2002 *Feedback control of dynamic systems.* (Prentice Hall, 4th Edition).

[12] G. Marro, 1987 *Controlli Automatici* (Bologna, Zanichelli, 3rd Edition)

[13] L. Meirovitch, 1990 *Dynamics ad Control of Structures* (New York, John Wiley & Sons)